Chapter 1

Introduction and literature review

This chapter introduces the potentiality of biomimetic materials, particularly HA nanocrystals, as an alternative to traditional implant biomaterials, due to their strong resemblance to the mineral phase of living bone in composition and morphology. This chapter also provides a critical and comprehensive review of the various synthesis routes for the development of different morphologies of HA nanocrystals, such as nanorods, nanoplates, nanowires, nanofibers, nanotubes, nanoneedles, nanowishkers, nanobelts, nanoribbons and nanosheets, with a focus to understand the process science. Moreover, the role of various experimental parameters, such as hydrothermal (HT) temperature and time, nature and concentration of organic additives, pH of precursor solution, and elemental doping on size, morphology, aspect ratio, crystallinity and state of agglomeration of HA nanocrystals is thoroughly explained. Further, systematic discussion has also been made on bone tissue engineering and drug delivery applications of HA nanocrystals, with special emphasis on several essential physical and experimental parameters to achieve the desired performance of HA nanocrystals. Finally, the motivation behind selecting the 2-D HA nanoplates as the primary research focus, compared to other HA nanocrystal morphologies, is also provided.

1.1. Biomaterials

Over the past few years, with the advancements in materials and biological sciences as well as nanotechnology, biomaterials have become the exciting field of research for medical applications. Titanium alloys are the most widely used biomaterials for bone and dental implants, owing to their good strength and efficient biocompatibility. However, they still face various challenges, such as bioactivity, non-biodegradability, and relatively low resistance to corrosion. These challenges hinder their ability to integrate with surrounding bone tissue, leading to complications that require the removal of implants. Recently, the demand for

biomimetic materials like HA has been continuously increasing. It has the capability to integrate with surrounding bone tissue, facilitate cell growth and the formation of new bone, which reduces the necessity for implant removal. Advancements in nanotechnology have also made it possible to create biomaterials at the nanoscale level. High surface area and small particle size allow it to improve interactions with cells and enter them to deliver drugs inside the cells while targeting cells or tissues, creating opportunities for personalised medicine and precise treatments.

1.2. Hydroxyapatite (HA)

HA, a prominent member of the calcium phosphate family with a chemical formula of $Ca_{10}(PO_4)_6(OH)_2$ (Ca/P: 1.67), is the prime mineral constituent of natural bone tissue, constituting approximately 65 % by weight of the total composition in human bone. It crystallizes in a hexagonal crystal structure (Fig. 1.1) with lattice parameters of a = 9.4000 Å, b = 9.4000 Å, c = 6.9300 Å and a space group of *P63/m*, and plays a crucial role in maintaining the structural strength, resilience, physiological activity, and bio-functionality of bones [1].

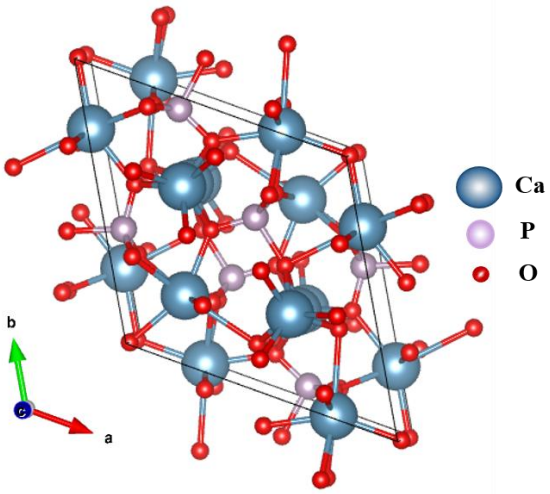

Fig. 1.1. *Hexagonal crystal structure of HA.*

Due to resemblance (phase and composition) with the mineral phase of living bone, artificial HA has long been considered as one of the most preferred biomaterials in bone tissue

engineering, dental implants, and biocoatings. HA renders remarkable biological features, such as bioactivity, osteoconductivity, osteoinductivity, and nonimmunogenic response etc. [2-4]. Its ability to integrate with surrounding tissues, promote cellular adhesion, and facilitate osseointegration made it an ideal candidate for various biomedical implants. Their bioactivity and osteoconductivity facilitate the direct bonding with surrounding bone tissue, which promotes the osseointegration, osteogenesis, and reduces the rejection risks in biomedical implants. HA also possesses a range of other valuable properties, such as adsorption capacity, selectivity, environmental friendliness, and non-toxic nature, that make it highly suitable for drug delivery applications. At the microscale, the properties of HA are solely composition-dependent, i.e., remain unaffected by changes in size and morphology. To address the limitations of bulk HA, reducing its dimension to the nanoscale is essential to control the mechanical, biological (bioactivity, cell adhesion, and proliferation, and differentiation), antibacterial, and drug release response.

1.3. HA nanocrystals

HA nanocrystals possess a higher specific surface area that allows many receptor proteins to interact with HA, ultimately leading to a significant enhancement in cellular functionality. Unlike bulk HA, nanosized HA can be engulfed easily by cells via membrane penetration, stimulating cell growth and facilitating intracellular drug delivery [5-10]. Moreover, the high specific surface area of nano-sized HA (nHA) facilitates a greater number of adsorption sites as compared to bulk HA, which can be potentially utilized for drug loading and sustained release behavior. In addition, the issue of brittleness of bulk HA can be addressed via the formation of ultra-long HA nanowires [11]. Shi et al.[6] reported that the degree of MG-63 cell growth and proliferation has abruptly increased on reducing the size of HA from micro to nanoscale with a diameter of 20 nm. Lyu et al.[12] reported that flexural yield and compressive yield strengths, and compressive modulus of HA rods (~ 41 wt %) reinforced poly(amino acids)

composites significantly increase from 78.1 – 105.7 MPa, 73.8 – 85.8 MPa and 3 – 3.5 GPa, respectively, on reducing the size of HA rods from micro, i.e. (1000 × 100) nm to nano level, i.e. (200 × 40) nm. It has been suggested that the higher specific surface area of HA nanorods than microrods allows better stress transfer within poly(amino acids) matrix. It is well known that living bone consists of ~ 65 wt.% 2 D-plate-like HA nanocrystals with 4 –10 nm in thickness, 30 – 200 nm in length and width, which are well dispersed within the collagen nanofibers matrix towards their longitudinal axes in the form of complex hierarchical structure, that provide such an exceptional strength and fracture toughness to the bone [13-15].

The properties of nanocrystals are highly sensitive to their size, and morphology along with composition, i.e., at nanoscale, only a small change in their physical dimension can make a major impact on their properties [16]. For instance, Ma et al.[17] reported that 5 μm sized HA nanowires strongly stimulate the differentiation of osteogenic stem cells. However, the unfavorable differentiation of stem cells has been observed in case of HA nanorods. Li et al.[18] revealed that smaller HA nanorods (aspect ratio: 2.9) provide better support to stem cell proliferation than larger HA nanorods of aspect ratio of about 4.4. Nathanael et al.[19] observed better osteoblastic attachment, differentiation and proliferation on HA nanowires than HA nanorods.

In view of the above, the development of different morphologies of HA nanocrystals becomes an area of interest. These morphologies can be categorized as: (1) 1-D and (2) 2-D nanocrystals. 1-D nanocrystals possess nanoscale dimensions (≤ 100 nm) in two directions, and their shape is characterized by the aspect ratio, which is defined as the ratio of length to diameter or width. In contrast, 2-D nanocrystals have a single nanoscale dimension, and their aspect ratio is defined as the ratio of length to thickness. Nanorods (Aspect ratio: ≤ 15), nanowires (Aspect ratio: ≥ 1000), nanofibers (Aspect ratio: ≥ 30), nanotubes (Aspect ratio: ≥ 5), and nanoribbons (Aspect ratio: ≥ 50) are evolved in the first category. However, HA nanoplates (Aspect ratio:

≤ 50) and nanosheets (Aspect ratio: ≥ 50) are associated with the second category. A number of fabrication techniques have been used to develop HA nanocrystals, such as HT/solvothermal (ST) method, microwave (MW)-assisted technique, microemulsion approach, template method, biomimetic route, co-precipitation, sol-gel method, solid-state method, electrospinning technique, and sonochemical method, etc. These morphologies of HA nanocrystals can be controlled during the fabrication stage by controlling the experimental variables, such as HT temperature and time, concentration of organic additives, pH of solution and elemental doping [20-27]. Further, the aforementioned morphologies of HA nanocrystals have been effectively used in multidimensional applications— development of scaffold for bone defect repair, anticancer drug carrier for osteosarcoma treatment, making of filter paper for water purification, development of fireproof cloths, making of invisible ink for security printing, electrochemical sensor and catalysis etc. [10, 28-35].

1.4. Synthesis methods

Generally, there are two basic approaches to synthesize the nanocrystals - (1) Top-down approach, which refers to the etching of bulk material to nano dimension systematically, leading to the formation of nano-sized crystals, where arc discharge technique, laser ablation, mechanical milling, anodization, electrospinning, and ultra-sonication are some of the well-known dimension reducing techniques, and (2) bottom-up approach involves the production of fine nanocrystals directly from the molecular precursors via the number of routes including HT, ST, MW, micro-emulsion, co-precipitation, sol-gel, chemical vapor deposition (CVD), template mediated route, sonochemical and biomolecule assisted synthesis [16, 36].

Number of properties of HA nanocrystals, such as biological, mechanical, dielectric response, AC conductivity, solubility, and stability are strongly dependent on it’s composition, size, dimension, morphology and type of doping [37-39]. Therefore, significant efforts have been made to produce various morphologies of HA nanocrystals viz., nanorods, nanoneedles,

nanowires, nanofibers, nanobelts, nanowishkers, nanotubes, nanoplates and nanosheets using both, top-down and bottom-up synthesis approaches. However, the later approach is suggested to be more reliable owing to better controllability in composition, size, shape and morphology [40]. Fig. 1.2 summarizes the fraction of published research articles with a particular morphology against the total available articles on HA nanocrystals. The synthesis procedures of the above-mentioned HA nanocrystals (1-D and 2-D) are critically reviewed in the subsequent sections.

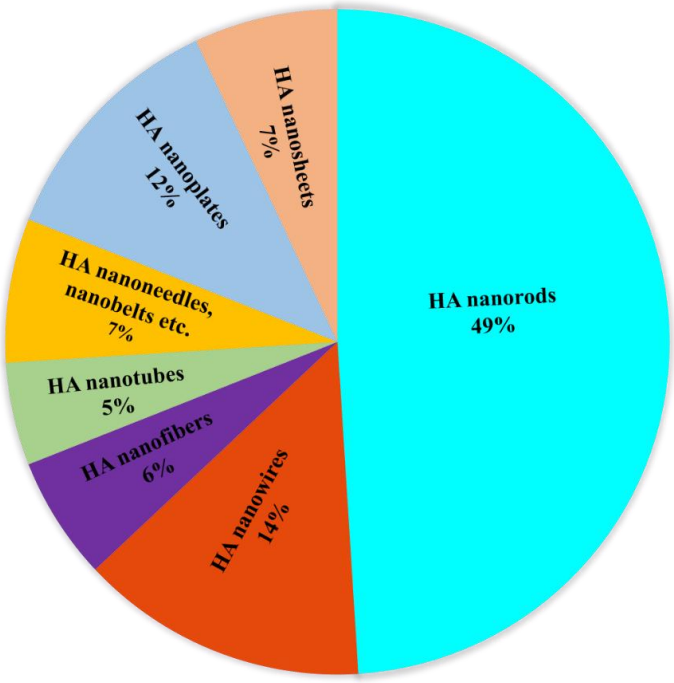

Figure 1.2. *The fraction of total number of research articles of a particular morphology of HA nanocrystals. The foremost number of research articles are based on the HA nanorods.*

1.4.1. Synthesis of 1-D HA nanocrystals

1.4.1.1. HA nanorods

In the past few years, number of synthetic strategies has been evolved to develop HA nanocrystals with controllable morphology. The wet chemical synthesis approaches, including chemical precipitation technique, sol-gel method, HT method, MW method, emulsion, and sonochemical synthesis, have been extensively used to design the HA nanorods [41]. Among

these techniques, HT method is the most popular technique to develop HA nanorods, that offers better morphological control, fine grained single crystal, high purity, good homogeneity, narrow size distribution due to the chemical reaction taking place at higher temperature (up to 200ºC) and pressure (3 – 25) MPa [20, 23, 24, 26, 29, 34, 37, 39, 42-53][54-82]. It has also been observed in number of studies that crystallinity, size, aspect ratio, morphology, and colloidal stability of HA nanorods are very sensitive to both, HT temperature and time. There are three types of variations in the aspect ratio of HA nanorods with increasing the HT temperature and time; (1) The aspect ratio of HA nanorods is proportional to both, HT temperature and time. For example, Wang et al.[20] demonstrated that on increasing the HT temperature from 120°C to 150°C, aspect ratio of HA nanorods increases from 3 to 10 with the increment in the size (especially along it's length) from (60 × 20) nm to (150 × 15) nm in presence of CTAB at pH of 12 and HT time of 20 h. In addition, as the HT time varies from 20 h to 24 h, aspect ratios of HA nanorods have also been found to increase from 3 to 5 with the transformation of size from (60 × 20) nm to (75 × 15). In another study, Wang et al.[49] synthesized HA nanorods under the condition of three different organic additives, such as Trisodium citrate, PEG 600, and tween 20 at pH 10 and HT time of up to 8 h. For three of them, similar effect of HT temperature on aspect ratio of HA nanorods has been reported. It means that higher HT temperature and longer HT time favors the growth of HA nanorods along their c-axis direction (responsible for increment in length) rather than a-axis direction. (2) Aspect ratio of HA nanorods is inversely proportional to both, HT temperature and time. Zhu et al.[38] and Jin et al.[67] demonstrated that aspect ratio of HA nanorods decreases from 7.5 – 4 and 7.6 – 5 with increasing the HT temperature from 90°C – 150°C and 90°C – 180°C, respectively (Fig. 1.3A and B). Neto et al.[72] also found similar variation in aspect ratio of HA nanorods with HT time (0 – 5) h without using any additive. Such reduction in aspect ratio of HA nanorods with increasing the HT temperature and time is attributed to significant enhancement in rate of

crystal growth along their a-axis (responsible for increment in diameter) with slower crystal growth along their c-axis. (3) Aspect ratio of HA nanorods is almost constant with both, HT temperature and time. For instance, Zhao et al.[26] and Jin et al.[67] observed no significant change in aspect ratio of HA nanorods with varying HT temperature and time (Fig. 1.3 C), respectively, because the ratio of crystal growth rate along a- and c-axes of HA nanorods is almost constant with increasing the HT temperature and time. Hoai et al.[75] supported this variation of aspect ratio (2.26 – 3.34) of HA nanorods with HT time (6 – 18) h (Fig. 1.3 D). it can be affirmed that on the increasing the both HT temperature and time, the size of HA nanorods increases. However, the type of variation in ratio of crystal growth rate along c- to a-axis with HT temperature and time depends upon the type of organic additive and pH condition used, for the synthesis of HA nanorods.

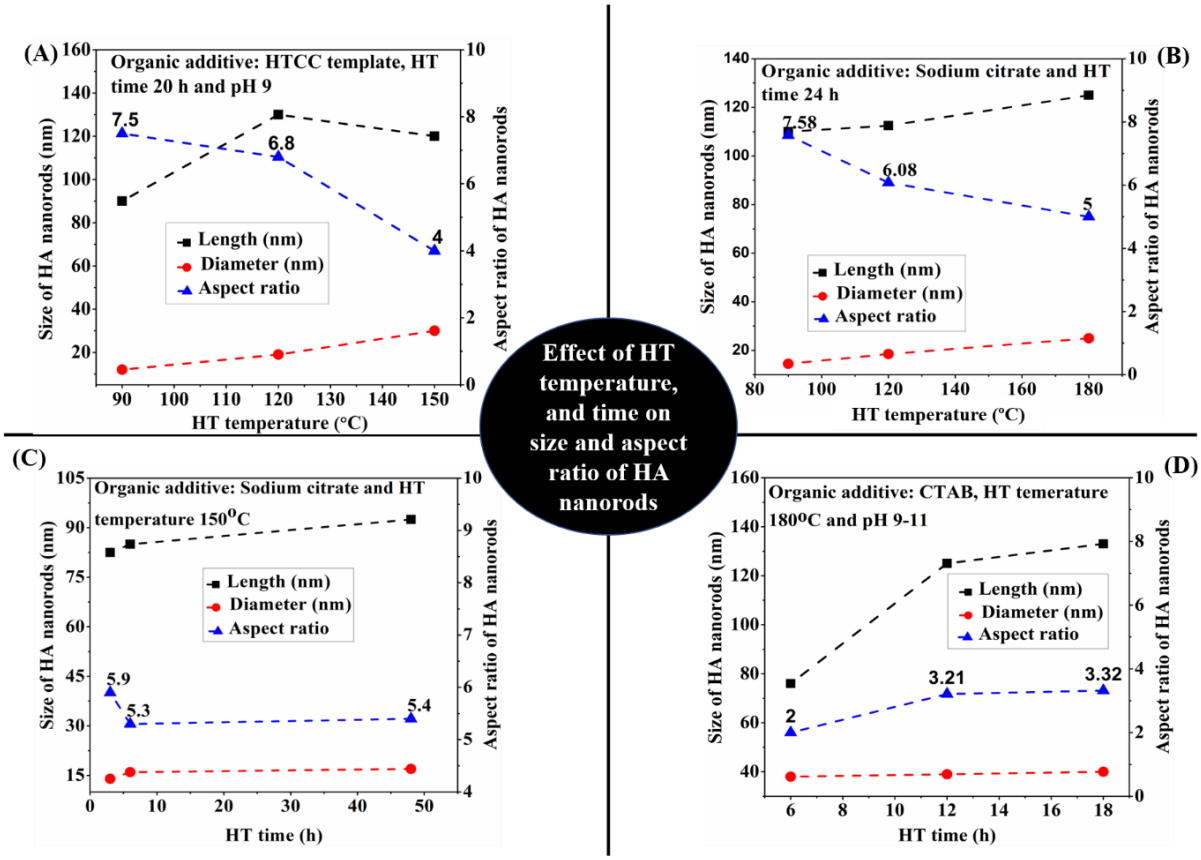

Figure 1.3. Role of HT temperature and time on the size and aspect ratio of HA nanorods. *Variation in length, diameter, and aspect ratio of HA nanorods against the HT temperature (A, B) and time (C, D). Data are taken from the Refs. [38, 67, 75]*

Few results also reveal that crystallinity of HA nanorods is proportional to HT temperature, and time [26, 49, 66, 67, 72]. On the contrary, colloidal stability of HA nanorods is observed to decrease with increasing HT temperature and time, owing to increase in size of HA nanorods [67].

Therefore, the HT temperature and time can be suggested as key parameters to control the crystallinity, morphology, aspect ratio and colloidal stability of HA nanorods.

Despite of remarkable advantageous effects, there are few shortcomings of HT method, such as high energy loss, slower reaction rate and longer processing time. Therefore, in order to reduce the energy and time consumption, Liu et al.[83] adopted, for the first time, the clean and eco-friendly technique i.e., "microwave (MW) irradiation" to synthesize the HA nanorods. This method has the ability to heat the solution homogenously with high reaction rate due to its direct coupling with reacting molecules by dipolar polarization and conduction mechanisms [84]. Also, the developed HA nanorods exhibit high purity, narrow size distribution and smaller particle sizes [83, 85]. This method has been widely explored by number of studies for the production of HA nanorods [83, 85-97].

The wet chemical precipitation, which is one of the oldest method, has also been utilized to fabricate the HA nanorods [18, 22, 98-105]. Other synthesis approaches for the development of HA nanorods, include sonochemical homogeneous precipitation [106], sol-gel [107-109], ST methods [17, 110-112], and electrophoretic deposition [113]. Some of the studies combined two synthesis approaches to achieve the integrated advantageous effect from both the techniques, which include chemical precipitation-HT [49, 50, 114, 115], MW-HT [21, 116-118], ultrasonication- precipitation [119], HT solid-state conversion [120]. Recently, gas-

injection strategy has been applied in HT and ST methods to increase the pressure within autoclave, since high pressure plays a critical role in achieving the nanomaterial with good crystallinity, which, in turn, improves the mechanical properties. Nosrati et al [121, 122]. injected the argon gas and mixture of argon and hydrogen gases in autoclave, and reported the increase in crystallinity, crystallite size, particle size, elastic modulus and hardness of HA nanorods. Fig. 1.4 summarizes the year-wise evolution in the aspect ratio of HA nanorods, developed from HT, MW, MW-HT, and sol-gel techniques with and without the use of organic additives. The following points can be noted from Fig. 1.4: (1) the HT method became the first choice for large number of researchers to develop the HA nanorods; (2) most of the hydrothermally synthesized HA nanorods have aspect ratio in the range of 2 – 15 in comparison to MW, MW-HT and sol-gel synthesized nanorods having aspect ratio less than 10 (except single report); and (3) CTAB is the most commonly used organic additive.

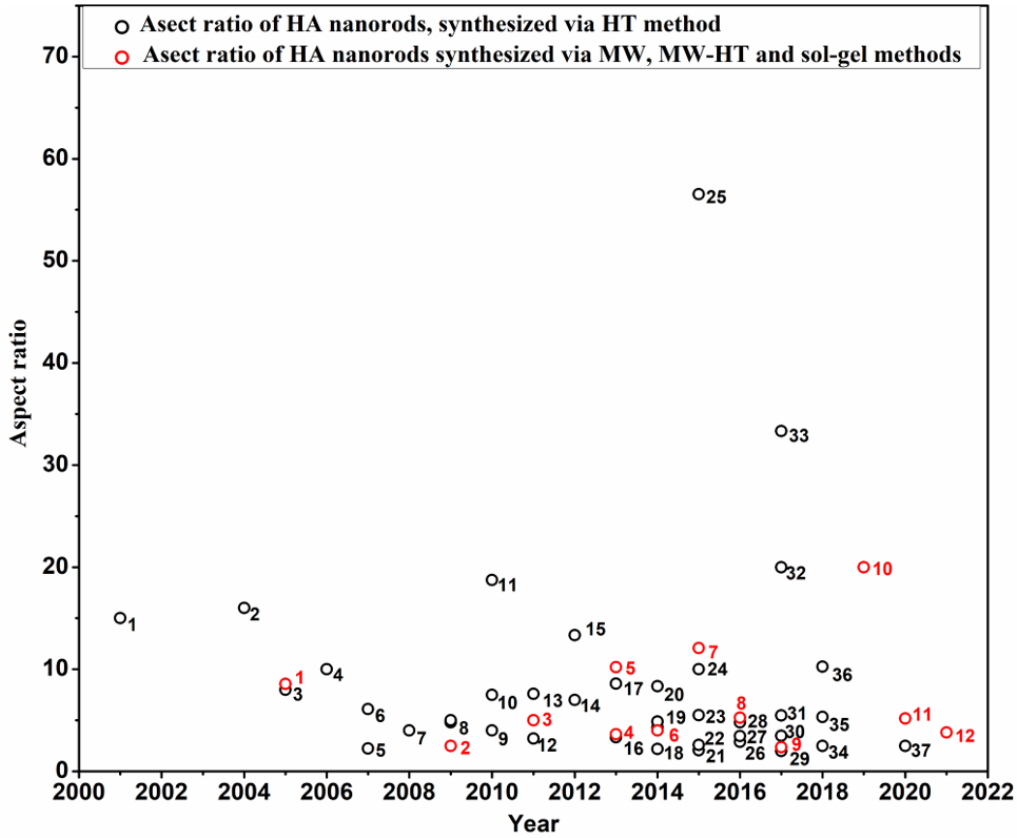

1, 4, 7, 12, 14, 20, 28, 30, 34: CTAB surfactant as a template.	**1:** No organic additive (MW)
10, 13, 15, 21, 27, 35, 37: No organic additives	**2:** No additive (Sol-gel)
2: Amino acids	**3:** No additive (Sol-gel)
3: Poly(amidoamine) dendrimer	**4:** Zwitter ions (MW)
5: PEG 600.	**5:** CTAB (MW-HT)
6: CTAB/n-Pentanol	**6:** CTAB (Sol-gel)
8: CTAB, and Pluronics	**7:** EDTA (MW-HT)
9: PiGA-mPEG Block co-polymer biomolecule	**8:** No additive (MW)
11: HTTC template	**9:** CTAB (MW)
16: RP biomolecule	**10:** Ascorbic acid (MW)
17: Tamarind extract as natural template	**11:** Amino acid (MW-HT)
18: Glutamic acid + Urea	**12:** Licorice root extract
19: PEO20-PPO70-PEO20 (P123) block co-polymer	
22: Alginate	
23: Sodium citrate	
24: no additive, oleic acid + ethanol, and Apicot tree gum	
25 : Polyvinyl pyrrolidone (PVP)	
26: Sodium citrate	
29: Urea	
31: Mango extract template	
32: PEG 20000	
33: Sodium lignin sulfonate	
36: Brij-93 surfactant	

HTTC: N-[(2-hydroxy-3-trimethylammonium)propyl]chitosan chloride
RP: Riboflavin-59-phosphate monosodium salt

Figure 1.4. *The Year-wise (since last 21 years) evolution in the aspect ratio of HA nanorods, synthesized from HT, MW-HT and sol-gel techniques with and without the use of organic additives.*

1.4.1.1.1. Role of experimental parameters on size, morphology, aspect ratio, and state of agglomeration of HA nanorods

Organic additives, pH of the solution, calcination temperature and elemental doping play a critical role during the synthesis of HA nanorods, which are elaborately discussed in the subsequent sections.

(i) Role of organic additives

Since, control over the morphology and size of HA nanorods appears to be a major challenge with conventional methods [21]. Therefore, template mediated synthesis method, a type of highly tuneable route, has been attracted considerable attention for the synthesis of HA nanorods using organic additives as a template. Variety of organic additives have been used for the preparation of HA nanorods of different aspect ratios, which can be divided into following categories: surfactant [29, 64, 70, 80, 99, 116], organic molecules [34, 56, 67, 94, 117], polymers [39, 48, 49, 51, 57, 123] biomolecules [26, 38, 66], and other natural sources [63, 92, 112].

Surfactant is one of the most promising templating agents, owning to its high efficiency in controlling the morphology of HA nanocrystals with minimum agglomeration. Few of the most well-known ionic and nonionic surfactants include CTAB [20, 21, 29, 45, 55, 75, 80, 90, 91, 97, 101, 109], ethylenediamine tetra acetic acid (EDTA) [58, 70, 86] sodium dodecyl sulfate (SDS) [45, 70], Titron X-100 [124], tween 80 [49], zwitterions [85], Pluronics (P123) [54, 64] and Brij-93 [81]. The mechanism behind the formation of different morphological HA nanocrystals is best described by surfactant based microemulsion system. Emulsion, a type of thermodynamically stable transparent suspension, contain two immiscible liquids “water and oil”, in which surface-active agents are used to stabilize the suspension. Since the water phase is dispersed in oil phase under agitation. Therefore, the incorporation of surfactant is necessary to control the interfacial tension of immiscible phases [125, 126]. Above a critical

concentration of surfactant, the water is dispersed as micro- droplets, surrounded by single layer of surfactant molecules, leading to the formation of reverse micelles. These micro-droplets of aqueous phase, stabilized in nanosized droplets by surfactant, act as an independent micro or nanoreactor, in which synthesis of nanocrystals takes place [126]. The micelles provide heterogeneous nucleating sites for $(PO_4)^{3-}$ and Ca^{2+} ions on their surfaces for the growth of HA nanocrystals. After the specified growth, surfactant can be easily removed through solvent extraction or calcination process, which results in the formation of porous HA nanocrystals [64, 80]. Fig. 1.5A illustrates the templating mechanism for the formation of HA nanorods in presence of CTAB surfactant as a template. Above critical micelle concentration (CMC), which is 1 mM for CTAB, it initially self-assembled into spherical like micelles which then converted to rod shaped micelles. Meanwhile, CTAB ionizes into cetyltrimethylammonium cation (CTA^+), where ammonium group can act a nucleation site for HA formation. On the addition of PO_4^{3-} ions, it effectively interacts with CTA^+ through strong electrostatic attraction to form CTA^+–PO_4^{3-} complex. Such strong interaction might also be due to stereochemical compatibility in chemical structure (Tetrahedral) of both CTA^+ and PO_4^{3-} ions. Further, CTA^+–PO_4^{3-}complex electrostatically interacts with Ca^{2+} to form $Ca_9(PO_4)_6$ clusters, which then ultimately crystalizes to HA nanorods within micelles with continuous heat treatment [20, 45, 75, 101, 127].

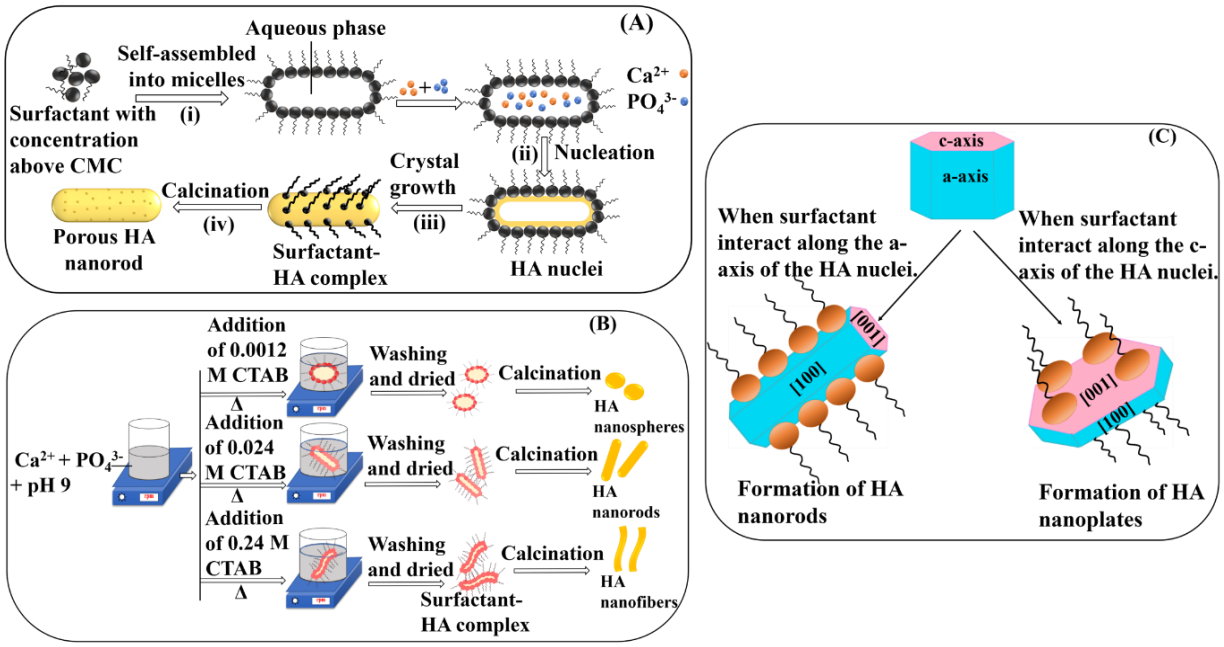

Figure 1.5. Role of organic additives (Surfactants, organic molecules, and polymers) in controlling the morphology of HA nanorods. *(A) CTAB surfactant-based template mechanism for the formation of HA nanorods: (i) above the critical micellar concentration (CMC), self-assembly of CTAB molecules into rod shaped micelles; (ii) nucleation of HA on the surface of micelles; (iii) growth of HA nuclei under heat treatment to form the CTAB-HA complex; and (iv) removal of CTAB through calcination, leading to the formation of porous HA nanorods [20, 45, 75, 101, 125, 127]. (B) Effect of surfactant concentration on the morphology of HA nanocrystals [21]. (C) Role of organic additives into crystallographic growth of HA nanorods and nanoplates. In case of HA nanorods, organic additives molecules restrict the crystal growth along a-axis (side faces) of HA nuclei by capping them and activate the growth along c-axis (end faces), and inverse is also true for the formation of HA nanoplates [22, 39, 68].*

Micelles exhibit varieties of shapes, including spherical, rod and lamellar, which is sensitive to surfactant concentration, i.e., surfactant concentration determines the morphology of HA nanocrystals. For example, Gopi et al [21]. synthesized various morphologies of HA nanocrystals such as HA nanospheres, nanorods and nanofibers at CTAB concentrations of 0.0012 M, 0.024 M, and 0.24 M, respectively (Fig. 1.5 B).

Similar micelle-based mechanism has also been proposed for other surfactants such as SDS, P123, and zwitterions to synthesize the HA nanorods.

The morphology of HA nanorods can be controlled using organic molecules such as sodium citrate [68, 100] and oleic acid [128] as well as polymers such as polyvinylpyrrolidone (PVP) [39], and polyethylene glycol (PEG) [22]. The organic additive prevents the HA crystal growth in [1 0 0] crystallographic direction of hexagonal HA crystallite by strongly interacting with (100) facet and makes the growth feasible along the c-axis i.e., [0 0 1] crystallographic direction, which leads to the formation of HA nanorods [68]. However, in case of nanoplates, the additive restrict the growth along c-axis and allow the crystal growth along a-axis, i.e., [1 0 0] crystallographic direction [39]. Fig. 1.5 C schematically represents the growth mechanism of nanorods and nanoplates in the presence of organic additive.

Despite of multiple advantages associated with the use of these additives, there are number of critical concerns, i.e., difficulty in removal due to their hydrophobicity, potential toxicity and high cost. Therefore, the biomolecules, which is biocompatible and nontoxic in nature, have been utilized as template to synthesize the HA nanorods. Moreover, another problem during HA synthesis has also been addressed using the biomolecules, which is rapid nucleation as well as uncontrolled crystal growth of HA due to use of separate phosphorus precursor in solution for the synthesis of HA nanorods. This leads to higher availability of PO_4^{3-} ions in solution at a time. Therefore, the phosphorus enriched biomolecules such as Riboflavin-59-phosphate monosodium salt (RP), pyridoxal-50-phosphate (PLP) and creatine phosphate have been used as both, organic template as well as phosphorus source [26, 66, 111]. it exhibits several advantages: (i) The PO_4^{3-} ions is not free in the precursor solution which is preventing the fast nucleation; (ii) The hydrolysis of biomolecules to release the PO_4^{3-} ions requires certain heat condition. Therefore, by controlling the reaction condition, the release rate of PO_4^{3-} ions can be controlled to obtain the desire size of HA nanorods; (iii) it provides the controlled crystal

growth due to progressive release of PO_4^{3-} ions as hydrolysis proceeds; and (iv) biomolecules also play a role of organic template to control the shape of HA nanorods. For RP, the controlled mechanism for the formation of HA nanorods is as follows: As the HT reaction proceeds at temperature of 120ºC, the RP molecules begin to hydrolyze and releases number of PO_4^{3-} ions. Now, the hydrolysed R – OH biomolecules react with Ca^{2+} ions to form R– Ca^{2+} complex, which then further reacts with free PO_4^{3-} ions to form HA nuclei. Such nuclei grow to HA nanorods on prolong HT treatment for 24 h. The similar mechanism is explained for PLP and creatine phosphate biomolecules.

However, the higher cost of biomolecules is still a main problem. Therefore, eco-friendly and low-cost natural templates have been adopted to control the morphology of HA nanorods. These include Banana [63], Grape [63, 76], Tamarind [63, 76], Mango [76], *Moringa oleifera flower* [92], Apricot tree gum (ATG) [70], Green polymer sodium lignin sulfonate (SS) [112], Licorice root extract [118], and Caffeine [129]. Recently, Alorku et al.[130] summarized various synthesis routes for HA nanostructures using plant derived bio chemicals such as surfactant, biomolecules, chelating agent or structure directing agents.

Effect of concentration and nature of organic additives on size, morphology and colloidal stability of HA nanorods

Few research groups also observed that size, aspect ratio, morphology, and colloidal stability of nanorods are strongly dependent on the concentration and nature of organic additives, used into the reaction medium. Gopi et al.[21] demonstrated that MW assisted hydrothermally prepared HA nanorods become longer and much thinner with mean aspect ratio, typically ranging from 6.7 – 10.2 on increasing the concentration of CTAB surfactant from 0.012 M to 0.024 M. In another report, Nathanael et al.[19] also observed that aspect ratio of HA nanorods is proportional to CTAB concentration (0 to 1 mmol). Similarly, Hoai et al.[75] reported the identical effect of CTAB concentration on aspect ratio [Fig. 1.6 A (a)], because the size of HA

nanorods follow the upward trend from (133 × 40) nm to (158 × 45) nm on varying the CTAB concentration of about 0.64 g to 4 g. Such variation in the size of HA nanorods might be due to increase in size of CTAB micelles. It can be affirmed that CTAB is suitable organic additive to obtain HA nanorods with desired aspect ratio. PVP is another organic additive, used as aspect ratio booster. For instance, Nathanael et al.[39] suggested that aspect ratio of HA nanorods increases from 22 – 56 with increasing the PVP in the range of (0 – 4) g/L due to increment in their length. Fig. 1.6 A (b) shows such variation for PVP surfactant, which strongly interact with side faces (a-axis) of HA nucleus than end faces (c-axis). Therefore, with increasing the PVP concentration, restriction in growth of HA nucleus along a-axis (side faces) increases, which consequently, increases the growth along c-axis. As a result, aspect ratio of HA nanorods increases. In contrast, Nga et al.[64] and Chen et al.[117] reported the inverse relationship between concentration of organic additives, such as P123 and amino acid, and aspect ratio of HA nanorods, respectively [Fig. 1.6 A (c and d)]. On increasing the concentration of P123 from (0 – 2) g, shape of rod-like micelles became wider instead of longer [Fig. 1.6 A (c)]. Therefore, HA nanorods of lower aspect ratio produces due to increase in diameter and negligible change in length. In case of Fig. 1.6 A (d), increase in the concentration of amino acids from (0 – 1.2) M leads to drastic reduction in length of HA nanorods with negligible change in diameter of HA nanorods. The amino acids adsorbed on the HA crystal surface, especially along the c-axis direction, through the coordination of COO^- with Ca^{2+} ions, reduces the amount of Ca^{2+} and PO_4^{3-} ions in crystal growth process, which subsequently, reduce the length. Higher the concentration of amino acids means more COO^- ions are coordinated with Ca^{2+} ions, which hinder the crystal growth along c-axis, i.e., length of HA nanorods decreases [117]. Jin et al.[68] demonstrated that aspect ratio of HA nanorods gradually increases from 3.7 to 4.8 with increasing the concentration of sodium citrate from 0 – 0.0133 M, which was attributed to significant reduction in mean diameter from (24 – 9) with almost similar length of HA

nanorods, because the tendency of citrate ions to inhibit the growth of HA along a-axis is much higher than c-axis and such tendency increases with increase in sodium citrate concentration. However, more efforts are still required to develop a clear understanding about the effect of sodium citrate concentration on aspect ratio of HA nanorods. Moreover, size and morphology of HA nanocrystals also differ from one organic additive to other, which can be clearly seen in Fig. 1.6 B [29, 49, 70, 116].

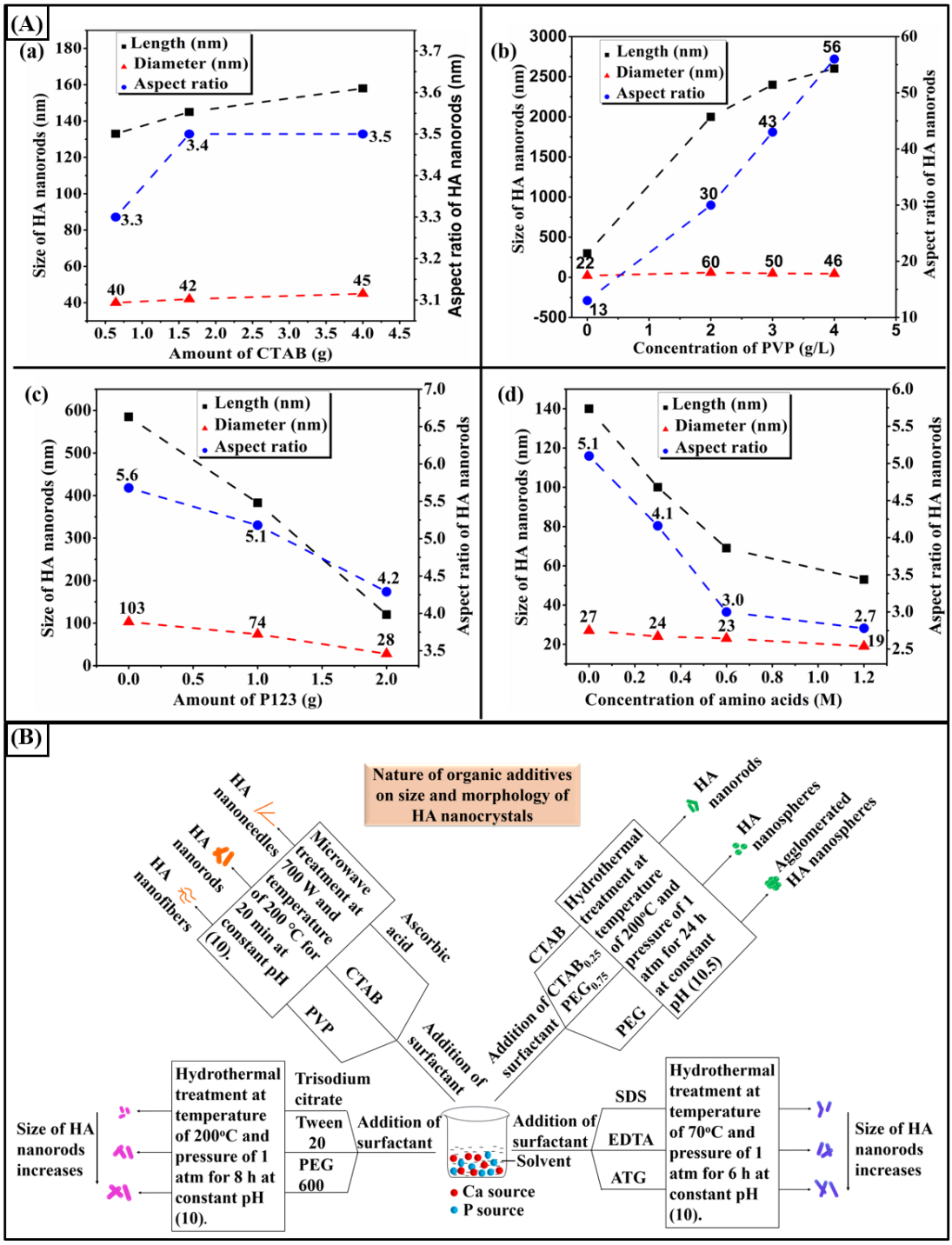

Figure 1.6. Effect of concentration and nature of organic additives on size, morphology and aspect ratio of HA nanocrystals. *(A) Variation in length, diameter, and aspect ratio of HA nanorods againstvarious concentrations of organic additives, and (B) Influence of nature of organic additive on size and morphology of HA nanorods [29, 49, 70, 116].*

Organic additives are also beneficial to inhibit the nano aggregation by the adsorption of their molecules on the surface of nanorods that causes electrostatic repulsion among the micelles [39, 57, 67, 76]. Nathanael et al.[39] and Jin et al.[67] demonstrated that there is a linear correlation between concentration of organic additives i.e., PVP and sodium citrate, respectively, and colloidal stability.

(ii) Role of pH

The second most important influential parameter i.e., pH of the solutions also controls the morphology, size and colloidal stability of HA nanocrystals. There are number of reports suggesting different mechanisms, by which the morphology of HA nanocrystals can be customized with the variation of pH [22, 55, 70, 83, 99]. Liu et al.[83] synthesized HA nanocrystals with different morphologies by changing the pH of the solution from 9 to 13 (Fig. 1.7 A). At lower pH value of about 9, Ca-EDTA complex releases Ca^{2+} ions due to their poor stability. Such free Ca^{2+} ions move into the atomic lattice of the HA crystallites. HA nanorods are formed as a consequence of the anisotropic growth of HA crystallites. While, on increasing the pH (~13), concentration of OH^- ions increases. Therefore, each facet of HA crystallite has almost equal probability to generate the active sites due to strong adsorption of OH^- ions on it's surface. Also, the stability of Ca-EDTA complexes increases. Therefore, instead of Ca^{2+} ions, entire Ca-EDTA complexes bind with active sites of the crystallites. In this case, neighbouring distance between these complexes does not permit Ca^{2+} ions to organize in actual crystal lattice of HA, which results in the formation of new nucleus at limited active sites. Under the microwave treatment, each HA crystallite transformed into nanoflower morphology owing to anisotropic growth of newly formed nucleus at limited active sites. Similarly, Chen et al.[99] suggested that the morphology of fluorapatite (FHA) nanocrystals depends upon the stability of Ca^{2+}-EDTA complex. At low pH, complex is not stable and Ca^{2+} releases, which, in turn, produces large number of nucleates of bigger size. These nucleates self-assembled into

spherical form to minimize their energy. Since, such spherical form contains many active sites. Therefore, it grows to flower like FHA nanocrystals on further release of Ca^{2+} ions. On increasing the pH from 4 to 6, limited amount of Ca^{2+} releases, resulting in the formation of a smaller number of nuclei of smaller size. Each nucleate forms only a single FHA nanorod/nanowire attributing to their smaller size. In another study, Zhang et al.[55] synthesized nanoparticles (NPs)/very short nanorods at pH 7 or 9 (neutral or alkaline condition) and micro sheets, micro flowers and bur-like microspheres in acidic environment (4, 4.5 and 5). It has been suggested that under alkaline conditions, the crystal growth is isotropic or weak anisotropic due to high adsorption probability of OH^- ions on the surface of HA nuclei, which results in NPs or nanorods. On the other hand, at acidic condition, the adsorption probability of OH^- ions on the surface of HA nuclei is limited, which promote the formation of micro sheets, micro flowers-like morphology due to anisotropic crystal growth.

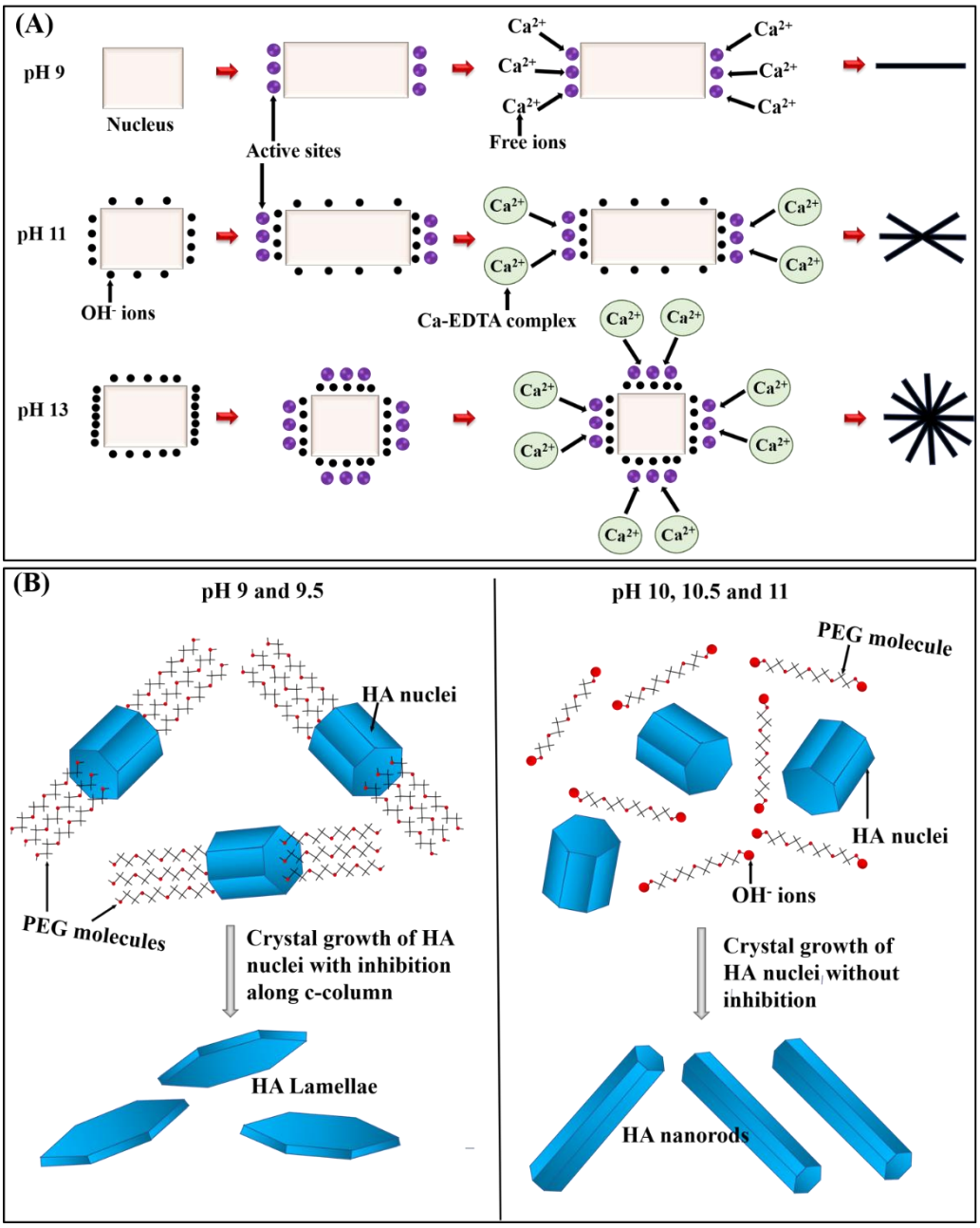

Figure 1.7. *Role of pH of precursor solution on the morphology of HA nanocrystals. Reproduced with the permission from publisher, Refs. [22, 83].*

In addition, Taheri et al.[70] prepared FHA NPs, nanoflowers, and nanorods at pH of 6, 8 and 10, respectively, using ATG surfactant. It has been suggested that this may be due to change in bonding ability of surfactant to Ca^{2+} ions and number of FHA seeds during the growth process of FHA. Furthermore, Zuo et al.[22] obtained laminated HA nanocrystals at pH of 9 – 9.5 and rod-shaped nano HA at pH of 10 – 11. Fig. 1.7 B schematically represents the formation of

these nanocrystals. In case of HA lamellae, the PEG molecules restrict the crystal growth along the c-axis of HA nuclei after their adsorption on the end face through the hydroxyl groups. Thereby, crystal growth proceeds along a- and b-axes of HA. Whereas, on increasing the pH up to 10, concentration of OH^- ions increase in the solution, which interact with more and more PEG molecules. As a result, smaller number of PEG molecules adsorbed on the end face of HA, which gradually weaken the inhibition force towards the crystal growth of HA along the c-axis, leading to the formation HA nanorods or needles.

From all these mechanisms, it can be clearly affirmed that the number of adsorbed OH^- ions and stability of Ca^{2+}-surfactant complex play a critical role during HA crystal growth while varying the pH.

In addition to morphology, pH also affects the size of HA nanorods and colloidal stability. Zhu et al.[38] demonstrated that the size of HA nanorods decreases from (120 × 30) nm to (40 × 20) nm on varying the pH value in the range of 9 – 13. Since at higher pH of about 13, the concentration of OH^- ions are much higher than that of PO_4^{3-} ions. Therefore, the repulsion between OH^- and PO_4^{3-} ions reduces the probability of collision between two tetrahedral structures, PO_4^{3-} and HTTC, which resist these tetrahedral structures to interact with each other. Consequently, it disturbs the HA to crystallize as HA nanorods. However, at lower pH of about 9, resistance of interaction between PO_4^{3-} and HTTC tetrahedral decreases due to lower concentration of OH^- ions, which favours HA to crystallize as rod-like morphology. Jin et al.[68] reported the similar effect of pH (7 – 10) on the size of HA nanorods. Moreover, colloidal stability of nanorods is also observed to enhance with increase in the pH value from 7.5 – 10, because at lower pH (~7), hydrogen citrate ($HC_6H_5O_7^{2-}$) and dihydrogen citrate ($H_2C_6H_5O_7^-$) types of ions are adsorbed on the HA surface due to the partial dissociation of citrate ions, which lowers the charge density on the surface. Therefore, the electrostatic repulsion is not enough to overcome the aggregation of nanorods. While, at pH 8, no

dissociation of citrate ions occurs. Consequently, the electrostatic repulsion among the HA nanorods becomes strong enough to provide the colloidal dispersion due to adsorption of Cit^{3-} ions on the surface of HA nanorods. Chen et al.[34] also observed the similar effect. It can be clearly suggested that the pH value of 9 – 10 provides the most favourable condition towards the development of HA nanorods with controlled size.

(iii) Role of calcination temperature

Most of the studies involved the calcination step to remove the organic template. However, few reports also investigated that the calcination temperature also plays a major role in controlling the size, aspect ratio, morphology and crystallinity of HA nanocrystals [51, 61, 82, 87, 125]. Saha et al.[125] calcined HA NPs at 450°C and 650°C and observed that the size of HA NPs increases with increase in the calcination temperature. Nguyen et al.[61] reported that the aspect ratio of nanorods increases from 5.84 – 7.00 due to increase in their length after calcination at 500°C. However, with increase in calcination temperature up to 700°C, the aspect ratio decreases to 4.2 with considerable increase in diameter. Mishra et al.[87] reported that HA nanorods can only be formed above the calcination temperature of about 700°C. Also, the degree of crystallinity increases with heat treatment temperature [82].

(iv) Role of doping

The development of new techniques/approaches to modify the key properties, such as mechanical, biological, chemical, electric, dielectric and optical etc. of HA nanocrystals for various applications, are in continuous thrust. Among these, doping of nHA with various types of elemental ions appears to be an effective way to control the size, morphology, crystallinity, lattice parameter, bioactivity, cell proliferation, antibacterial activity, mechanical properties, dielectric, and electrical conductivity [24, 89, 90, 94, 131]. This method has been adopted as biomimicking strategy. The natural bone consists of variety of metal ions, e.g., Na^{+}, K^{+}, Sr^{2+}, Mg^{2+}, Zn^{2+}, $Fe^{3+/2+}$, Mn^{2+}, Cu^{2+} etc. in trace amount, which play an important role in regulating

it's metabolic activity. In this perspective, Ca^{2+} ions in HA are being substituted by metal ions such as K^{+}, Mg^{2+}, Sr^{2+}, Ce^{3+}, Al^{3+}, Fe^{3+} W^{6+}, Mo^{2+}, Te^{4+}, Eu^{3+}, Zn^{2+}, Ag^{+}, La^{3+}, Bi^{3+}, Co^{2+}, Cd^{2+} and OH^{-} ions in HA are being replaced by CO_3^{2-}, F^{-}, Cl, Br^{-} and SeO_3^{2-} ions [132]. There are several reports on the synthesis of doped HA nanorods with various ions, such as Sr^{2+} [24, 56, 71, 88, 133], Zn^{2+} [23], Mn^{2+} [96], Fe^{3+} [132], Co^{2+}[134], V [135], Cs^{3+} [93], W^{6+} [89], Mo^{2+} [91]**,** Te^{4+} [90], Eu^{3+} [34, 69], Ag^{+} [94], Al^{3+} [136], Gd^{3+} [74], Tb^{3+} [69], Y^{3+} [60], Si^{4+} [137], Er^{3+} [105], CO_3^{2-} [138], and F^{-} [62, 70, 139]**.** According to few reports, the successful elemental doping on HA nanorods was validated by observing changes in its lattice parameters (Table 1.1).

Table 1.1 Variation in lattice parameter and crystallinity of HA nanocrystals with elemental doping

S. No.	**Doping elements**	**Lattice parameters** (Å)		**Degree of crystallinity (X_c %)**		**Ref.**
		Pure HA	**Doped HA**	**Pure HA**	**Doped HA**	
1.	Zn (5 mol %)	a= 9.432 c= 6.880	a = 9.426 c = 6.866	94	92	[23]
2.	Sr (20 %)	a= 9.432 c= 6.880	a = 9.469 c = 6.922	94	90.4	[24]
3.	Y (5 %)	a= 9.417 c= 6.885	a = 9.390 c = 6.870	-	-	[60]
4.	W (40 wt %)	a= 9.520 c= 6.960	a = 9.410 c = 6.880	58	67	[89]
5.	Te (0.08 wt %)	a = 9.422 c = 6.887	a = 9.406 c = 6.885	49	12	[90]
6.	Mo (0.5 %)	a= 9.450 c = 6.910	a= 9.440 c= 6.900	60	66	[91]
7.	Cs (32 %)	a = 9.391 c = 6.864	a= 9.446 c= 6.904	63	51	[93]
8.	Ag (0.1 M)	a = 9.433 c = 6.880	a = 9.405 c = 6.863	-	-	[94]
8.	Co (0.1 M)	a= 9.368 c= 6.870	a= 9.371 c= 6.828	-	-	[134]
10.	V (30 %)	a= 9.426 c = 6.889	a = 9.438 c = 6.885	74	69	[135]

Nathanael et al.[60, 62] reported that the aspect ratio of HA nanorods increases from 4.30 to 7.61 due to reduction in their diameter on 5 wt % of yttrium doping, and from 1.2 – 4.5 due to increment in their length on F^- substitution from (0 – 15.7) mol %. In the case of yttrium doping, the replacement of Ca^{2+} ions with smaller Y^{3+} ions shrink the HA nanorods along diameter. Therefore, the aspect ratio increases [60]. On the other hand, Nathanael et al.[62] proposed that crystallinity and aspect ratio of HA nanorods are interrelated to each other with fluorine substitution. The incorporation of F^- ions increases the crystallinity, which, in turn, promote the crystal growth along c-axis of HA. As a result, aspect ratio of HA nanorods increases because, crystalline HA possesses high surface energy and low planar Ca^{2+} ions density on (001) plane. In HA (without F^- substitution), surface energy and planar density of Ca^{2+} ions are less sensitive to crystallographic orientation due to lower crystallinity. Accordingly, equi-axed or slightly rod-like HA NPs results. In another report, Chen et al.[34] also found that aspect ratio of HA nanorods increases on Eu (1 – 8) % doping, because both, length and width of HA nanorods followed the downward trend from (74 × 22) to (50 × 12) nm. Such evolution in aspect ratio of HA nanorods may be attributed to charge imbalance within the region of local crystal lattice due to substitution of some of Ca^{2+} ions with Eu^{3+} ions. In contrast, Xu et al.[23], Xu et al.[24], Shkir et al.[89] and Karunakaran et al.[94] reported the inverse relationship between aspect ratio and concentration of dopants such as Zn (~1 – 5) mol %, Sr (~1 – 20) mol %, W (~1 – 40) wt % and Ag (~ 0.01 – 0.1) M, respectively and demonstrated that the rate of crystal growth decreases along the c-axis of HA nanorods. In addition, Xu et al.[23, 24] reported the morphology of un-doped HA as nanobelts while, Zn- and Sr-doped HA exhibited uniform rod-like nanocrystals. Zheng et al.[69] also observed the gradual shift in the morphology of HA nanocrystals from nanorods of length 150 nm to nanowires of length 2 μm on successive doping with 0, 5, 10 and 15 % of Eu^{3+} or Tb^{3+} ions. It clearly indicates that the

aspect ratio can be easily tuned with the amount of doping. The effect of doping on aspect ratio of HA nanorods is schematically illustrated in Fig. 1.8.

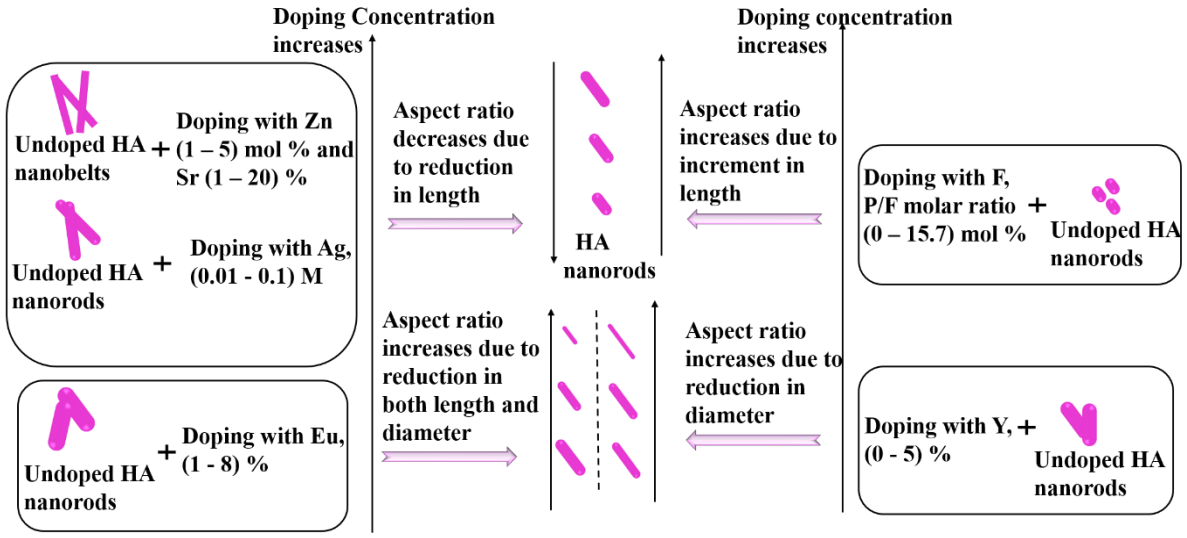

Figure 1.8. *The effect of elemental doping on the aspect ratio of HA nanorods [23, 24, 34, 64, 60, 94].*

The degree of crystallinity also affected with increasing the concentration of elemental doping, such as Mo [91], Te [90], W [89], Cs [93], V [135], Eu [34] and F [62] type of ions (Table 1.1). For doping with Mo^{2+} (0 – 5) % and F^- ions (0 –3) %, the degree of crystallinity of HA nanorods systematically increases from (59.7 – 71.1) % and (13 – 88) %, respectively [62, 91]. Nathanael et al.[62] explained the mechanism for the enhancement in degree of crystallinity with F^- substitution in the terms of replacement of OH^- ions with F^- ions. Once, the partial substitution of OH^- ions with F^- ions is allowed to occur, the existing H atoms of OH^- ions are strongly bonded to neighboring F^- ions owing to their higher affinity with respect to O atoms. Consequently, quite well-ordered HA structure results, i.e., crystallinity increases. In contrast, for W (0 – 40) % and Te (0 – 0.24) % doping, crystallinity decreases at low concentration, and then increases for higher concentration [89, 90]. In addition, no systematic change in degree of crystallinity is observed in the case of Cs doping (0 – 32) % [93]. Interestingly, the degree of crystallinity of HA nanorods is also found to decrease on doping with Eu^{3+} ions. A high level

of doping should be avoided to prevent the nano aggregation [34, 93]. Moreover, relative permittivity, AC electrical conductivity, antibacterial response and adjuvant activity have also been found to increase when HA nanorods were doped with W, Mo, Ag and Si metals, respectively [89, 91, 94, 137].

1.4.1.2. HA nanowires

Owing to the strong morphological dependence properties of HA nanocrystals, extensive efforts have been devoted to engineer the one-dimensional HA nanowires. High aspect ratio of nanowires leads unique mechanical properties, such as good elasticity and high flexibility which results in potential applications in various fields including, bone tissue engineering, filter paper for water purification, fire-resistant rope, catalytic paper, electrically conductive paper, magnetic paper, thermal insulation, anticounterfeiting application, tin phosphate anode, and biocoating etc. [11, 33, 140-151]. Although, number of synthesis routes, such as HT, ST, MW irradiation, MW assisted HT, sol-gel and template methods have been attempted. The synthesis of nanowires with high aspect ratio is quite a challenging task [11]. The most common template-based strategy has been adopted to synthesize HA nanowires. For instance, highly ordered HA nanowires array of 50 μm in length and 100 nm of diameter, were fabricated within the pores of aluminum oxide hard template after immersing the porous template into HA sol at 600°C for 6 h [152]. In another report, the HA nanowires of few μm in length were formed in presence of most popular cationic CTAB template [19]. It has been proposed that the growth of HA nanowires depends on the anisotropic charge distribution on the different faces of HA. CTAB can attach via electrostatic interaction with certain faces [i.e., (1 0 0)] of HA containing highly negatively charged ions as compared to face [i.e., (0 0 1)], containing positively charged ions. Such interaction promote the crystal growth of HA along c-axis direction by restricting the growth along a-axis direction, which lead to formation of HA nanowires under prolonged HT treatment [19]. However, the use of these templates are critical to health and environment,

and make the synthesis process costly, as mentioned previously. Therefore, Zhang et al.[153] produced ultralong HA nanowires up to mm scale in presence of environmental friendly mixed solvents of oleic acid, ethanol and water via ST method. The detailed mechanism behind the formation of HA nanowires has been proposed by Jiang et al.[154].

The set of chemical reaction between reactants occurred in reaction chamber are as follows:

First, the formation of calcium oleate precursor occurs through the two stages reactions [(1) and (2)] during initial stage [154]:

$$CH_3(CH_2)_7CH=CH(CH_2)_7COOH + NaOH \rightarrow CH_3(CH_2)_7CHQCH(CH_2)_7COONa + H_2O \quad (1)$$

$$2CH_3(CH_2)_7CH=CH(CH_2)_7COONa + CaCl_2 \rightarrow [CH_3(CH_2)_7CH=CH(CH_2)_7COO]_2Ca + NaCl \quad (2)$$

Further, the formation of HA nuclei takes place [(3) and (4)] under ST treatment at 180ºC[154]:

$$NaH_2PO_4 + 2OH^- \rightarrow PO_4^{3-} + 2H_2O + Na^+ \quad (3)$$

$$10[CH_3(CH_2)_7CH=CH(CH_2)_7COO]_2Ca + 6PO_4^{3-} + 2OH^- \rightarrow$$

$$Ca_{10}(PO_4)_6(OH)_2 + 20CH_3(CH_2)_7CH=CH(CH_2)_7COO^- \quad (4)$$

The oleate ions adsorb on the side faces of HA nuclei which restrict the growth along a-axis and allow the growth along c-axis. Consequently, the continuous ST heat treatment up to 18 h lead to the production of HA nanowires [154].

Because of reasonably higher value of aspect ratio of HA nanowires, number of research groups followed this method with some modification [17, 30, 33, 140, 141, 143-145, 147, 150, 154-161]. Yu et al.[162] used similar combination of precursors, but treated in MW oven to avoid few of the shortcomings of HT method such as energy consumption, expensive and longer reaction time, as already discuss above, and developed the nanowires with ultra-high aspect ratio, typically tens of millimeter. However, high cost of oleic acid is not ignorable. To resolve this situation, oleic acid has been replaced with peanut oil which contain the ~ 67 % of oleic acid. The micron sized HA nanowires has been formed at Ca/P ratio of 1:2 [163]. There are also many research articles, where the researchers controlled the wire shape of HA

nanocrystals even without using the organic solvent and template. As an example, Lin et al.[164] used hard precursor of similar morphology i.e., “xonotlite nanowires” which was treated hydrothermally in Na_3PO_4 solution to synthesize ultra-long HA nanowires with diameter of about 20 nm and length up to several μm. Also, Costa et al.[165] evolved the dissolution-precipitation route to transform the amorphous calcium phosphate NPs into HA nuclei under HT conditions, which subsequently, grow into HA nanowires with aspect ratio of about 50 – 80. For such growth of HA nuclei, two mechanisms were suggested- (i) Ostwald ripening process, where the larger crystals grow at the expense of smaller crystals in order to minimize the surface energy, and (ii) diffusion-controlled crystal growth, which can be explained as follows: The atoms in crystal structure of HA are arranged in such a way that interfacial energy of (0 0 1) face is higher than other faces. Under high concentration of amorphous calcium phosphate, it possesses significantly greater chemical potential than (0 0 1) face of HA. At this condition, 1-D growth of HA crystal occurs as a result of migration of metastable amorphous calcium phosphate towards (0 0 1) face of HA. On prolonging the HT time from 6 h – 16 h, 1-D growth continues from HA nanorod to nanowire morphology. This second mechanism is in good agreement with previously reported HA crystal growth mechanism [166]. In another study, Bramhe et al.[167] explained that the relative specific surface energy of different facet of HA crystal could be responsible for nucleation and growth of HA nanowires. Since different faces of HA adsorb different concentrations of OH^- ions due to difference in their surface energies that determine the rate of crystal growth and morphology of HA nanocrystals. On increasing the pH i.e., concentration of OH^- ions in the solution, the mobility of Ca^{2+} and PO_4^{3-} ions in nucleus decreases, which consequently, reduces the crystal growth. At this stage, OH^- ions act as a template, i.e., Ca^{2+} and PO_4^{3-} ions attached to that facet of HA nuclei where the concentration of OH^- is lower, which result in the formation of HA nanowires of aspect ratio ~10^2 [167]. In addition, Zhang et al.[25] also speculated the

mechanism behind the development of Si and Sr substituted HA nanowires of length/diameter up to 2 µm/60 nm by treating the Sr-containing calcium silicate (CS) precursor powder hydrothermally in Na_3PO_4 solution. It has been suggested that the Sr-CS particles erode with the release of Ca^{2+}, Sr^{2+} and SiO_3^{2-} ions in phosphate solution under HT treatment at 180^{o}C. With continuous release of these ions, supersaturation condition arises, and consequently, HA are nucleated on the eroded Sr-CS particle surface. On increasing the HT time up to 24 h, size of HA crystals increases along their lengths at the expense of continuously released ions. Meanwhile, the released Sr and Si ions from Sr-CS particles are also substituted with Ca^{2+} ions in HA crystal lattice. As a result, Si and Sr substituted HA nanowires are formed. Furthermore, Qi et al.[168] also prepared HA nanowires of diameter 30 nm and length up to several micrometers with the use of $CaCl_2.2H_2O$ and ATP disodium salt ($C_{10}H_{16}N_5Na_2O_{14}P_3$) as a Ca and P sources, respectively. All such results of HA nanowires are briefly summarized in Fig. 1.9.

As HA nanowires, produced without using any organic template/solvent, are only up to micrometer in length. Therefore, it can be clearly concluded that the organic solvent dependent synthesis of HA nanowires is more effective to achieve the dimension up to mm scale.

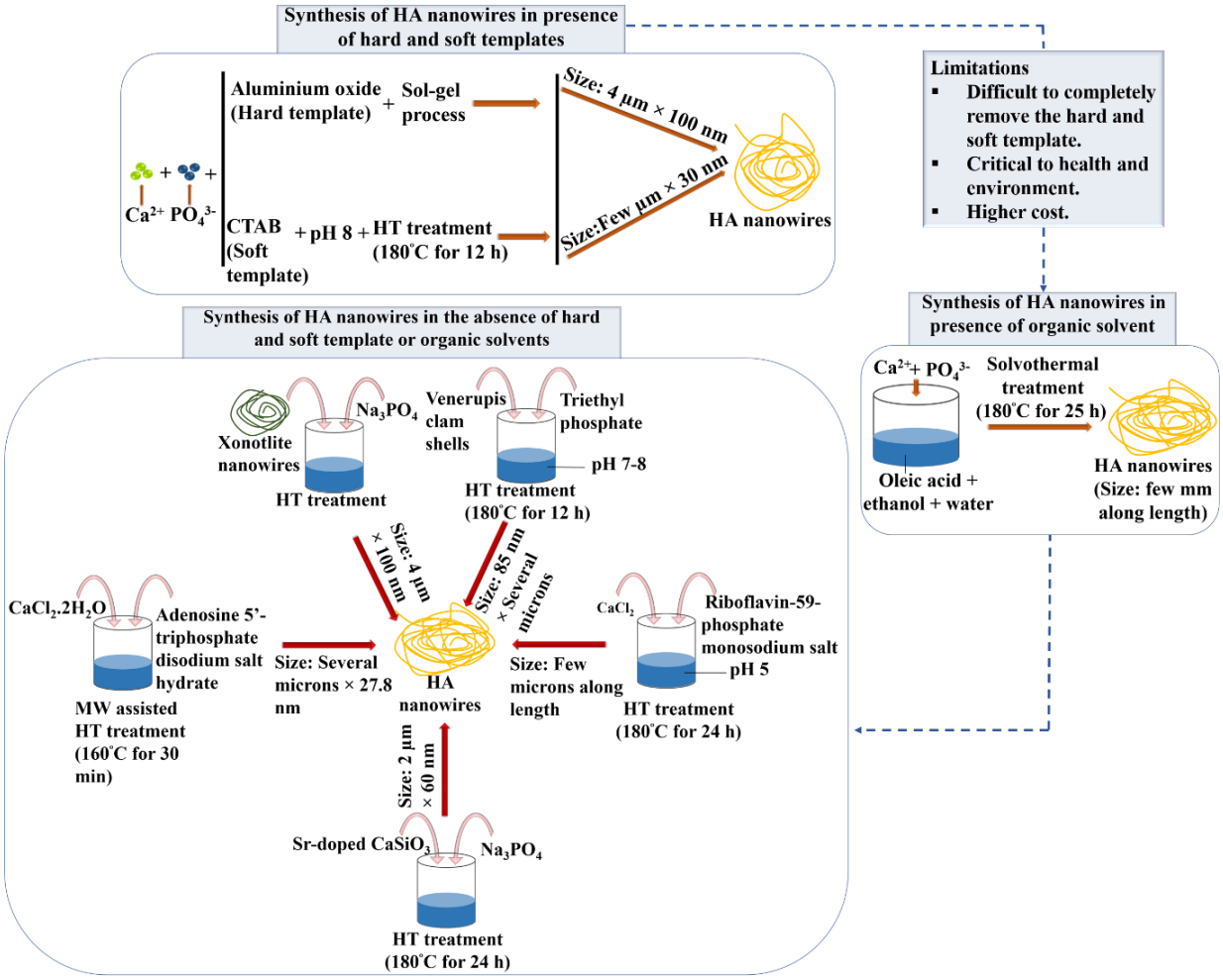

Figure 1.9. *Synthesis of HA nanowires with and without using organic solvent, to overcome the limitations associated with synthesis of HA nanowires in presence of hard or soft template [19, 25, 152, 153, 164, 165, 167, 168].*

1.4.1.2.1. The transformation of HA nanorods to HA nanowires

The role of various controlling parameters, such as HT time, temperature, pH of precursor solution and surfactant concentration on the transformation of HA nanorods to nanowires are also examined (Fig. 1.10). Costa et al.[165] transformed HA nanorods of aspect ratio of about 15, formed hydrothermally after treating amorphous calcium phosphate solution of pH 7.5 for 6 h, into HA nanowires of aspect ratio of up to 60 – 90 by successive variation in HT time from 16 h to 24 h (Fig. 1.10 A). After two years, Zhang et al.[25] demonstrated that short rod like HA nanocrystals formed after the HT treatment for 1.5 h, converted into nanowires of length

of about 2 μm on increasing the time up to 24 h. The increase in diameter of nanowires from 50 nm to 60 nm has also observed under similar conditions. On increasing the HT time to 3 days, length and diameter of HA nanowires further increased up to 2.5 and 70 nm, respectively (Fig. 1.10 B). The mechanism behind such transformation in morphology is already discussed above. In addition, Zhao et al.[26] formed HA nanowires at pH 5 and higher HT temperature of about 180^{o}C for 24 h instead of pH 9 having same HT condition (Fig. 1.10 C). In acidic conditions, the hydrolysis of RP biomolecules, used as an organic additive as well as phosphorus source, is relatively slow process, producing lower concentration of PO_4^{3-} ions. Therefore, a smaller number of HA nuclei formed at initial stage. On prolonging the HT time up to 24 h, the later formed PO_4^{3-} ions by hydrolysis react with Ca^{2+} ions at the end facet of HA nuclei, growing to HA nanorods and eventually, HA nanowires. On the other hand, at alkaline condition, the hydrolysis of RP biomolecules is quick, which, in turn, led to the higher concentration of PO_4^{3-} ions at initial stage of reaction. Therefore, massive number of HA nuclei formed at initial stage, which abruptly grow to HA nanorods. Furthermore, Nathanael et al.[19] observed that in the absence of CTAB, HA nanorods are obtained by treating the precursor solution of pH 8 hydrothermally at 180^{o}C for 12 h. However, with addition of CTAB of concentration of about 0.5 mmol, the length of nanorods begin to increase, and transformed into nanowire of few μm length at 1 mmol of CTAB concentration, while keeping the rest of experimental parameters unchanged. The mechanism for this transformation in morphology is also mentioned above. Moreover, longer HT time (12 h) offered better uniformity in the diameter of nanowires in presence of CTAB surfactant (Fig. 1.10 D). Therefore, it can be inferred that the longer HT time and higher HT temperature at acidic condition or lower basic condition is favorable for the growth of HA nucleus into nanowires.

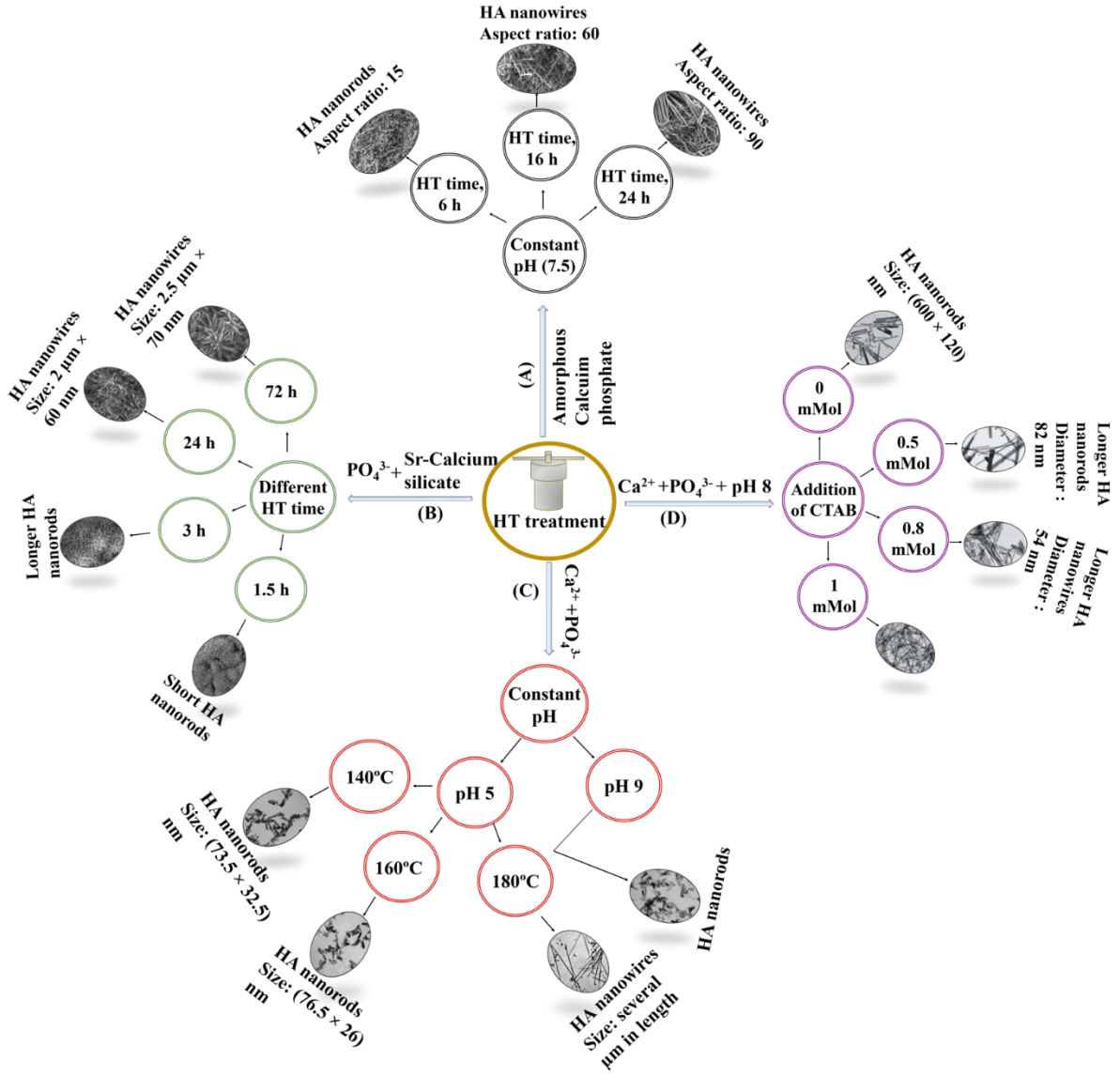

Figure 1.10. *Schematic illustrating the role of HT time (A and B), pH of precursor solution and HT temperature (C), and surfactant concentration (D) on the transformation of HA nanorods to HA nanowires. Longer HT time and higher HT temperature at acidic or lower basic condition is favourable for the growth the HA nucleus into HA nanowires. Scanning electron microscope (SEM) images are reproduced with the permission from publisher, Refs. [19, 25, 26, 165].*

1.4.1.3. HA nanofibers

Low mechanical strength and fracture toughness of HA due to its brittle nature, restrict its use in load bearing applications. Nanofibers are regarded as promising morphological structure to

improve the mechanical strength and fracture toughness of a brittle material, and also offer the superior reinforcing phase in the composites [169]. Therefore, the development of HA nanofibers becomes a powerful strategy to overcome the limitations associated with HA, which can be accomplished using wet synthesis methods like chemical precipitation, HT, MW irradiation, template route, sol-gel, electrospinning and electro blowing as well as dry synthesis methods like solid state and mechanochemical routes [170]. The quaternary water-in-oil microemulsion system, CTAB/cyclohexane/n-pentanol/water has been adopted to synthesize the HA nanofibers with the aspect ratio of up to ~1000. In this method, HA was nucleated within the CTAB reverse micelles. However, the formation of nanofibers does not occur within the pool of reverse micelles. In fact, HA grows to nano fiber-like morphology through the aggregation of tiny particles along c-axis direction during HT treatment (130 °C for 12 h) [171]. In another study, Shan Gao et al.[172] also used the CTAB surfactant. Although, different mechanism was proposed, i.e. the formation of short rod like nanostructures within cylindrical-shaped CTAB micelles, which, then combine to form HA nanofibers. Moreover, aspect ratio of HA nanofibers also increases from (20 – 33) with increasing the CTAB concentration from (0.45 – 3.0) g, which is in well agreement with previous discussion, i.e. CTAB is favorable organic additive to achieve the HA nanocrystals of high aspect ratio. It is also important to mention that Liu et al.[173] used the similar precursors as well as organic additive “oleic acid", as used by Jiang et al.[154], to fabricate the HA nanowires. Both research groups proposed the similar mechanism for the nucleation of HA. However, Liu et al.[173] controlled the morphology of HA nanocrystals to nanofiber under the HT condition (140ºC for 8 h), in which oleic acid plays a pivotal role as capping agent or structure directing agent in the formation of different morphological HA nanocrystals. By hydrophilic (– COOH functional group) part of oleic acid, it absorbed to a certain facet of HA through the coordination with Ca^{2+} ions, which render the HA facet hydrophobic due to alkyl chain of oleic acid. Meanwhile, Ca^{2+} ions

undergo reversible exchange reaction between oleate and phosphates. This process decides the release rate and quantity of Ca^{2+} ions as reactant, which eventually promote HA to grow along c-axis direction [173]. Few other organic molecules such as yeast extract and glutamic acid have also been used to control the growth direction of HA nanocrystals, and developed HA nanofibers of aspect ratio of up to 40.6 and 700, respectively [174, 175].

Since, the degree of flexibility of nanofibers is strongly related to their aspect ratio. Therefore, the evolution of the advanced technique is in continuous thrust with aim to achieve the aspect ratio of HA nanofibers, as high as possible. In view of this, Wang et al.[176], lately, applied similar strategy as reported by Wang et al.[128] i.e., template technique combined with liquid-solid solution strategy to design the HA nanofibers with aspect ratio of about ~10^4 in presence of environmental friendly surfactant, steric acid as a template under the ST conditions (Fig. 1.11 A). In this method, the sodium stearate is initially transformed into calcium stearate through the ion exchange between Na^+ and Ca^{2+} ions. Afterwards, the Ca^{2+} ions of calcium stearate interact with PO_4^{3-} and OH^- ions under high ST temperature of 180^{o}C and pressure to start the nucleation and control the crystal growth of HA nanofibers. Suchanek et al.[177] also adopted the distinct approach, i.e., prepared HA nanofibers from the Monetite [Dicalcium phosphate anhydrous (DCPA)] microplates in presence of EDTA as complexing agent and monoethanolamine as a pH regulator, phase and shape modifier (Fig. 1.11 B). Monetite phase with microplate morphology, obtained at pH less than 4.2, transformed to HA nanofibers of size (1.5 μm × 100 nm) with increasing the monoethanolamine concentration from 0.08 mol dm^{-3} – 1.65 mol dm^{-3} i.e., pH of the solution from 4.2 – 12 under the HT condition.

HA nanofibers have also been synthesized via the conventional electrospinning technique. Since, this technique most commonly offers the fabrication of continuous nanosized fibers of varieties of polymers and their composite materials [178]. Therefore, the electrospinning and calcination process have been combined to obtain the ceramic nanofibers by removing the

polymer phase from electrospun composite nanofibers of polymer and inorganic precursor sol [179, 180]. Lee et al.[181] synthesized gelatin-calcium phosphate microporous membrane by the electrospinning of gelatin-calcium phosphate composite sol. Such composite membrane is then treated thermally at 800°C to eliminate the gelatin, which subsequently, results the HA nanofibers (Fig. 1.11 C). However, electrospinning technique has some limitations such as slow production rate and further weight loss during thermal treatment [182, 183]. Therefore, Holopainen et al.[183] used electro blowing technique, combination of electrospinning process and air blowing, to fabricate HA nanofibers with improved production rate, higher yield and better controllability in fiber diameter. This technique uses both, electrostatic force and velocity of air to extrude the electrospinning solution into jets, and subsequently, into nanofibers [182]. Solid state and mechanochemical method have also been explored for the development of HA nanofibers. For example, Qiao et al.[184] synthesized HA nanofibers using solid state method by immersing the $CaAlB_3O_7$ powders into K_2HPO_4 solution. The mechanism for the formation of HA nanofibers is shown in Fig. 1.11 D [184]. Since, the framework of $CaAlB_3O_7$ is constructed by BO_4 chain structure [Fig. 1.11 D (a)]. On soaking in K_2HPO_4, the ion exchange between BO_4^{3-} and PO_4^{3-} can take place. [Fig. 1.11 D (b)]. Subsequently, the crystallization process of HA nanofibers can occur under heat treatment after combining the PO_4^{3-} to Ca^{2+} ions.

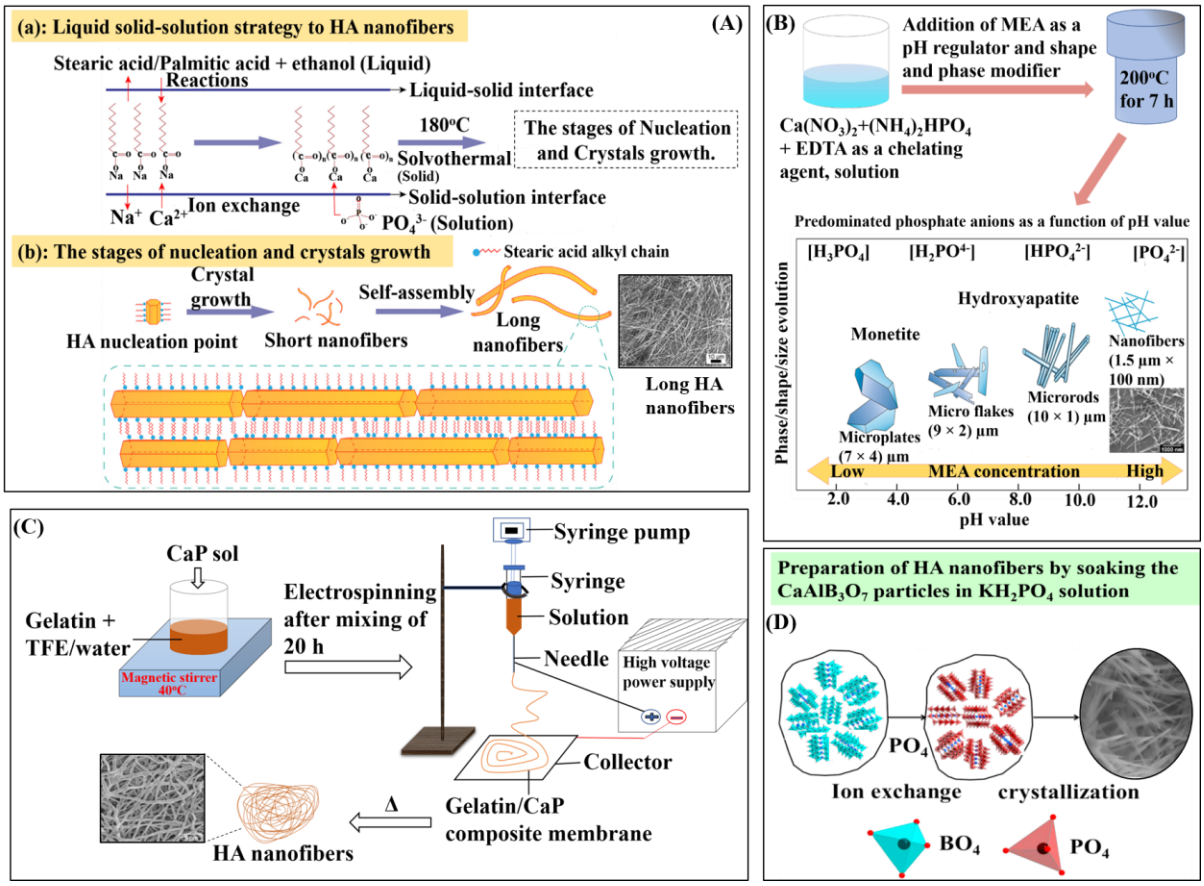

Figure 1.11. Various synthetic techniques for the development of HA nanofibers. *(A) Fabrication of HA nanofibers in presence of stearic acid/palmitic acid as a template under solvothermal condition: (a) liquid-solid solution strategy for HA nanofibers, and (b) stages of nucleation and crystal growth to transform the HA nuclei into long HA nanofibers, in which adsorbed stearate anions on the side faces of HA nuclei offers the crystal growth in form of fibers. Reproduced with the permission from publisher, Ref. [176]. (B) The conversion of Monetite into HA nanofibers in presence of monoethanolamine (MEA) as a pH regulator, phase and shape modifier and EDTA as a cheating agent [177]. (C) Fabrication of HA nanofibers through electrospinning technique. [181]. (D) The transformation of $CaAlB_3O_7$ particles into HA nanofibers after their immersion into KH_2PO_4 solution through the ion exchange mechanism. Reproduced with the permission from publisher, Ref. [184].*

1.4.1.4. HA nanotubes

The development of advanced fabrication route for HA nanotubes has gained remarkable attention as the nanotubular structure endow higher specific surface area than nanorods, which is beneficial to achieve a better performance in various field, particularly, in water purification, bone repair, adsorption, catalysis etc. [185]. In addition, it also paves the way to further optimize the correlation between morphology and properties including, mechanical and biological. In fact, it is well reported that single crystal nanotubular structure possesses better mechanical properties than nanorod structure. Although, various types of engineering methods for the synthesis of nanotubes have been explored such as, etching [186], template [187], and via Kirkendall effect (In this process, voids are initially start to form within the material through the inter diffusion of atoms of two different diffusion coefficients. Eventually, the hollow material forms due to coalescence of voids) [188]. Nevertheless, HA nanotubes offer major challenge to control the morphology. Among the aforementioned synthesis techniques, template mediated approach combined with Kirkendall effect has been widely adopted, owing to its well control nature in size, morphology and array. Porous anodic alumina, a chemically and thermally stable template, used to confine the growth of HA into nanotube form [189, 190]. In this case, membrane channels are not completely filled or blocked with CaP gel even after the long aging process or calcination (Fig. 1.12 A). Since, gel phase of CaP contains their major portion as hydrogen bonded water molecules, which only allow the specific amount of CaP loading on the pores of membrane. Upon calcination (500ºC), nucleation and growth of HA occurred at inner walls of channels, which results in membrane composite, enriched with HA nanotubes. Eventually, such composite membrane etched with NaOH to isolate HA nanotubes of diameter (140 – 350) nm and length up to micro meter. In another study, Singh et al.[191] successively soaked the electrospun composite nanofiber template, based on poly(caprolactone)-magnetite NPs, into $CaCl_2$ solution, phosphate solution and SBF to obtain

the mineralized composite fiber, which produced the magnetic HA nanotubes with inner shell width and thickness of about 650 nm and 137 nm, respectively, after removing the polymeric phase (Fig. 1.12 B). It is important to note that the use of these types of inorganic templates evolve the extra removal step process, which is not only contributing to increase the expenditure of energy but also cost. Therefore, to save the separate template removal step, Sun et al.[192] utilized $CaCO_3$ nanoneedles as a template and Ca precursor. The solubility of HA is much lower than $CaCO_3$ nanoneedles precursor. Therefore, owing to such high solubility difference between $CaCO_3$ nanoneedles and final product, Kirkendall effect assisted ion exchange method transformed $CaCO_3$ nanoneedles to HA nanotubes with length, inner diameter of both the ends and wall thickness of about 2 – 4 μm, 300 – 400 nm and 150 – 250 nm, and ~ 35 nm, respectively. On exposing the $CaCO_3$ nanoneedles in alkaline solution of phosphate anions and heat treatment, it eroded with the release of Ca^{2+} and CO_3^{2-} ions into the alkaline solution. With continuous release of these ions, the concentration of Ca^{2+} and PO_4^{3-} ions reached to over saturation value. In this condition, HA nucleated on the eroded surface of $CaCO_3$ nanoneedles. Though, $CaCO_3$ nanoneedles are only partially eroded, nanotubular form of HA are obtained.

Beyond assuring the energy savings and cost related to template removal step, other critical factors, such as toxicity etc. needs to be addressed. Since, the complete removal of template is a complicated process. Therefore, Guo et al.[193] adopted the biomimetic process and developed HA nanotubes in two steps (Fig. 1.12 C): (i) The gentle addition of organoamines in CaP precursor solution at pH lower than 8.2 allow the formation of regular dicalcium phosphate dihydrate (DCPD) plates, which then undergoes dehydration, and splits into dicalcium phosphate (DCP) nanorods, for the pH greater than 8.2; (ii) The step by step transformation of DCP nanorods to HA nanotubes while forming the HA nanorods intermediates, under HT treatment. The tubular structure initially starts to originate from the

tip of HA nanorods, which subsequently, spread from tip to centre, finally, convert whole rod to tubular form. Wang et al.[194] adopted this technique to prepare HA nanotubes based catalyst.

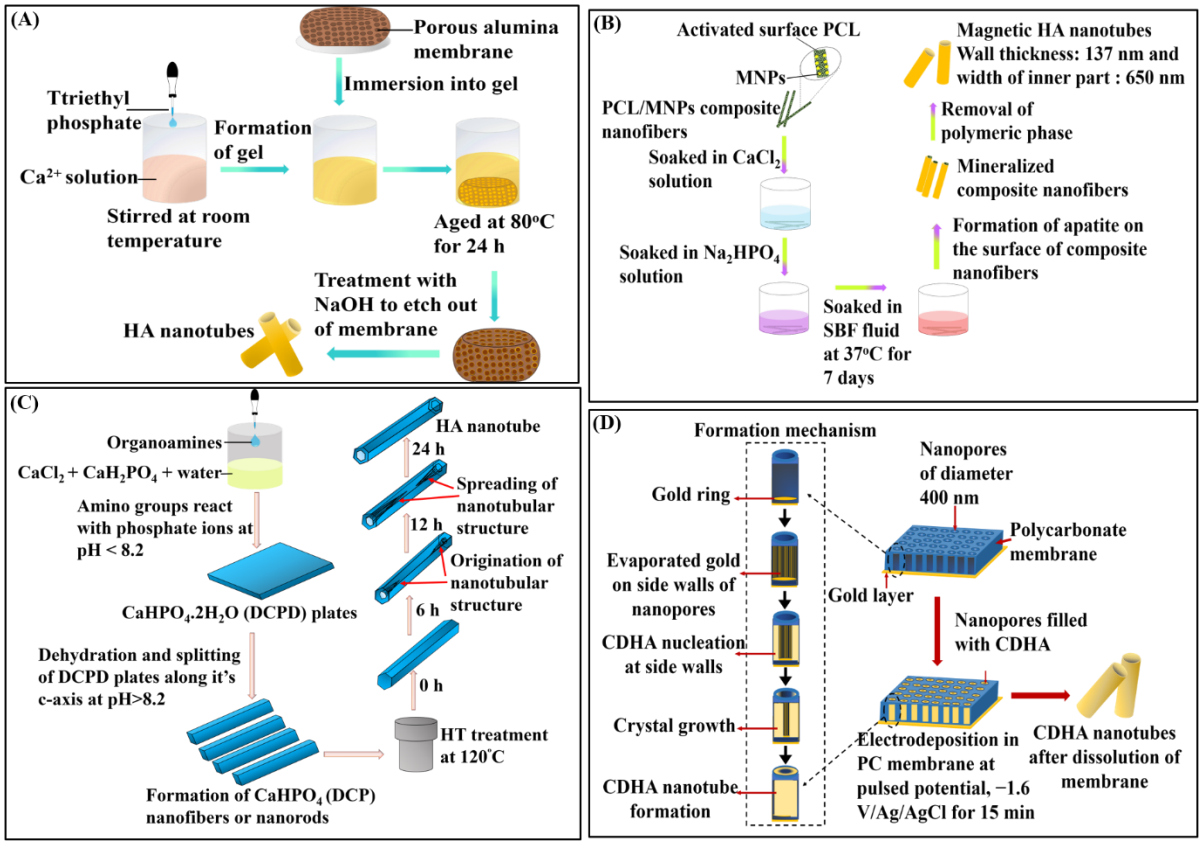

Figure 1.12. Synthesis techniques for the development of HA nanotubes. *(A) Fabrication of HA nanotubes in presence of porous anodic alumina membrane as inorganic template [190]. (B) The schematic illustration of synthesis process of HA nanotubes with the use of poly (caprolactone) (PCL)- magnetite nanoparticles (MNPs) composite nanofiber template [191]. (C) The biomimetic synthesis of HA nanotubes using organoamines as a controller or inducer [193]. (D) The electrodeposition process and key mechanism for the formation of CDHA nanotube, followed by the dissolution of composite membrane in dichloromethane [196].*

In contrast, Hui et al.[195] controlled HA morphology into nanotubular structure in absence of any template or additive using only 3 % of fluorine doping. At initial stage of process, CaF_2 forms, which is followed by the reaction with PO_4^{3-} ions into the solution during the HT

treatment, that lead to the production of F-substituted HA on the surface of CaF_2. Owing to anisotropic hexagonal symmetry of HA,[116] F-HA coated on CaF_2 surface is assumed to control the crystal growth like 1-D nanostructure. With complete consumption of CaF_2, hollow inner space left with surrounding HA, i.e., nanotube-type structure. Moreover, it was also found that the order of addition of F^- and PO_4^{3-} ions play a crucial role in the morphology of HA nanocrystals. Addition of F^- ions before PO_4^{3-} ions results in HA nanotubes. While, the opposite is true for the formation of HA nanorods.

Recently, template assisted pulsed mode electrodeposition method has also been introduced, to control the morphology of calcium deficient hydroxyapatite (CDHA) nanocrystals, i.e., CDHA nanotubes or nanowires [196]. As compared to conventional template method, morphology, size, and aspect ratio of HA nanocrystals can be better controlled with varying the membrane pore diameter and deposition time. The electrodeposition has been performed into nanopores of gold layered polycarbonate membrane at electric pulsed potential of -1.6 V/Ag/AgCl with current density of -120 mA/cm^2 for 15 min. Afterwards, CDHA nanotubes with aspect ratio from 9 – 25, are formed after the dissolution of CDHA filled membrane with diameter of 400 nm. While, HA nanowires of aspect ratio of about 21 – 53 results for the membrane with pore diameter of 200 nm. The electrodeposition process and growth mechanism for the formation of HA nanotubes is schematically presented in Fig. 1.12 D. The mechanism for such interesting variation in morphology with different pore diameter has also been speculated. The gold ring formed at the bottom of nanopores nucleates CDHA. Such CDHA nuclei grow from bottom to top direction within nanopores, which then transform to CDHA nanowires. Moreover, during electrodeposition, gold evaporated away from the bottom of nanopores and deposited at the side walls of nanopores. However, gold depositing area is wider in the membrane of pore dimeter of 400 nm than membrane having pore diameter of 100 or 200 nm. Therefore, for the

membrane of pore diameter of about 400 nm, CDHA nucleation begins at the side walls of nanopores, which eventually turn to CDHA nanotubes.

1.4.1.5. HA nanoneedles, nanobelts, nanowishkers and nanoribbons

Yubao el al.[44, 197] reported the synthesis of HA nanoneedles just after one month of their report on HA nanorods using almost similar HT condition as that for HA nanorods, except the glycerine as a dispersant. Instead, the fluorine ions are incorporated to control the crystal growth into the nanoneedles of crystal size of about (75 × 10) nm. Few reports are also available on the preparation of HA nanoneedles [116, 198-200]. The oil-in-water micro emulsion approach, composed of oleic acid (surfactant), water, ethanol and cyclohexane (oil phase), has been adopted by Ma et al.[198], wherein the nucleation of HA takes place at interface of oil droplets, opposite to above discussed water-in-oil microemulsion system (HA nucleated within the micelles). The freshly prepared HA nucleus, capped with oleic acid, moved from interface to within the oil phase and stabilized the oil droplet as surfactant. At HT temperature above 90ºC, i.e., 100ºC – 140ºC, these nuclei grew to nanoneedle-like shape with length from 80 – 100 nm to 200 nm, respectively. The growth mechanism of HA nanoneedles are explained using Fig. 1.13 A. There are few other interesting types of 1-D morphology of HA nanocrystals, such as HA nanoribbons, HA nanoblocks and HA nanowishkers which came into existence along with HA nanoneedles while exploring the influence of experimental conditions on the morphology of HA nanocrystals. For instance, Ito et al.[199] transformed the plate shaped DCP crystal to different morphological HA nanocrystals such as HA nanoneedles, HA nanofibers and HA nanosheets, with alteration of pH of the precursor solution and phosphate ions concentration (Fig. 1.13 B). In case of HA nanoneedles, spindle shaped HA nano seeds initially formed on the surface of DCP crystals by solid-solid phase transformation of DCP crystal under highly basic condition, i.e., at pH 13, which then grew to bundles of HA nanoneedles. At pH 9, the initial stage is almost similar, i.e., HA fibrous seeds nucleated on DCP surface with the

dissolution of phosphoric acid. Randomly oriented long HA nanofibers resulted on DCP surface with the crystal growth of such fibrous seeds with time. HA nanoneedles and HA nanofibers formed with the direct transformation of DCP crystal through the dissolution of phosphoric acid. On the other hand, HA nanosheets obtained with solid-liquid-solid transformation of DCP crystal due to presence of excess amount of phosphate ions, which suppress the direct transformation of DCP precursor to HA. Instead, complete dissolution, and then subsequent crystal growth led to formation of HA nanosheets. In another study, Kobayashi et al.[200] grown HA seeds in SBF at 38ºC for 24 h into their respective nanoneedles, nanoribbons and nanosheets at pH 6.5, 7 and 7.5, respectively (Fig. 1.13 C). At pH 6.5, the crystal growth of HA seeds proceeds to their habitual crystallographic direction, c-axis, which consequently, produces needle like nanostructures. However, with increasing the pH of precursor solution up to 6.5 or 7.5, degree of supersaturation condition enhances. Also, 2-D crystal growth dominates the 1-D crystal growth with increased pH level. At initial stage of reaction (within 10 min), needle like particles produced. Subsequently, these growing particles coalesced within 30 min to form HA nanoribbons or nanosheets. This indicate that higher degree of supersaturation and enhanced crystal growth rate with increased pH level (from 6.5 to 7 or 7.5) are mainly responsible for the growth of HA seeds to 2-D type nanostructures. The nanosheets, nanoribbons and nano blocks shaped HA nanocrystals are also obtained in presence of urea, together with altering the HT temperature, 120°C, 150°C and 180°C [201]. In this case also, higher degree of supersaturation with increased HT temperature up to 150°C (because of increase in pH of solution with decomposition of urea at higher temperature) is responsible for the formation of HA nanoribbons. Further, increase in HT temperature up to 180°C reduces the growth ratio along c-axis to a-axis (or b-axis) of HA via the Oswald repining mechanism, which results in nano blocks like morphology. Zhou et al.[202] observed that there is conversion of HA nanoflowers into their nanowishkers morphology on the substitution of Ca^{2+} ions of HA

with Zn^{2+} ions. Few authors also reported the nanobelts like HA morphology. However, their growth mechanism is still not clear [23, 203].

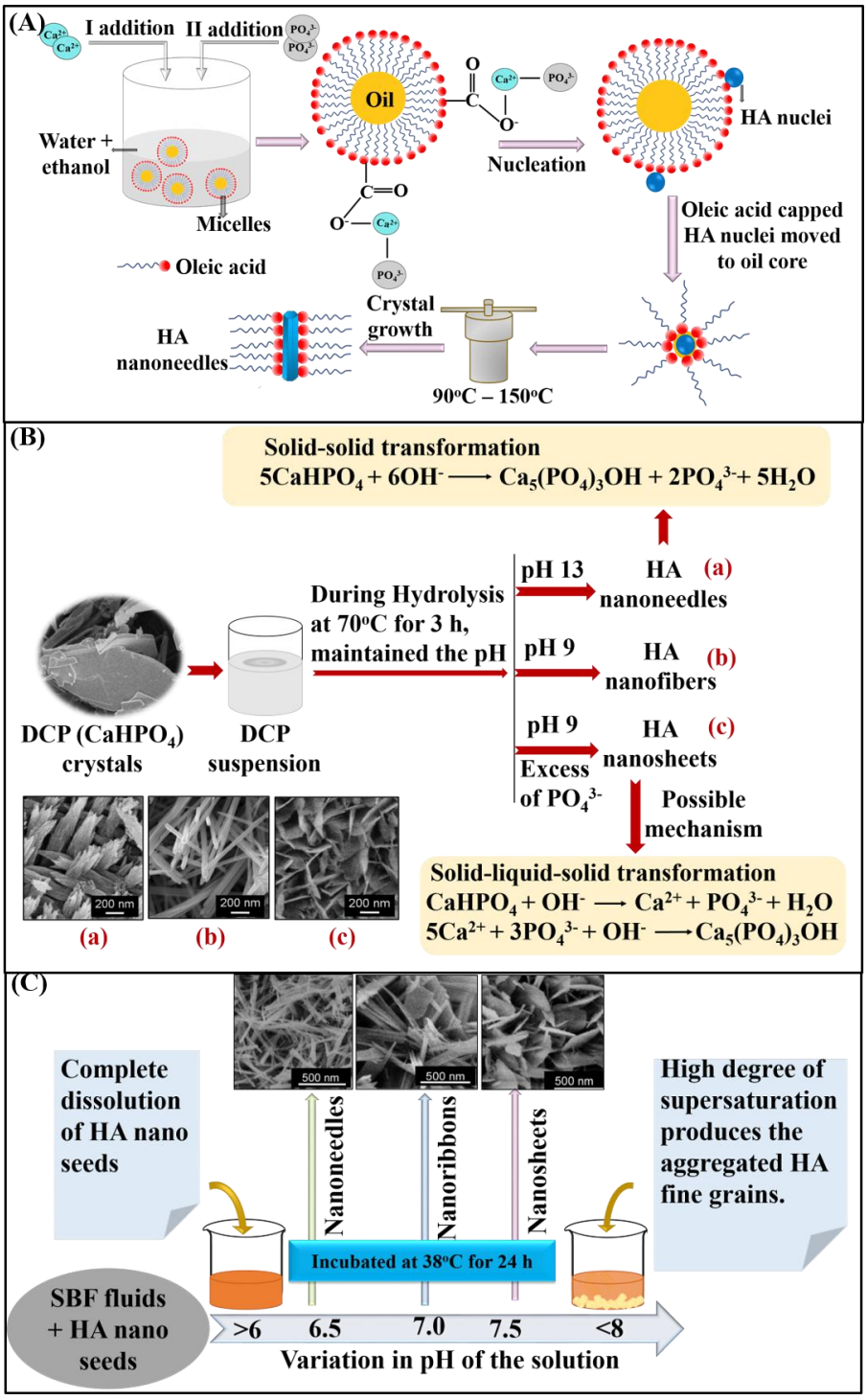

Figure 1.13. Techniques for the development of HA nanoneedles and nanoribbons. *(A) Oil-in-water microemulsion system for the synthesis of HA nanoneedles [198]. (B) pH and ionic concentration dependent fabrication of various morphologies of HA nanocrystals, such as HA needles, HA nanofibers and HA nanosheets through the hydrolysis of solid dicalcium phosphate (DCP) crystal in alkali solution. The SEM images are reproduced with the*

permission from publisher, Ref. [199]. (C) The transformation of HA nano seeds to HA needles, HA nanoribbons and HA nanosheets in SBF under the different pH conditions. The SEM images are reproduced with the permission from publisher, Ref. [200].

1.4.2. Synthesis of 2-D HA nanocrystals

1.4.2.1. HA nanoplates

It is known that HA nanoplates are the mineral components of our natural bone. Therefore, the development of 2-D HA can be recognized as more promising choice over to 1-D HA to accomplish the architectural resemblance with bone [204]. Although, few attempts have been made recently to develop the morphology of HA to mimic the bone-like apatite. Nevertheless, the development of such 2-D HA is in continuous thrust.

The template mediated processing route has been recognized as most promising approach to control the morphology of developed nanostructures. Similar strategy has been adopted to confine the growth of HA crystals into respective nanoplates using number of techniques, such as chemical-precipitation, HT, MW, and sol-gel methods [22, 204, 205]. Zuo et al.[205], for the first time, used anionic surfactant, SDS, as a template to form HA nanoplates with lamellar structure. Such synthesis process was adopted by number of research groups [204, 206-210]. Among them, Wan et al.[204] suggested the mechanism of formation of lamellar HA nanoplates (Fig. 1.14 A), i.e., the nucleation and growth of HA nanoplates can occur within the layer pre-shaped SDS micelles under thermal conditions (reflux at 83ºC for 24 h). Importantly, lamellar form of HA nanoplates do not dispersed well, while designing the composites. Therefore, Luo et al.[208] exfoliated the lamellar HA into individual respective nanoplates by intercalating the glucosamine (Fig. 1.14 A).

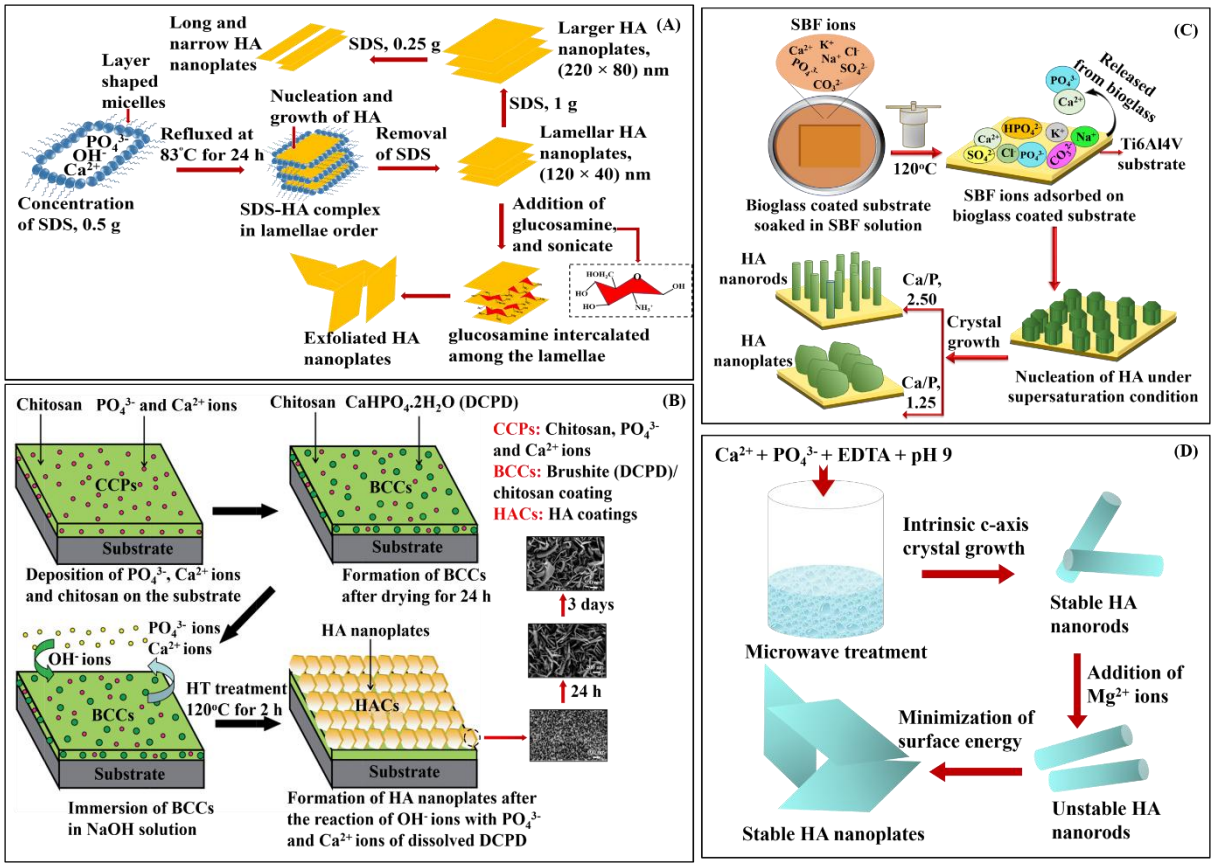

Figure 1.14. Various fabrication techniques for the development of HA nanoplates. *(A) Synthesis of lamellar HA nanoplates in presence of SDS template; exfoliation of lamellar HA nanoplates by the addition of glucosamine; variation in the size of HA nanoplates as a function of SDS concentration [204, 208]. (B) Transformation of BCCs to HACs having oriented nanoplate arrays on Ti6Al4V substrate. Reproduced with the permission from publisher, Ref. [217]. (C) Transformation of bioglass coating (on Ti6Al4V substrate) to rod and plate-like HA nanocrystals coating by soaking the bioglass-coated Ti6Al4V substrate into two different concentrations of SBF having Ca/P ratio of 2.50 and 1.25, respectively, at 120ºC [218]. (D) The effect of Mg doping on the drastic change in morphology of HA nanocrystals from rod to plate form [27].*

In another study, Zuo et al.[22] developed HA nanoplates with the size of about 300 – 400 nm in presence of PEG template at a pH of 9 via chemical precipitation method. The detailed mechanism is already mentioned previously. In addition, the monomer of PEG, ethylene

glycol, was also used as a crystal growth controlling additives to facilitate the formation of HA nanoplates [211]. There are also few reports, where biomimetic approach has been adopted. Since, based on the existing theory for biomineralization process of natural bone, collagen, which is 90 % of total organic content of natural bone, act as a template for HA nucleation due to their unique 3-D structure. The collagen molecules are arranged in such a way that holes are created between the neighboring molecules, which provides the nucleation site for the formation of HA nanocrystals in natural bone [212-214]. Moreover, noncollagenous protein, such as againine, aspartic acid lysine and glutamic acid [covers less than 10 % of total organic contents in natural bone tissue] also affect the size and morphology of HA [212, 215, 216]. In this perspective, Tsetsekou et al.[216] used collagen or chitosan as a template along with the presence of amino acid "L- arginine" to develop the bone-like HA nanoplates at biomimetic temperature of about 40^{o}C under alkaline condition. Similarly, Guan et al.[217] also mimicked the formation mechanism of HA in natural bone, where the precursor solutions [Ca^{2+}, PO_4^{3-} and chitosan (CCPs)] were initially deposited on Ti6Al4V substrate. Such CCPs were transformed into the brushite (DCPD)/chitosan coatings (BCCs) after 48 h of drying. Further, Ti6Al4V substrate with BCCs were treated hydrothermally in NaOH solution to transform into Ti6Al4V substrate with nanoplates-shaped HA coating (HACs) via dissolution-precipitation mechanism (Fig. 1.14 B). Under this condition, DCPD dissolves and releases the Ca^{2+} and PO_4^{3-} ions into the solution, which subsequently, react with OH^- ions to form the plate-like nano HA on the substrate. It has been noted that chitosan remains in coatings, because the chitosan possesses limited solubility in NaOH solution owing to stereo regularity and hydrogen bonding among chitosan molecules, and $-NH_2$ functional group of chitosan can act as nucleation site for apatite formation. After one year, Chen et al.[218] also followed the same strategy for the conversion of bioglass-coated Ti6Al4V substrate to HA nanocrystals (nanorods and nanoplates) coated substrate (Fig. 1.14 C). In this process, bioglass coatings are

successively soaked into SBF and treated hydrothermally at 120ºC for 12 h and 2 days respectively, via dissolution-precipitation mechanism, to convert into HA nanocrystals coating with oriented rod or plate like arrays. Green synthesis approach has also been adopted by Sundrarajan et al.[219] to develop the nanoplate morphology of HA, wherein tannin enriched "Moringa oleifera" plant extract was used as a chelating agent along with the presence of 1-butyl-3-methylimidazolium tetrafluoroborate ([BMIM]BF_4) ionic liquid as a template. The –OH groups of tannin bonded with Ca^{2+} ions to form the tanninate-Ca^{2+} complex via conjugation effect. Such chelate complex further binds to phosphates anions, which lead to nucleation of HA. [BMIM]BF_4 was attached to HA-tanninate complex through hydrogen bonding, restricting the vertical growth of HA. As a result, plate-shaped HA nanocrystals were obtained upon calcination at 400ºC. Other biocompatible organic additives such as amino acid [220], glutamic acid [221, 222], urea [223], and dodecenylsuccinic anhydride [224] have also been utilized to control the morphology of HA into nanoplate-like structures.

Few studies varied the experimental parameters including calcination temperature, HT temperature and time, and concentration of organic additives to achieve the optimal condition for the formation of HA nanoplates. Cabrera et al.[221] suggested that the morphology of HA nanocrystals can also be changed with glutamic acid concentration. It has been demonstrated that on increasing the concentration of glutamic acid, most of the Ca^{2+} ions take part in chelate complex formation by interacting with carbonyl group of glutamic acid. These complexes hinder the crystal growth along the [010] direction. Whereby, the growth of the crystals proceeds only in [001] direction, which consequently, results in the formation of nanofibers. Inversely, at low concentration, few Ca^{2+} ions in column could not form chelate complex. As a result, crystals growth occurs in nanoplate form. However, Wan et al.[204] revealed that the lamellar HA nanoplates become larger in size from (120 ± 20) – (40 ± 10) nm to (220 ± 20) – (80 ± 10) nm on increasing the SDS concentration from 0.5g to 1g. With decrease in SDS

concentration to 0.25 g, lamellar structure converted into rod shape, as SDS is not able to self-assembled into lamellar micelles at this concentration (Fig. 1.14 A). In another study, Guan et al.[217] reported the influence of HT time on morphology of HA nanoplates. It has been elucidated that the width or length of HA nanoplates gradually increases with increasing the HT time from 3 h to 3 days (Fig. 1.14 B). At initial stage of reaction, large number of Ca^{2+} and PO_4^{3-} ions, released from BCCs, take part in the formation HA nuclei rather than crystal growth. With time, concentration of reactants decreases, which, in turn, promotes the crystal growth as compared to the formation of HA nuclei. Therefore, the size of HA nanoplates increases with varying the HT time from 3 h to 3 days. In addition, Chen et al.[218] found that with altering the Ca/P ratios of SBF solution from 2.5 to 1.25, morphology of HA coating, formed on surface of Ti6Al4V substrate after soaking the bioglass-coated titanium substrate into SBF solution at HT temperature of 120ºC, transforms from nanorods to nanoplates-like HA nanocrystals (Fig. 1.14 C). At Ca/P ratio of 2.5, the concentration of Ca^{2+} ions, attach to side faces (a- or b-axis) of HA crystal, are larger than PO_4^{3-} ions (bind to end faces of HA crystal), which consequently, favors the crystal growth to nanorods morphology. In contrast, concentration of PO_4^{3-} ions, bind to end faces of HA nucleus, is higher in case of SBF with Ca/P ratio of about 1.25. Therefore, HA crystal growth proceeds to nanoplate-like morphology. Moreover, the bioglass-coated Ti6Al4V substrate was also soaked in SBF with Ca/P ratio of 2.5 at 37ºC which formed the plate shaped HA coating with low crystallinity. Furthermore, Mori et al.[224] suggested that HT temperature and time, and concentration of Ca ions are essential parameters to control the morphology and Ca/P ratio of HA nanoplates. It has been concluded that appropriate Ca^{2+} ion concentration, HT temperature and time to achieve the clear plate like morphology, with controlled Ca/P ratio close to 1.67, are 1.0 $mol.dm^{-3}$, 180^{o}C and 2.5 h, respectively.

Besides, aforementioned experimental parameters, there is also one quite interesting result on the role of doping to control the morphology of HA nanoplates, as reported by Mishra et al.[27] (Fig. 1.14 D). In this study, the consequence of Mg doping has been demonstrated to be dominant over EDTA surfactant to confine HA crystal growth into plate form. The addition of only 0.6 mol % of Mg in HA results in exciting change in the morphology from rod-like to plate-like HA nanocrystals. In case of Mg doped HA, the driving force acts in material in such a way that it makes Mg doped HA nanorods unstable with higher surface energy. In order to minimize the surface energy of Mg doped HA nanorods, it transforms to more stable nanoplates structure. In another report, Luo et al.[210] revealed that the degree of ordering of Se doped HA lamellar nanocrystals decreases on further elemental doping of Gd from 1.2 mmol to 4.6 mmol.

Despite of number of synthesis routes to obtain HA nanoplates, morphological control is quite difficult in comparison to 1-D HA nanocrystals. The inherent nature of HA is to grow along the c-axis direction, which leads to development of 1-D morphology. To restrict the HA crystal growth along c-axis and direct it along the a- or b- axis i.e., to develop the HA nanoplates, unique morphological controlling conditions are required. Therefore, the development of advanced synthesis routes to fabricate the HA nanoplates are still in continuous thrust.

1.4.2.2. HA nanosheets

As far as the development of HA nanosheets are concerned, only a few articles are available [199-201, 225-231]. In contrast to the synthesis of other HA nanostructures, most of the literature reports suggested that the development of HA nanosheets are based on the combination of HT and template methods. For example, Xiao et al.[226] designed laminated form of c-axis directed carbonated HA nanosheets with the synergistic action of biomacromolecule “succinylated gelatin” and surfactant “CTAB micelles” as template, via HT method. In early stage of HT reaction, succinylated gelatin electrostatically combined to Ca^{2+}

ions through their COO^- groups. These complexes further attached to PO_4^{3-} ions, which led to the nucleation of DCPD phase. Under the effect of succinylated gelatin, attached along their a- and b-faces, these DCPD nuclei grew as flaky-like nanostructures. CTAB molecules are also attached to succinylated gelatin via electrostatic attraction. With increasing the concentration of CTAB above CMC (1.05 mM), their molecules began to self-assemble into lamellar-like micelles. With the help of these micelles, DCPD nano flakes self-arrange to lamellar structure. As reaction proceeds, the pH of aqueous solution also gradually increases, which, in turn, allow initially precipitated DCPD phase to react with OH^- ions, which forms more stable phase of octa calcium phosphate. Eventually, it transformed to carbonated HA after prolonged reaction time (48 h), while morphology is intact. In another study, Qi et al.[227] and Zhao et al.[229] used the biomacromolecule, DNA and hemoglobin, respectively, as a template to form HA nanosheets based microspheres under HT conditions. The mechanisms for the formation of HA nanosheets using DNA template are as follows (Fig. 1.15 A); (i) the formation of micelles by self-assembly of number of DNA molecules; (ii) the adsorption of Ca^{2+} ions on the surface of micelles through the electrostatic attraction with negatively charged DNA molecules; (iii) following the incorporation of PO_4^{3-} ions, nucleation and further growth of HA nuclei occur into HA nanosheets on the surface of micelles; (iv) arrangement of synthesized HA nanosheets into porous microspheres to reduce the surface energy of HA nanosheets; and (v) hydrolysis of DNA under HT conditions to form the nanosheet-based porous hollow microspheres. Zhong et al.[230] developed HA nanosheets by abalone shell ($CaCO_3$) with the help of ionic surfactant CTAB and SDS via HT method. In this case, the influence of $CaCO_3$ is significantly higher than surfactant in controlling the growth of HA nanosheets i.e., $CaCO_3$ is acting as template for the formation of nanosheets. Therefore, HA nanosheets crystallize around the $CaCO_3$ surface (Fig. 1.15 B).

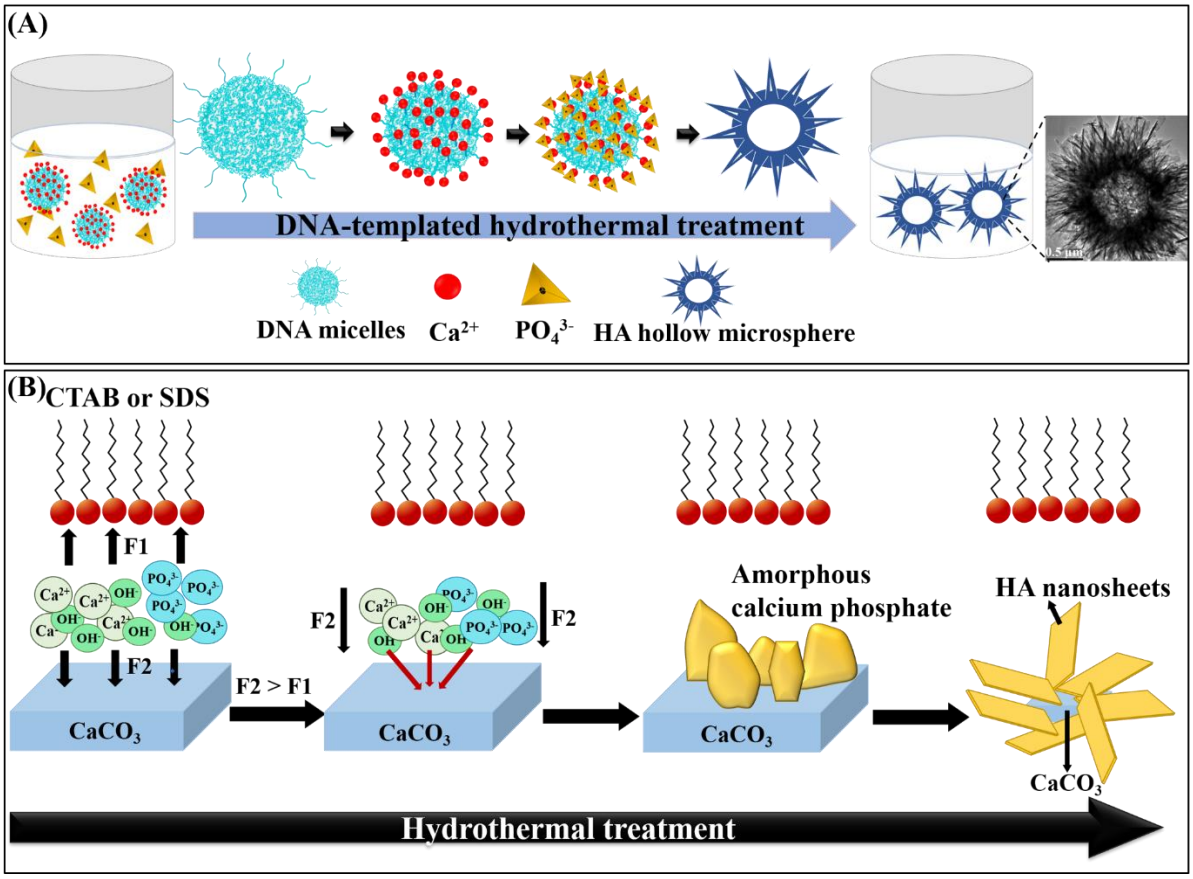

Figure 1.15. Synthetic methods for the fabrication of HA nanosheets. *(A) The HT synthesis of nanosheet-based hollow microsphere in presence of DNA template. The high-resolution field emission scanning electron microscope (HFESEM) image of HA nanosheets based microsphere are also shown as inset. Reproduced with the permission from publisher, Ref. [227]. (B) The conversion of abalone shell ($CaCO_3$) powder to HA nanosheets in presence of ionic surfactants (CTAB or SDS). In this, $CaCO_3$ is acting as a template, and therefore, crystallization of HA nanosheets, accelerated by CTAB or SDS, take place around the surface of $CaCO_3$ under the HT treatment. Reproduced with the permission from publisher, Ref. [230].*

Interestingly, Kobayashi et al.[200], Ito et al.[199], Lin et al.[225], Manoj et al.[232] and Zheng et al.[201] also fabricated HA nanosheets without the use of any organic additives, surfactant or template. The detailed mechanism for the production of HA nanosheets, by Ito and Kobayashi et al. was already elucidated in previous section (Figs. 1.13 B and C) [199, 200]. Lin et al.[225] mimicked the biological HA, which is co-substituted with various essential trace

elements such as Na, K, Mg, F and Cl as well as CO_3^{2-} ions. Sheet like HA nanostructures of thickness of about 60 nm, width of about 3 – 5 µm, and length of up to 20 µm, were developed after 0.5 h of HT reaction at 120ºC. With continuing HT reaction (0.5 h), HA nanosheets grew along their length and width with the expanse of smaller crystals, which lead to complete disappearance of smaller HA nanosheets. In 1 h, these nanosheets aggregated in besom like shape to reduce their surface energy in the solution. On further reaction (3 h), HA nanosheets were self-organized as flower-like structures. Eventually, much more addition of HA nanosheets into flower-like structure with prolonged reaction time (24 h) resulted the formation of 3-D HA microspheres.

1.5. Biomedical applications of HA nanocrystals

1.5.1. Bone tissue engineering

In the case of large human bone defects, mainly originated by degenerative bone diseases (e.g., arthritis, osteonecrosis, osteoporosis), infection, bone fracture, resection of bone tumor, surgical, bone cancer and trauma etc., the self-repairing nature of bone becomes futile [233, 234]. Therefore, the necessity of synthetic bone graft has been realized. Autologous bone grafting technique is considered as a ‘gold standard’ in order to treat the bone defect due to its excellent immunological compatibility and osteoinductivity. However, there is associated disadvantages such as infection, secondary damage, donor-site morbidity, and immunogenic response etc. [235, 236]. Few alternatives, including allografting and xenografting techniques have been evolved, which also encompasses number of issues, including potential infection, immunogenic rejection, and disease transmission risks, which drove the focus of researchers towards advanced technological development [237]. Fig. 1.16 (A) depicts both, advantages and disadvantages of all the above-mentioned traditional bone defect repairing techniques as well as driving force towards the further development of advanced technique i.e., bone tissue engineering.

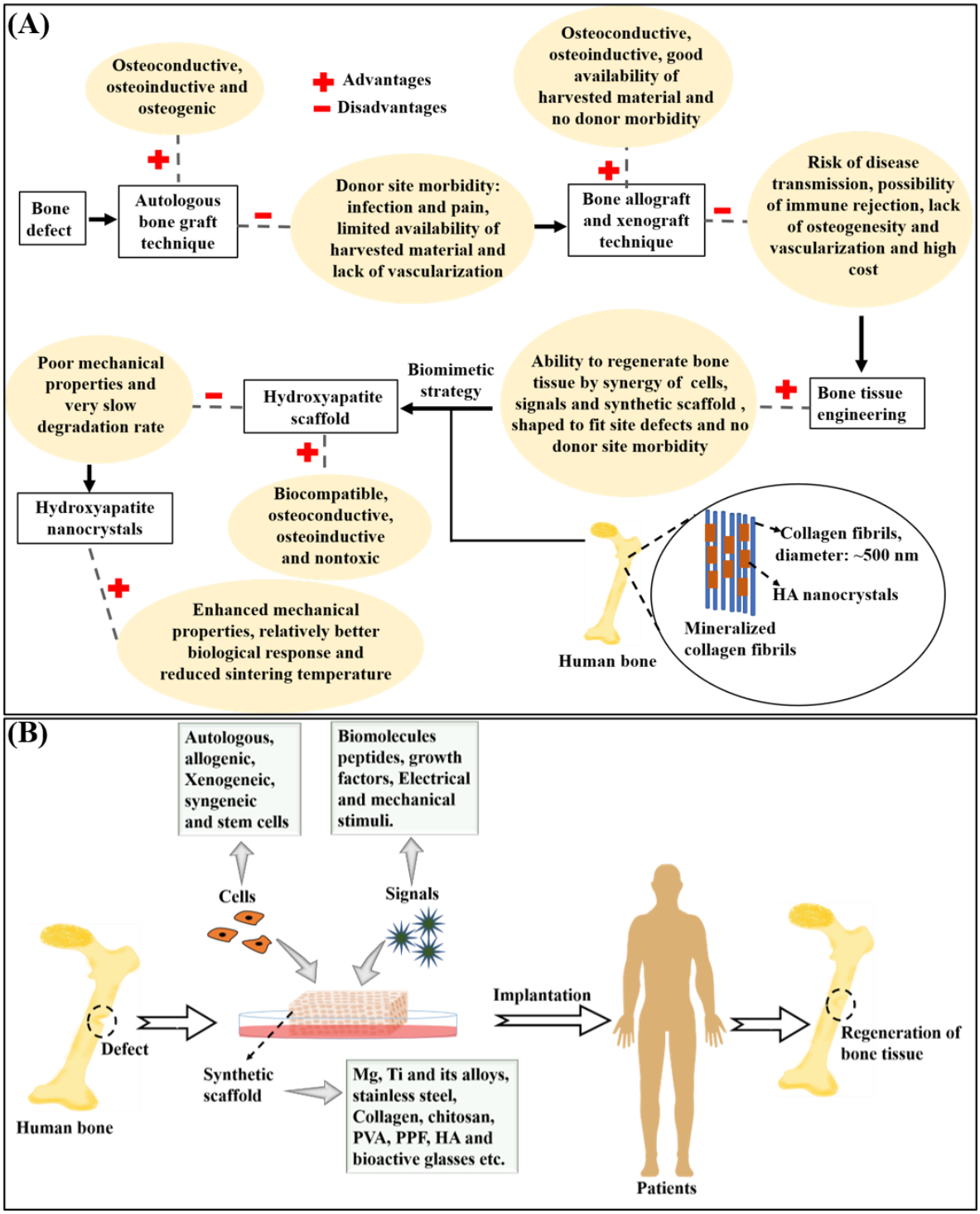

Figure 1.16. The basic idea behind the development of bone tissue engineering. *(A) Advantages and disadvantage, associated with conventional bone defect repairing techniques for defect repair, and (B) Fundamentals of bone tissue engineering.*

Bone tissue engineering approach attracted appreciable attention as a new therapy to regenerate new tissues and to reconstruct the damaged bone with the synergistic effect of cells, signals

and synthetic scaffolds [236]. The fundamental principle behind the bone tissue engineering is presented as Fig. 1.16 B. Synthetic scaffolds, also called as temporary natural bone extracellular matrix or transplant, must mimic or replicate the structure, composition, mechanical properties, porosity and surface features of extracellular matrix of natural bone. Such a mimicking approach offers the microenvironment to support the cell adhesion, proliferation, differentiation, migration and development of new tissues [234, 238]. The ideal scaffold material should be osteoinductive, osteoconductive, biodegradable and good antibacterial agent, so that implanted scaffold could gradually degrade, as new bone tissue grows within scaffold, and eventually completely replaced by newly formed bone tissue without any bacterial infection [236].

Number of biomaterials has been developed as a biocompatible artificial scaffold for tissue engineering applications. Among them, HA nanocrystals-based scaffolds have been demonstrated to be promising materials in repairing of damaged bone, due to its similarity (structurally and chemically) to the inorganic component of natural human bone [14].

Although, many research articles suggested that HA nanocrystals, such as nanorods [17, 18, 64, 75, 86, 90, 239, 240], nanoplates [14], nanowires [17, 141, 241, 242], nanotubes [190], and nanofibers [243, 244], can be a potential scaffold to promote the bone regeneration. Nevertheless, most of the researchers focused on the HA nanocrystals-based composites with the aim of mimicking the composite nature of bone to achieve the desirable biological and mechanical properties for bone regeneration. Various types of polymers have also been used as matrix, to design the HA- nanocrystals reinforced polymer composites scaffold, which include collagen [241, 245], collagen nanofiber [28, 246], chitosan [142, 247], nylon nanofiber [14], polyvinyl alcohol (PVA) [248], polycaprolactone (PCL) [249, 250], polypropylene (PP) [251], polylactic acid (PLA) [244, 252, 253], and PLA/chitosan [254]. Majority of such reports

are focused on HA nanocrystals/collagen composite as a scaffold to promote the regeneration of bone tissue, because such combination offers the similar composition, as living bone.

In addition, few other materials are also incorporated to further accelerate the bone healing performance of biomimetic HA nanocrystal-based composite scaffolds. For example, Hou et al.[248] converted nano HA/PVA into magnetic (m) nano HA/PVA by coating the nano HA with osteoconductive Fe_2O_3 NPs and observed that the proliferation and osteoblastic adhesion is highly susceptible in case of m-nano HA/PVA as compared to that of nano HA/PVA. Since, Fe_2O_3 NPs support the protein (e.g., fibronectin and vitronectin) adsorption on scaffold surface, which, in turn, bind with integrins, expressed by osteoblast cells, to promote the osteoblastic adhesion. In the same year, Liao et al.[251] used the hybrid multi-walled carbon nanotubes-HA nanorods (MWCNTs-nHA) as the reinforcing material instead of only HA nanorods to fabricate MWCNTs-nHA/PP composite scaffold. Significant enhancement in the tensile strength, stiffness, impact strength, cell viability and proliferation activity of MWCNTs-nHA/PP composite is observed as compared to nHA/PP scaffold. Such improvement in impact strength of MWCNTs-nHA/PP was ascribed to high flexibility and large failure strain of MWCNTs. Fig. 1.17 (A) clearly reveals that the degree of osteoblastic adherence on PP scaffold notably increases when it successively reinforced with MWCNTs and MWCNTs-nHA. The enhanced osteoblastic adherence was due to the graphitic structure of carbon nanotubes (CNT) and its high surface area, which allows adsorbing the significant number of proteins molecules.

Mg and Si elements are known to be potential stimulators for osteogenic and angiogenic differentiation of stem cells [255, 256]. Sun et al.[142] used magnesium silicate (MS) as osteogenesis and angiogenesis promoter to develop HA nanowires-MS/chitosan composite scaffold, where HA nanowires-MS/chitosan scaffold significantly stimulate the bone regeneration and formation of new blood vessels, *in vivo*, in comparison to chitosan and HA

nanowires/chitosan scaffolds [Figs. 1.17 (B) and (C)]. Moreover, HA nanowires-MS/chitosan scaffolds also confer the better cell adhesion, proliferation and differentiation of mesenchymal stem cells, *in vitro,* due to sustained release of Mg and Si ions.

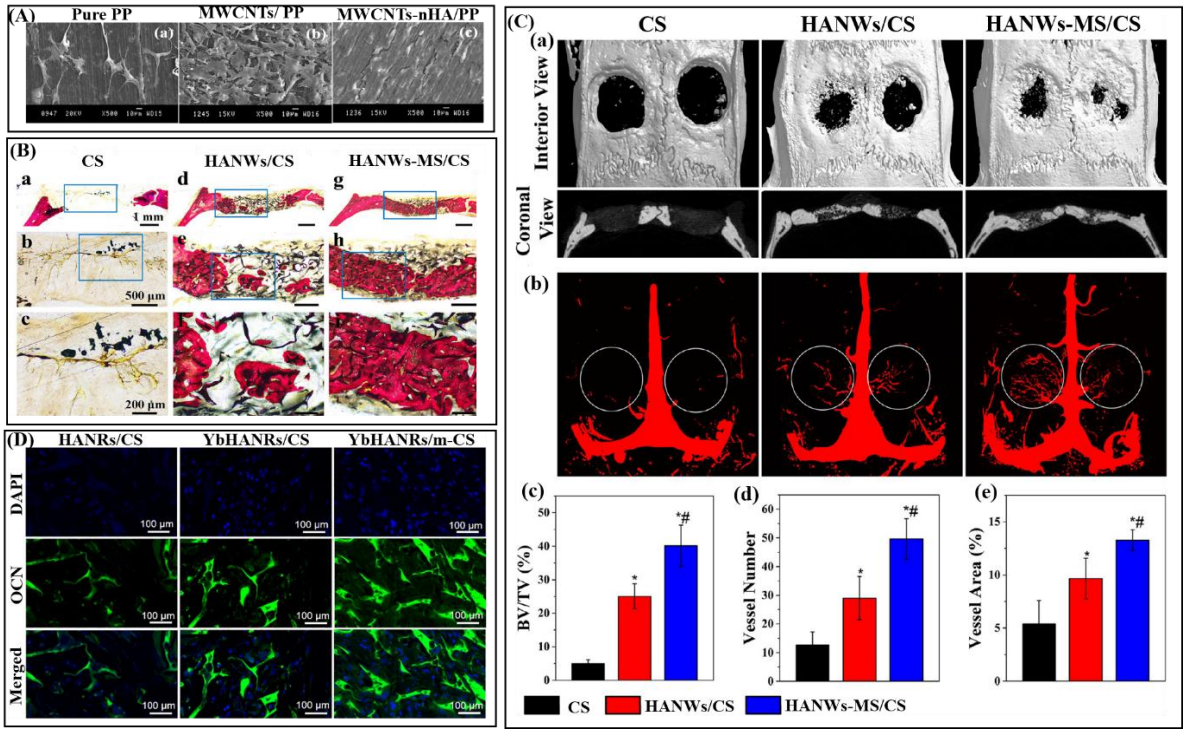

Figure 1.17. In vitro and in vivo cellular response of HA nanocrystals-based scaffolds. *(A) Scanning electron microscopy (SEM) images of osteoblast cells, cultured on (a) polypropylene (PP), (b) 0.3% MWCNTs/PP, and (c) 0.3% MWCNTs- 20 % nHA/PP, for 3 days. Reproduced with the permission from publisher, Ref. [251]. (B) New bone tissue formation around the defect area in rat calvarial after implantation of chitosan scaffolds (CS), HA nanowires/chitosan (HANWs/CS), and HA nanowires-MS/chitosan (HANWs-MS/CS) for 12 weeks. Reproduced with the permission from publisher, Ref. [142]. (C) The micro-CT images, representing the formation of new bone and blood vessels around the defect regions in rat calvarial after implantation of CS, HANWs/CS, and HANWs-MS/CS scaffolds for 12 weeks: the interior and coronal images of calvarial defect repair by the formation of new bone (a), the formation of new blood vessels (b), and newly formed bone (BV/TV) (c) as well as blood vessels (number and area) (d and e) in calvarial defect. Reproduced with the permission from*

publisher, Ref. [142]. (D) The immunofluorescence images of DAPI and OCN proteins on HA nanorods/chitosan (HANRs/CS), Yb-doped HA nanorods/chitosan (YbHANRs/CS) and Yb-doped HA nanorods/magnetic chitosan (YbHANRs/m-CS) scaffolds. Reproduced with the permission from publisher, Ref. [247].

Recently, magnetic (m) chitosan, magnetic $SrFe_{12}O_{19}$ nanoplates coated chitosan, has been successfully used instead of chitosan to upgrade the osteogenesis and angiogenesis performance of Yb-doped HA nanorods/chitosan composite scaffold, because magnetic materials have ability to significantly accelerate the cellular response by activating Wnt/β-catenin, BMP, NF-κB, and MAPK pathways in absence of external magnetic field. Fig. 1.17 D (immunofluorescence OCN image) suggests that Yb-doped HA nanorods/m-chitosan produces the highest amount of OCN protein in comparison to HA nanorods/chitosan and Yb-doped HA nanorods/chitosan composites, which confirm that the use of m-chitosan instead of chitosan significantly promote the osteogenic performance of HA nanorods [247].

Table 1.2 comprehensively presents the bio-mechanical response of scaffolds, based on HA nanocrystals of various 1- and 2-D forms, such as nanorods, nanoplates and nanowires etc.

Overall, it can be concluded that the morphology, amount/chemistry of dopant, aspect ratio, and the content HA nanocrystals are the critical parameters which decide mechanical and biological response of such scaffolds.

Table 1.2. HA nanocrystals-based scaffolds for bone tissue engineering applications.

S.N.	HA nanocrystals with various morphologies	Response	Ref.
1	HA nanorods (Mean length: 120 nm, mean width: 28 nm, pore size: 12 nm, and Pore volume: 16 cm^3/g	• Rapid formation of bone like HA layer on their surfaces after the 7 days of soaking in SBF (excellent *in vitro* bioactivity).	[64]
2	Si/Sr substituted HA nanowires (Length: 2 µm and diameter: 60 nm)	• *In vitro* degradation rate increases from (0.58 – 1.0) % with increasing the amount of Si (0.56 to 3.06 wt %) and Sr (0 to 6.76 wt %) substitution.	[25]
3	Short HA nanowires (Length: 5 µm)	• Good cytocompatibility • Efficient osteogenic differentiation of human derived stem cells without any growth factor, after 21 days of culture.	[17]
	Long HA nanowires (Length: 50 µm)	• Inhibit the spreading of human adipose derived stem cells.	
	HA nanoplates	• Better cytocompatibility than short HA nanowires. • No efficient osteogenic differentiations.	
	HA nanorods (Length: 100 nm)	• Good cytocompatibility (Similar to short HA nanowires). • No efficient osteogenic differentiation.	
4	HA nanorods (Mean length: 125 nm and mean diameter: 39 nm)	• Formation of bone-like mineral after 7 days of incubation with SBF.	[75]
5	HA nanorods (Aspect ratio: 2.0 – 4.4)	• Excellent biocompatibility and highest osteogenic capacity for HA nanorods of aspect ratio of about 2.9.	[18]
6	Rod shaped HA NPs (Mean length: 161 nm	• Apatite formation only after 3 days of incubation in SBF i.e., excellent biomineralization capacity.	[240]

	and mean diameter: 52 nm)	• Higher ability to protein adsorption (1213 ± 178 µg protein the 24 h of incubation in FBS). • Favours cell adhesion, proliferation and spreading.	
7	Graphene nanosheets/ HA nanorods (40 wt %) composites	• Two times higher hardness of 242.06 MPa and Young's modulus of 6.20 GPa than HA nanorods. • Better biocompatibity, osteointegration ability, and cellular proliferation than HA nanorods.	[257]
8	Glucosamine-grafted (g)-HA nanoplates (20 wt %)/sodium alginate (SA) nanocomposite [87.6 % of porosity with average pore size of about 184 µm (suitable for bone tissue engineering)]	• 2 times higher compressive strength (0.198 ± 0.030 MPa) and compressive modulus (2.536 ± 0.315 MPa) than SA scaffold. • Enhanced osteoblastic proliferation of MG-63 cells than pure SA scaffold. • The cell viability has obtained to be proportional to g-HA nanoplates content (10 to 30 wt %) in nanocomposite scaffold.	[209]
9	Magnetic silicium HA nanorods (Fe and Si-doped HA nanorods)	• Improved cellular proliferation and differentiation *in vitro* than HA nanorods. • Better ability to new bone formation *in vivo* than HA nanorods.	[239]
10	HA nanoplates (Length: 95 nm and diameter: 19 nm) coated Nylon (N6) nanofiber biocomposite scaffold	• 235 % increased Young's modulus and 86.6 % higher tensile strength as compared to neat N6 fibers. • Enhanced cellular proliferation and differentiation in comparison to pristine N6 nanofibers.	[14]
11	HA nanorods (10 – 20 wt %)/poly (d, l) lactic acid (PLA) composite scaffold [(Porosity: (84.46 ± 2.17 – 80.18 ± 0.78) % and pore size: (183 ± 60 – 117 ± 60) µm]	• Enhanced *in vitro* biomeralization on composite scaffold (30 wt % of HA nanorods) as compared to PLA scaffold. • Better cell viability and growth on composite scaffold (10 wt % of HA nanorods) in comparison to PLA scaffold.	[252]

12	HA nano rods/PLA biocomposite nanofibers	• 18 % higher degradation rate (1.9 %) after 5 days of incubation in PBS than PLA nanofibers. • Excellent ability to form HA nanosheets based layer on their surfaces after 7 days of incubation with SBF. • Enhanced adhesion, proliferation and spreading of MG63 osteoblast cells on their surfaces than PLA nanofibers. • Superior ability of formation of new collagen and bone tissue at defect region after the 12 weeks of implantation than PLA nanofibers, i.e., Higher *in vivo* biocompatibility.	[253]
13	HA nanorods (20 wt %) reinforced polycaprolactone (PCL) biocomposite (*In-situ*) porous scaffold (Porosity: >90 %)	• ~ 15 % higher Young's modulus (1.99 ± 0.076 MPa) and compressive strength (159 ± 7 kPa) as compared to *ex-situ* nanocomposite scaffold. • Higher *in vitro* bioactivity, cell viability and proliferation against human osteosarcoma cells than *ex-situ* nanocomposite scaffold.	[249]
14	HA nanorods/PCL scaffold	• 98.38 % and 127.60 % enhancement in tensile (8.59 MPa) and compressive strength (14.68 MPa) of 10 wt % HA nanorods/PCL than PCL scaffold. • 10 wt % HA nanorods/PCL scaffold significant promote the cell adhesion, proliferation and growth.	[250]
15	HA nanorods (11.6 wt %)/collagen biocomposite nanofibers [Size of HA nanorods (96 × 32) nm]	• 8 % increased Young's modulus (2.45 GPa), 65.7 % higher tensile strength (228.9 MPa), 389.2 % increased strain to failure (127.2 %), and 665.2 % higher fracture toughness (231.1 $MJ/m^{3)}$ than pure collagen fiber.	[246]
16	HA nanorods (30 wt %)/collagen biocomposite nanofibers	• 182.4 % increased tensile strength (209 ±.16 MPa) with 60 % increased elongation (58 ± 0.18) % in comparison to pure collagen fiber.	[28]

		• Higher cellular viability after 5 days of culture than pure collagen fiber. • Better proliferation and differentiation of U2-OS cells than pure collagen fiber.	
17	Ultralong HA nanowires (70 wt %)/ collagen (UHANWs/Col) and HA nanorods (70 wt %)/collagen (HANRs/Col) biocomposite scaffold	• 63 times higher Young's modulus for UHANWs/Col (61.9 ± 7.2 kPa) than HANRs/Col. • 4 times higher Young's modulus for UHANWs/Col scaffolds and 15 times lower for HANRs/Col scaffold (0.99 ± 0.02 kPa) than pristine collagen (15.0 ± 2.3 kPa) scaffolds. • Better cell adhesion and spreading on the surface of UHANWs/Col scaffold for mesenchymal stem cells than HANRs/Col and collagen scaffold.	[141]
18	Ultralong HA nanowires (66.7 wt %)/collagen composites scaffold [Porosity: 96.61 ± 0.22 % (mimic the porosity of human cancellous bone)]	• 7 times higher compressive modulus (839.4 ± 66.9 kPa) in dry state than collagen scaffold. • Releases 53.9 % of Ca and 36.1 % of P elements with sustained rate after soaking into silane solution for 21 days i.e., good degradation property. • Better stem cell response than collagen scaffold. • Enhanced *in vivo* bone regeneration and integration as compared to collagen scaffold.	[241]
19	Ultralong HA micro or nanoribbons (35 wt %) reinforced collagen biocomposite scaffold (Porosity: 96.09 %)	• 6 times higher Young's modulus (30 ± 1.23 kPa) than pure collagen scaffold. • 8 times slower degradation rate with weight loss of 12.72 ± 2.98% than pure collagen scaffold.	[245]
20	γ-Fe_2O_3 NPs coated nano HA/PVA (m-nHA/PVA) composites scaffold [Pore diameter: 1.6 ± 0.3 µm (For 10 wt % of m-	• 3 times higher compressive strength (29.6± 6.5 MPa) for 10 wt % of m-nHA content in composite scaffold in comparison to PVA scaffold. • Increased adhesion and proliferation of osteoblast cells on composite scaffold with increase in m-nHA content from (10 – 50) wt %.	[248]

	nHA) and 7.8 ± 0.3 µm (For 50 wt % m-nHA)]		
21	Multiwalled carbon nanotubes-HA nanorods (MWCNTs-nHA) reinforced polypropylene (PP) composite scaffold	• ~ 67 % enhancement in the Young's modulus of 20 wt % nHA/PP (~ 2.3 GPa) with respect to PP. • ~ 6.8 % higher tensile strength for 8 wt % nHA/PP (~31 MPa) than PP. • 0.3 wt % addition of MWCNTs in 8 wt % nHA/PP and 20 wt % nHA/PP enhances the tensile strength up to 33 MPa and Young's modulus up to 2.38 GPa, respectively. • Increased viability and proliferation of Saos-2 cells on MWCNT (0.3 wt %)-nHA (20 wt %)/PP than nHA (20 wt %)/PP scaffold.	[251]
22	HA nanowires-Magnesium silicate (MS)/chitosan (CS) porous scaffold (HA NWs-MS/CS)	• More ability to form apatite sheet on their surfaces after soaking into SBF for 4 days than CS scaffold. • Increased proliferation of mesenchymal stem cells than pure CS and HANWs/CS scaffolds. • Higher osteogenic and angiogenic activity *in vitro* than pure CS and HANWs/CS scaffolds. • Favoured the formation of newly bone as well as blood vessel *in vivo* than pure CS and HANWs/CS scaffolds.	[142]
23	Yb-doped HA nanorods/magnetic CS nanocomposite scaffold (Yb-HA/m-CS)	• The coating of CS with magnetic $SrFe_{12}O_{19}$ nanoplates and incorporation of Yb dopants stimulate the osteogenic and angiogenic activity of Yb-HA/m-CS scaffold *in vitro* and *in vi*vo.	[247]
24	HA nanofibers/PLA and PLA-grafted-HA nanofibers/PLA composite scaffolds	• 5 %, 4.9 %, 6.2 % 4.4 % enhancement in Young's modulus, flexural modulus, tensile strength, flexural strength of 5 wt % HA nanofibers/PLA with increasing the aspect ratio of HA nanofibers from 70 to 100. • 8.1 % and 18.5 % higher tensile (86 MPa) and flexural (124 MPa) strengths for PLA-grafted-HA	[244]

		nanofibers/PLA than HA nanofibers/PLA at 10 wt % of HA nanofibers. • More apatite formation on the surface of PLA-grafted-HA nanofibers/PLA composite after soaking into SBF for 5 days.	
25	UHANWs elastic aerogel (porosity: 98.5 % and density: 0.017 g cm^{-3})	• Unlike HA nanorods, superior ability to recover its original shape after 60 % strain at compressive stress of ~ 27 kPa and efficient degradability. • Better cell adhesion and osteogenic differentiation. • Higher rate of new bone as well as blood vessels formation in defect area than HA nanorods after 3 months of implantation, promoting osteogenesis and angiogenesis.	[242]

1.5.1.1. Controlling parameters for mechanical properties, biodegradation and biological response of HA nanocrystals-based scaffolds

1.5.1.1.1. Effect of content of HA nanocrystals

The bio-mechanical response of HA nanocrystals-based scaffolds depends on the contents of HA nanocrystals. For instance, Hay et al.[14] observed that the values of tensile strength and Young's modulus of HA nanoplates coated nylon 6 fiber scaffold increases by about 235 % and 86.6 %, respectively, with respect to nylon 6 fiber. There are two reasons for such improvement in mechanical properties of nanocomposite. (1) Formation of strong hydrogen bonding between HA and nylon 6 fiber which causes good load transfer from matrix to fiber. (2) Generation of micro-mechanical interlocking between HA nanoplates and surface of nylon fiber. Also, the significant increase in cell proliferation and differentiation were observed on composite scaffold in comparison to nylon fiber.

Similarly, Luo et al.[209] also demonstrated that increase of glucosamine-grafted HA nanoplates (gHA nanoplates) from 10 to 20 wt % in gHA nanoplates/sodium alginate scaffold

significantly improve the compressive strength in the range of (0.123 ± 0.015 – 0.198 ± 0.032) MPa, Young's modulus from (1.420 ± 0.005 – 2.536 ± 0.315) MPa, as well as proliferation of MG-63 osteoblast cells. Such enhancement in compressive strength and modulus attributed to the hydrogen bonding between HA and sodium alginate.

Sun et al.[141] also elucidated that Young's modulus of ultralong HA nanowires/collagen scaffold increases from (15.0 ± 2.3 – 61.9 ±7.2) kPa with increasing the HA nanowires content from (0 – 70) wt %. In contrast, Young's modulus of HA nanorods/collagen scaffold decreases from (15.0 ± 2.3 – 0.99 ± 0.02 kPa) with increasing the HA nanorods content from (0 – 70) wt % (Fig. 1.18 A) [141]. The detailed mechanism is discussed in next section.

In addition, it has been reported that increase in ultralong HA micro/nano ribbons content (0 – 35) wt % in HA micro/nano ribbons/collagen scaffold increases Young's modulus from (5 ± 0.8 – 30 ± 1.23) kPa, and slower the degradation rate (Fig. 1.18 B) [245]. However, for 50 wt % HA/collagen scaffold, Young's modulus further reduces to initial value, 5 kPa, which might be due to aggregation of HA within collagen matrix. Moreover, such scaffold also has an excellent ability to recover their shape after 60 % of strain (Fig. 1.18 C).

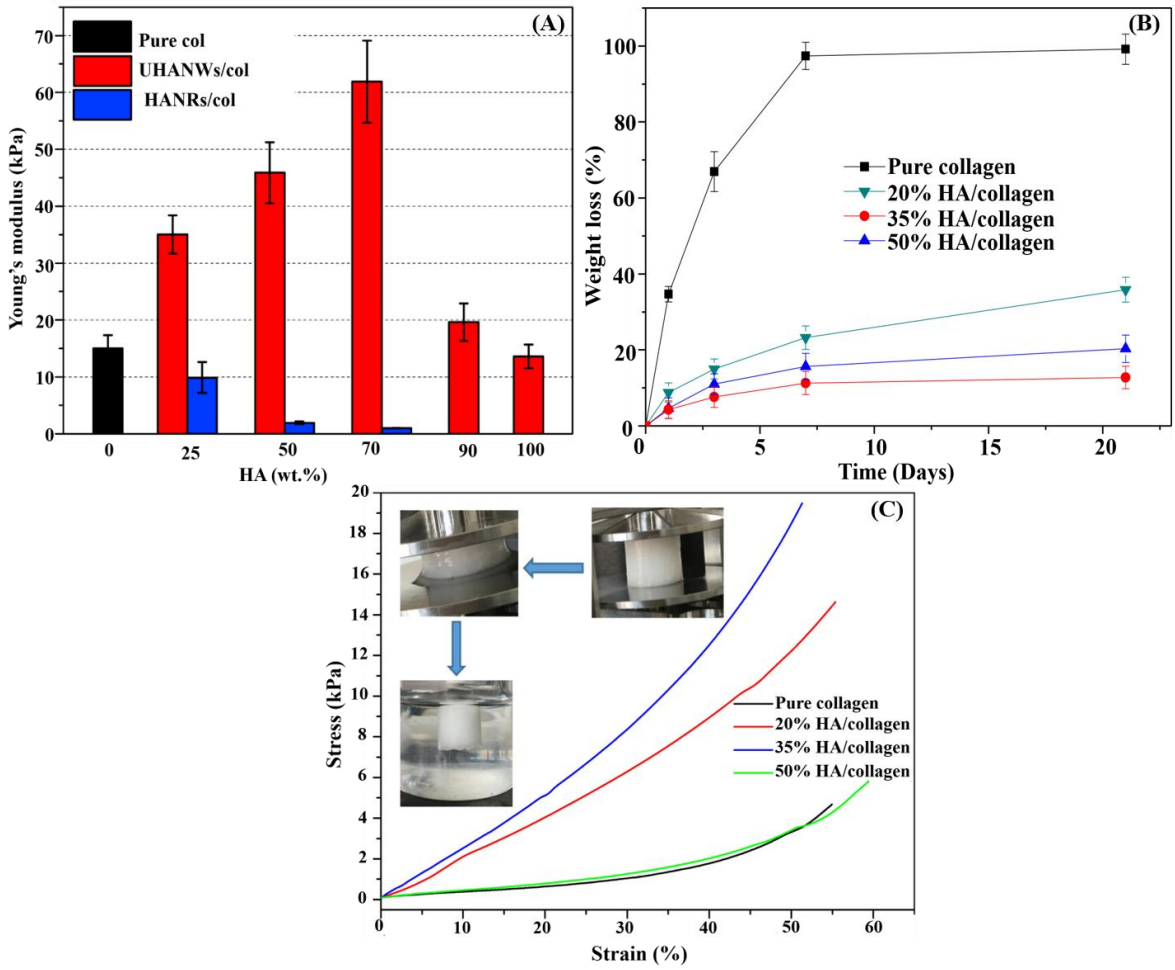

Figure 1.18. Mechanical and in vitro degradation response of HA nanocrystals-based scaffolds. *(A) Young's modulus for pure collagen (Col), ultralong HA nanowires (UHANWs)/Col and HA nanorods (HANRs)/Col with varying content of HA nanocrystals. Reproduced with the permission from publisher, Ref. [141]. (B) Weight loss in pure collagen and HA micro/nanoribbons/collagen (HA/collagen) scaffolds after incubation in SBF Reproduced with the permission from publisher, Ref. [245]. (C) Stress-strain curve and digital images (inset), demonstrating the ability of HA/collagen to recover its shape. Reproduced with the permission from publisher, Ref. [245].*

In 2012, Ko et al.[244] also observed that 5 wt % HA nanofibers (aspect ratio:100) reinforced PLA composite possess 13 % higher tensile strength (82 MPa) as compared to PLA due to bridging of HA nanofibers, which delayed the failure. Moreover, Young's modulus and flexural modulus of HA nanofibers (aspect ratio ~100) reinforced PLA composite also increases

from 4 to 5 GPa and 4.8 to 7 GPa, respectively, with increasing the HA nanofibers content from 5 to 15 wt %. Lately, Pei Feng et al.[250] also reported that the tensile strength, compressive strength, tensile modulus and compressive modulus of PCL scaffold enhances from 4.33 – 8.59 MPa, 6.0 – 14.68 MPa, 136.03 – 348.35 MPa, 40.0 – 154.76 MPa on reinforcing with 10 wt % of HA nanorods. Such amount of HA nanorods in HA nanorods/PCL scaffold better promote the stress transfer within PCL matrix. However, on further increasing the content of HA nanorods to 15 wt % reduces all the mechanical properties due to poor dispersion of HA nanorods within PCL matrix. This mechanical feature of HA nanorods/PCL scaffold is in between to cortical and cancellous bone. Moreover, cell adhesion, spreading and proliferation is highest on HA nanorods (10 wt %)/PCL scaffold which is attributed to increase in wettability of scaffold as well as ability to form bone-like apatite layer.

It can, therefore, be affirmed that the optimal content of HA nanocrystals can be helpful in achieving the desirable properties for bone regeneration.

1.5.1.1.2. Influence of culture duration

Number of researchers varied the culture duration to achieve the optimal *in vitro* biological response. As example, Liao et al.[251] optimized that the cellular proliferation on MWCNTs-nHA/PP scaffold increases with increasing the culture time, and eventually reaches to maximum after the 10 days of incubation. Other research groups, e.g., Fan et al.[257] and Zhang et al.[253] obtained the maximum cell density on HA nanorods/graphene and HA nanorods/PLA scaffold after 4 and 7 days of incubation, respectively. In addition, Zhou et al.[28] demonstrated that the viability and differentiation of cells increases on increasing the incubation period of HA nanorods/collagen composite nanofiber scaffold from 1 to 5 days. Hay et al.[14] and Luo et al.[209] also observed the identical variation of cell growth on HA nanoplates/N6 fibers and gHA nanoplates/sodium alginate composite scaffold with culture time of (1 – 5) days. Furthermore, Ma et al.[17] and Li et al.[239] found that osteogenic genes

expressions, such as Runx2, osterix, alkaline phosphatase (ALP), OPN, OCN and col-I which is the direct measure of osteogenic differentiation of cells, increases on increasing the culture duration of different morphological HA nanocrystals as well as Si and Fe co-doped HA nanorods from 1 – 21 and 1 – 14 days, respectively. Importantly, the bioactivity of scaffold also increased with time (1 – 7 days) when soaked in SBF. It has been observed that 7 days is the appropriate soaking time to attain the excellent bioactivity, as the clear HA nanoplates formation appears on scaffold surface after 7 days of soaking (Fig. 1.19 A) [64, 75, 257].

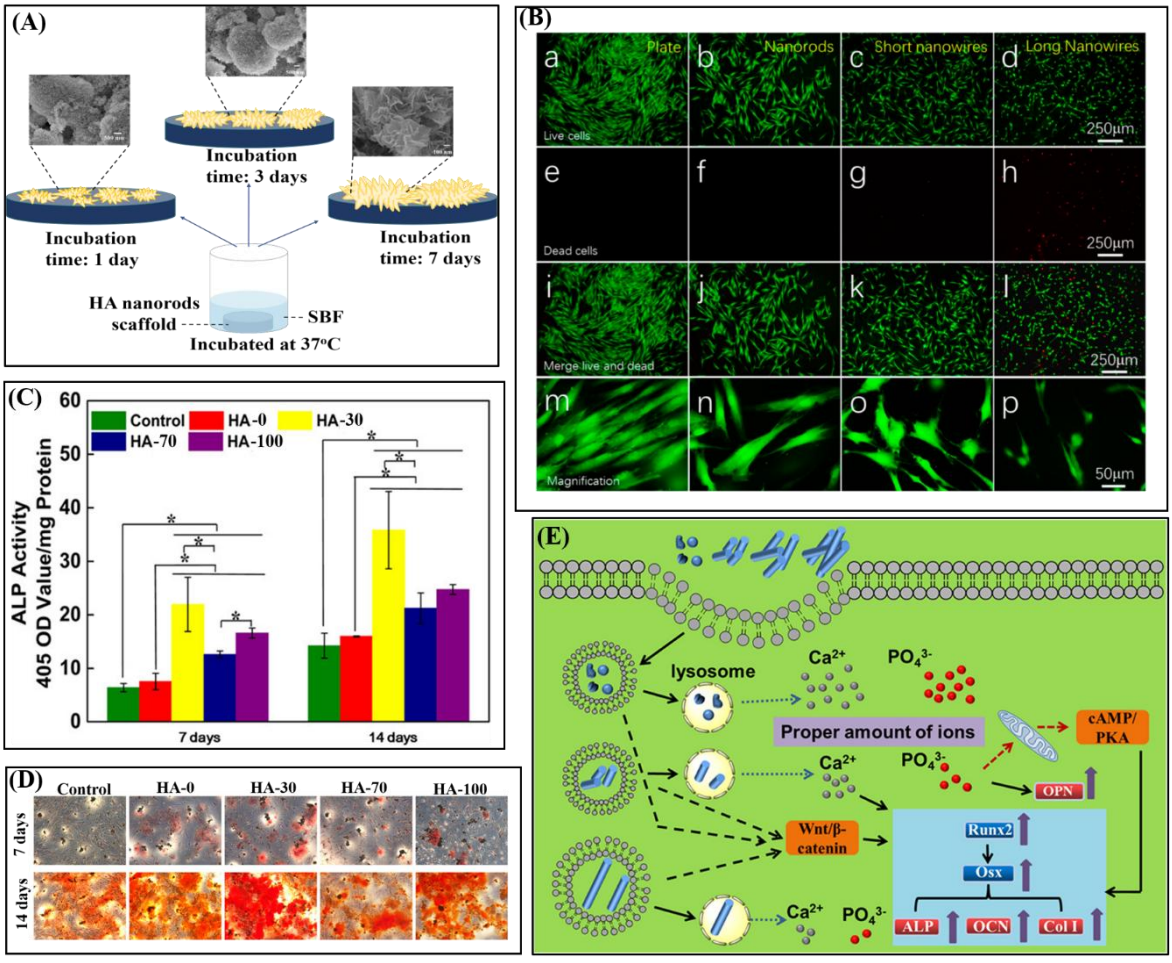

Figure 1.19. In vitro cellular and antibacterial response of various morphologies of HA nanocrystals-based scaffolds. *(A) Formation of HA nanoplates by soaking HA nanorods in SBF for a period of up to 7 days. The SEM images are reproduced with the permission from publisher, Ref [64]. (B) The stem cell response on scaffolds of HA nanoplates (a, e, i and m), HA nanorods (b, f, j and n), HA short nanowires (c, g, k and o) and HA long nanowires (d, h,*

l and p). Reproduced with the permission from publisher, Ref. [17]. (C) ALP activity of mesenchymal stem cells, cultured with various HA nanocrystals including irregular NPs of aspect ratio of 2.4 (HA-0) and HA nanorods of aspect ratios of 2.9, 3.37 and 4.32 (HA-30, HA-70 and HA-100). Reproduced with the permission from publisher, Ref. [18]. (D) Alizarin staining of MSCs, cultured with HA-0, HA-30, HA-70 and HA-100. Reproduced with the permission from publisher, Ref. [18]. (E) Schematic representing the mechanism towards contribution of HA nanorods of different aspect ratios to osteogenic differentiation of MSCs. Reproduced with the permission from publisher, Ref. [18].

1.5.1.1.3. Effect of morphology of HA nanocrystals

Sun et al.[141] demonstrated that ultralong HA nanowire (70 wt. %) /collagen scaffolds possess 63 times higher Young's modulus, larger porosity, better biocompatibility as compared to HA nanorod (70 wt. %)/collagen scaffolds. Such a vast difference in Young's modulus in both the scaffolds can be explained by the fact that unlike HA nanorods, high flexibility and aspect ratio allows the ultralong HA nanowires to intertwine with each other while designing their composite with collagen, which facilitate the strong interaction with collagen matrix. This interaction becomes stronger with increasing the HA nanowires content up to 70 wt %. Ma et al.[17] compared the biological response of HA nanocrystals with various morphological features, such as HA nanoplates, long HA nanowires, short HA nanowires and HA nanorods. It has been suggested that short nanowires demonstrate better cytocompatibility as well as good osteogenic differentiation of stem cells. In contrast, long HA nanowires rather inhibit the migration and spreading of stem cells, indicating lower cytocompatibility. On the other hand, in spite of excellent cytocompatibility of both, HA nanorods and HA nanoplates, unfavorable osteogenic differentiation of stem cells is observed. Fig. 1.19 B clearly shows that viability of stem cells is maximum when cultured on HA nanoplates and least over the surface of long HA

nanowires scaffold. Interestingly, this result also demonstrates the effect of aspect ratio of HA nanowires on biological response.

1.5.1.1.4. Effect of doping

The doping in HA nanocrystals with Si, Sr, Fe, and Yb elements also confers the control over cellular response and biodegradation rate [25, 239, 247]. Zhang et al.[25] improved *in vitro* degradation of HA nanowires by reducing their crystallinity with the co- substitution of Si (0.56 to 3.06 wt %) and Sr (0 to 6.76 wt %) ions. Li et al.[239] reported that the substitution of HA nanorods with Si and Fe aid to enhance the cell proliferation, differentiation, *in vitro* as well as bone integration ability, *in vivo*, which is due to sustained release of Si and Fe ions. Tang et al.[247] demonstrated that Yb doping in HA nanorods/magnetic collagen scaffold exceptionally upregulates the osteogenic activity, bone growth and blood vessels formation with the activation of Wnt, ERK and Smad pathways.

1.5.1.1.5. Effect of aspect ratio of HA nanocrystals

According to recent reports, biological properties of HA nanocrystals have also been customized by variation in their aspect ratio and surface topography [18, 258]. Li et al.[18] synthesized irregular HA NPs of aspect ratio typically 2.14 at room temperature and HA nanorods with varied aspect ratio of about 2.9, 3.37 and 4.32 at temperatures of 30ºC, 70ºC and 100ºC, respectively. It has been observed that smaller HA nanorods, due to their less crystalline structure, facilitate stem cell proliferation better than larger HA nanorods. Moreover, HA nanorods of moderate aspect ratio (2.9) exhibit the highest intracellular ALP activity (Indication of early-stage osteogenic differentiation) [Fig. 1.19 C], the highest MSC biomineralization (Indication of later stage osteogenic differentiation) [Fig. 1.19 D] and the highest expression level for all osteogenesis related genes, including Osx, ALP, Col I, OCN and OPN. In addition, possible mechanism behind the highest osteogenic activity of HA nanorods of aspect ratio of 2.9 are also elucidated in Fig. 1.19 E [18]. In comparison to irregular

HA NPs, HA nanorods can better promote the expression level of genes including, OCN, Col I and ALP via WNT/β-catenin pathway. Meanwhile, Ca^{2+} ions also regulate the OCN, Col I and ALP expressions with the promotion of Runx2 and Osx expressions. In addition, phosphate ions also increase the expression level of OCN genes to speed up the osteogenesis process via cAMP/PKA pathway. Moreover, smaller HA nanorods can enter relatively easily within the cells via the endocytic pathway than larger ones, and HA nanorods can be partially dissolved into lysosomal atmosphere. Therefore, dissolution of smaller sized and less crystalline HA nanorods can increase the Ca and P ions concentrations within the stem cell, resulting in enhanced osteogenesis related gene expression level. That's why, HA nanorods of moderate aspect ratio (2.9) displayed the highest osteogenic activity [18]. Recently, Ko et al.[244] also showed that tensile strength of 5 wt % HA nanofibers reinforced PLA composite increases from 77 to 81 MPa with increasing the aspect ratio of HA nanofibers from 70 to 100. HA nanofibers filler of higher aspect ratio offers better stress transfer from PLA matrix to nanofiber in PLA nanocomposite.

1.5.2. Antibacterial response of HA nanocrystals and its composites

Besides the mechanical, biological, and controlled biodegradation properties for a successful scaffold, antibacterial features that prevent the implant from bacterial infection have also been recently recognized among important requirements for prosthetic applications [259]. Bacterial infections are a serious global issue, accounting for most orthopedic implant failures. Despite the host immune defense system, bacteria readily adhere on the orthopedic implant surfaces, leading to colonization, and the formation of three-dimensional biofilms. These biofilms protect bacteria from immune cells, disinfectants and antibiotics [260]. The main bacteria related to implant infection are *Staphylococcus aureus (S. aureus)* and *Staphylococcus epidermidis as* gram-positive bacteria, and *Escherichia coli (E. coli)* as gram-negative bacteria [261-263]. Pure bulk HA supports the bacterial growth [94, 264]. Nanotechnology has emerged

as a promising approach to control bacterial growth in the past few years. The nano-sized particles with a high surface area to volume ratio exhibit enhanced reactivity towards bacterial cells, enabling them to show bactericidal effects. The most common underlying mechanisms for the antibacterial potential of NPs include: a) damage to the bacterial cell membrane, b) overproduction of ROS as an oxidative stress marker, and c) disruption in metabolism [265, 266]. Nano-sized particles can easily penetrate the bacterial cell and disturb the cellular metabolism, which causes cell death. Moreover, NPs are also susceptible to higher production of ROS due to the large number of reactive sites on their surface, which possess the significant capability to reduce the intracellular molecular oxygen, resulting in ROS including, superoxide anions ($O_2^{-\bullet}$), H_2O_2 and •OH etc. [265] Few studies highlighted the antibacterial potential of HA nanocrystals. For example, Kumar et al.[267] demonstrated that *E. coli* and *S. aureus* bacteria, treated with HA nanorods, exhibit an inhibition zone with a diameter of 26 mm. Baskar et al.[266] also observed the efficient antibacterial response of HA NPs against four bacteria, i.e., *E. coli*, *P. aeruginosa*, *K. pneumonia* and *Salmonella typhi*. Gopi et al.[63] showed that HA nanorods, fabricated using tartaric acid as a template, display the inhibition zone of lower diameter (~1 mm) against gram-negative bacteria (e.g., *E. coli* and *Klebsiella*) than HA nanorods, derived from natural sources, such as banana, grapes, and tamarind. The diameters of the inhibition zone, against *E. coli* and *Klebsiella* bacteria, are reported to be about 14 mm, 12 mm for tamarind-derived HA nanorods, 13 mm and 11 mm for grape-derived HA nanorods, and 11 mm and 9 mm for banana-derived HA nanorods, respectively. Such enhancement in antibacterial activity of HA nanorods, derived from natural sources, has been suggested to be attributed to the presence of few mineral ions, such as Na^{2+}, Mg^{2+} and Zn^{2+}. Abed et al.[268] observed significantly lower bacterial growth on nHA (1.6 wt %)/polycarbonate composite film than pure polycarbonate film. The diameters of the inhibition zone for *E. coli and S. aureus* pathogens were 27 mm and 18 mm, respectively, which is

significantly higher than polycarbonate film. The doping with elemental ions, such as Ag^{+}, Zn^{2+}, Mn^{2+} and Co^{2+} makes HA nanorods as impressive antibacterial material, where the antibacterial response is the function of doping content [94, 96, 134, 269]. The lysis of cell membrane, either due to interaction of HA nanorods with their surface molecules via electrochemical interaction or binding of metal ion with peptidoglycan layer of cell membrane, inactivation of cellular enzymes to inhibit cell division, oxidative stress, and inactivation of protein are the suggested mechanisms for the antibacterial activity of metal doped HA nanorods. Te-doped (0.24 wt %) HA nanorods and moringa oleifera extract-capped HA nanorods show better antibacterial response than pure HA nanorods [90, 92]. Recently, the doping of HA nanorods with Zn^{2+} ions have significantly induced the antibacterial response. On increasing the Zn content from 1.1 to 5.5 of Zn/(Ca + Zn) %, the zone of inhibition also increases from 09.14 ± 0.12 to 13.12 ± 0.16 for Bacillus subtilis bacteria and from 07.10 ± 0.13 to 12.36 ± 0.12 for *Klebsiella pneumoniae* bacteria. This is due to the release of Zn^{2+} ions, doped in HA nanorods, which bring the bactericidal effect around the bone implant [269]. Despite extensive research, the potentiality of HA nanocrystals-based scaffolds is still being explored for bone tissue engineering applications.

1.5.3. Drug delivery

Osteomyelitis is a severe infection of the bone that typically arises from injury, fractures, or surgery, and a major cause of implant failure. The primary causative pathogen of osteomyelitis is Gram-positive bacteria; *S. aureus*, accounting for up to 90 % of the cases [270, 271]. Even though various antibiotics are available, treating the bacterial infection is a worldwide issue due to the difficulty in achieving an optimal antibiotic concentration at the infection site [272, 273]. Traditional drug delivery methods do not offer controlled drug release, resulting in low bioavailability of the drug at infection site as well as spreading of drug in undesired areas that causes various side effects [274]. Additionally, the effectiveness of antibiotics depends on the

dosage and treatment time as bacteria continuously develop an intrinsic resistance by reducing membrane permeability, breaking down the antibiotic, or altering its target [275-277]. Therefore, in a past decade, sustained drug delivery has been developed as an advanced strategy to enhance the therapeutic efficacy of antibiotics [278]. It enables the prolonged drug release that increases the bioavailability of drug at infection site while minimizing drug spreading at unintended area [274]. For effective performance, a drug vehicle should hold various features, including excellent biocompatibility, high drug loading efficiency, and a controlled drug release response [279]. HA nanocrystals have recently emerged as an ideal drug delivery vehicle due to their outstanding biocompatibility and extensive drug binding sites on their surface. Number of previous studies showed the potentiality of HA nanocrystals as a sustained drug delivery system for bacterial eradication [280, 281]. For instance, Li et al.[264] reported antibacterial response in covalently bonded antimicrobial peptide "HHC-36" (which is grafted with polymer brush) on Fe and Si co-doped HA nanorods. In this study, polymer brush grafted HHC-36 peptide on HA nanorods was found to kill 99.9 % of *E. coli* and 99.5 % of *S. aureus* bacteria. The combined action of covalent bonding of antimicrobial peptide related destruction as well as physical damage by HA nanorods is suggested to be responsible for such antibacterial response. Asghar et al.[282] loaded the ciprofloxacin (96 % efficiency) onto nickel-doped HA NPs with 95 % controlled drug release. Such drug loaded HA controlled the bacterial growth with inhibition zone of 22 mm for *E. coli* and 24 mm for *P. aeruginosa* strains. Geuli et al.[270] also investigated the antibacterial activity of ciprofloxacin-loaded HA NPs coated on titanium implants. It found the prolonged drug release up to 25 days, which significantly inhibited the growth of *Pseudomonas aeruginosa* bacterial strain. Souza et al.[283] also inhibited the growth of *Enterococcus faecalis* bacteria due to sustained release of doxycycline from HA microspheres up to 7 days. Xiong et al.[158] also demonstrated that silver NPs (2.87 wt %) loaded HA nanowires paper and antibiotic "ciprofloxacin (527.7 mg/g)" loaded HA nanowires

paper exhibit inhibition zones of diameters about 9.2 and 9.7 mm against *E.coli* bacteria and 6.1 and 6.2 mm against *S. aureus* bacteria, respectively.

1.6. Motivation

Hexagonal HA possesses two distinct crystal planes, "a (b)-plane and c-plane". Each type is characterized by unique atomic arrangements with opposite charges. The first plane is predominantly populated with Ca^{2+} ions, providing a positively-charged surface. Whereas, the later plane is abundant in PO_4^{3-} and OH^- ions, giving rise to a negative charge. This charge variation between crystal planes facilitates different morphologies of nHA (c-axis oriented HA nanorods and a (b)-axis oriented 2-D HA nanoplates) to achieve various properties/applications. In particular, bone, 3-D hierarchical structure, is primarily composed of 2-D HA nanoplates with dimensions in range of 4 –10 nm in thickness, 30 – 200 nm in length and width, which is uniaxially and longitudinally impregnated within self-assembled collagen fibrils matrix. Such architectural arrangement endows high strength, good fracture toughness, favorable biological response, and remodelling nature to the bone. Due to such exceptional performance of living bone, there is remarkable interest in the scientific community towards the development of bone-mimicking materials, i.e., 2-D HA nanoplates, to repair large bone defects. Consequently, the synthesis of bone-like 2-D HA nanoplates becomes a key area of interest. Until now, few research articles have been published on the synthesis of HA nanoplates, based on chemical-precipitation, HT method, template-assisted technique [using SDS, PEG and g-C_3N_4 as templates], and ultrasonic precipitation, as already discussed in section 1.4.2.1. Unexpectedly, to the best of our knowledge, no article truly reflects the morphology of bone apatite nanoplates. The precise control over the crystal growth of HA along their a (b)-axis, i.e. [100] direction, for the creation of plate-like morphology is a quite challenging task as compared to their c-axis, i.e. [001] direction, because crystal growth of HA in nanorod shape is thermodynamically favourable due to relatively high surface energy of

their (001) face. Several pivotal studies also proved that the cytocompatibility, osteogenic, and antibacterial response of nanostructured materials is significantly influenced by several factors, including size, shape, concentrations, surface charge, ion release, crystallinity, hydrophilicity, and agglomeration. However, such biological potential of HA nanoplates compared to other shapes of HA nanocrystals is yet to be revealed. Moreover, the specific mechanisms underlying these varied biological effects across different nHA shapes were not properly addressed. Therefore, investigating the cytocompatibility, hemocompatibility, osteogenic, and antibacterial response of HA nanoplates compared to other shapes of nHA, with special emphasis on their surface chemistry and other aforementioned parameters, can significantly provide a broad spectrum for their applications in prosthetic implants. Further, a number of previous studies also showed the potentiality of HA nanocrystals as a sustained drug delivery system for bacterial eradication. However, no detailed study has been performed on antibiotic loading in HA nanoplates and their release behavior for bacterial growth control, compared to HA nanorods. While it is well established that morphology and dimensions of HA nanocrystals play a crucial role in modulating drug loading capacity, release kinetics, and their effect on antibacterial efficacy. In view of the above, exploring the antibacterial potential of antibiotic-loaded HA nanoplates with a detailed study in their drug loading and release behavior as compared to HA nanorods can provide a biocompatible and sustained-release antibiotic drug vehicle for effective bacterial eradication.

1.7. Objectives

The primary objective of the present thesis is to develop the bone-mimicking morphology of HA nanocrystals, such as nanoplates, using biocompatible PVA as a surface capping agent via the HT method. In addition, the cellular and antibacterial response of developed bone-like HA nanoplates are investigated as compared to 1-D HA nanorods. Further, the antibacterial effect of antibiotic-loaded HA nanoplates, in contrast to HA nanorods, is also explored.

The specific objectives of the present thesis are as follows:

(a) To systematically optimize the different experimental conditions, such as pH of precursor solution, HT time, and PVA concentrations to obtain the desired shape of HA nanoplates and to observe the corresponding change in morphology of HA nanocrystals.

(b) To conduct a thorough investigation to uncover the possible molecular mechanism governing the formation of HA nanoplates, nanorods, and thin nanoplates obtained under different experimental conditions, and to verify it from previous studies.

(c) To examine the impact of the morphology of HA nanocrystals on their surface charge, oxygen vacancy, and wettability using zeta potential measurement, XPS, and contact angle measurement, respectively.

(d) To investigate the cytocompatibility, hemocompatibility, osteogenic activity, and antibacterial response of HA nanoplates along with other nHA morphologies, HA nanorods and thin nanoplates.

(e) To explore the antibacterial effect of doxycycline hyclate (DOX)-loaded HA nanoplates with detailed analysis of their drug loading efficiency and release profile, compared to HA nanorods.

References

[1] Y. Sun, Y. Wang, C. Ji, J. Ma, B. He, The impact of hydroxyapatite crystal structures and protein interactions on bone's mechanical properties, Scientific Reports 14(1) (2024) 9786.

[2] W. Wang, K.W.K. Yeung, Bone grafts and biomaterials substitutes for bone defect repair: A review, Bioactive Materials 2(4) (2017) 224-247.

[3] V.H. Ingole, K. Hany Hussein, A.A. Kashale, K. Ghule, T. Vuherer, V. Kokol, J.-Y. Chang, Y.-C. Ling, A. Vinchurkar, H.N. Dhakal, A.V. Ghule, Ultrasound-assisted green economic synthesis of hydroxyapatite nanoparticles using eggshell biowaste and study of mechanical and biological properties for orthopedic applications, Journal of Biomedical Materials Research Part A 105(11) (2017) 2935-2947.

[4] Y. Ma, A. Wang, J. Li, Q. li, Q. Han, Y. Chen, S. Wang, X. Zheng, H. Cao, S. Bai, Preparation of hydroxyapatite with high surface area and dispersity templated on calcium carbonate in dipeptide hydrogels, Colloids and Surfaces A: Physicochemical and Engineering Aspects 596 (2020) 124740.

[5] Y. Cai, Y. Liu, W. Yan, Q. Hu, J. Tao, M. Zhang, Z. Shi, R. Tang, Role of hydroxyapatite nanoparticle size in bone cell proliferation, Journal of Materials Chemistry 17(36) (2007) 3780-3787.

[6] Z. Shi, X. Huang, Y. Cai, R. Tang, D. Yang, Size effect of hydroxyapatite nanoparticles on proliferation and apoptosis of osteoblast-like cells, Acta Biomaterialia 5(1) (2009) 338-345.

[7] M. Sadat-Shojai, M.-T. Khorasani, E. Dinpanah-Khoshdargi, A. Jamshidi, Synthesis methods for nanosized hydroxyapatite with diverse structures, Acta Biomaterialia 9(8) (2013) 7591-7621.

[8] T.G. Peñaflor Galindo, M. Tagaya, Interfacial Effect of Hydration Structures of Hydroxyapatite Nanoparticle Films on Protein Adsorption and Cell Adhesion States, ACS Applied Bio Materials 2(12) (2019) 5559-5567.

[9] S. Cai, C. Wu, W. Yang, W. Liang, H. Yu, L. Liu, Recent advance in surface modification for regulating cell adhesion and behaviors, 9(1) (2020) 971-989.

[10] Y. Liu, A. Nadeem, S. Sebastian, M.A. Olsson, S.N. Wai, E. Styring, J. Engellau, H. Isaksson, M. Tägil, L. Lidgren, D.B. Raina, Bone mineral: A trojan horse for bone cancers. Efficient mitochondria targeted delivery and tumor eradication with nano hydroxyapatite containing doxorubicin, Materials Today Bio 14 (2022) 100227.

[11] Y.-J. Zhu, B.-Q. Lu, Deformable Biomaterials Based on Ultralong Hydroxyapatite Nanowires, ACS Biomaterials Science & Engineering 5(10) (2019) 4951-4961.

[12] D. Lyu, Q. Zhang, Y. Wu, L. Chen, X. Li, H. Ren, Y. Yan, Effects of particle size of hydroxyapatite on mechanical property and cytocompatibility of hydroxyapatite/poly(amino acid) composites, Polymer Composites 43(2) (2022) 1107-1120.

[13] G. Poinern, R. Brundavanam, D. Fawcett, Nanometre scale hydroxyapatite ceramics for bone tissue engineering, American Journal of Biomedical Engineering 3 (2013) 148-168.

[14] A. Abdal-hay, P. Vanegas, A.S. Hamdy, F.B. Engel, J.H. Lim, Preparation and characterization of vertically arrayed hydroxyapatite nanoplates on electrospun nanofibers for bone tissue engineering, Chemical Engineering Journal 254 (2014) 612-622.

[15] H.M. Mousa, A.P. Tiwari, J. Kim, S.P. Adhikari, C.H. Park, C.S. Kim, A novel in situ deposition of hydroxyapatite nanoplates using anodization/hydrothermal process onto magnesium alloy surface towards third generation biomaterials, Materials Letters 164 (2016) 144-147.

[16] C. Burda, X. Chen, R. Narayanan, M.A. El-Sayed, Chemistry and Properties of Nanocrystals of Different Shapes, Chemical Reviews 105(4) (2005) 1025-1102.

[17] B. Ma, S. Zhang, F. Liu, J. Duan, S. Wang, J. Han, Y. Sang, X. Yu, D. Li, W. Tang, S. Ge, H. Liu, One-Dimensional Hydroxyapatite Nanostructures with Tunable Length for

Efficient Stem Cell Differentiation Regulation, ACS Applied Materials & Interfaces 9(39) (2017) 33717-33727.

[18] Y. Li, Y. Wang, Y. Li, W. Luo, J. Jiang, J. Zhao, C. Liu, Controllable Synthesis of Biomimetic Hydroxyapatite Nanorods with High Osteogenic Bioactivity, ACS Biomaterials Science & Engineering 6(1) (2020) 320-328.

[19] A.J. Nathanael, S.I. Hong, T.H. Oh, Y.H. Seo, D. Singh, S.S. Han, Enhanced cell viability of hydroxyapatite nanowires by surfactant mediated synthesis and its growth mechanism, RSC Advances 6(30) (2016) 25070-25081.

[20] Y. Wang, S. Zhang, K. Wei, N. Zhao, J. Chen, X. Wang, Hydrothermal synthesis of hydroxyapatite nanopowders using cationic surfactant as a template, Materials Letters 60(12) (2006) 1484-1487.

[21] D. Gopi, J. Indira, S. Nithiya, L. Kavitha, U.K. Mudali, K. Kanimozhi, Influence of surfactant concentration on nanohydroxyapatite growth, Bulletin of Materials Science 36(5) (2013) 799-805.

[22] G. Zuo, X. Wei, H. Sun, S. Liu, P. Zong, X. Zeng, Y. Shen, Morphology controlled synthesis of nano-hydroxyapatite using polyethylene glycol as a template, Journal of Alloys and Compounds 692 (2017) 693-697.

[23] Y. Xu, L. An, L. Chen, L. Cao, D. Zeng, G. Wang, A Facile chemical route to synthesize Zn doped hydroxyapatite nanorods for protein drug delivery, Materials Chemistry and Physics 214 (2018) 359-363.

[24] Y. Xu, L. An, L. Chen, H. Xu, D. Zeng, G. Wang, Controlled hydrothermal synthesis of strontium-substituted hydroxyapatite nanorods and their application as a drug carrier for proteins, Advanced Powder Technology 29(4) (2018) 1042-1048.

[25] N. Zhang, D. Zhai, L. Chen, Z. Zou, K. Lin, J. Chang, Hydrothermal synthesis and characterization of Si and Sr co-substituted hydroxyapatite nanowires using strontium

containing calcium silicate as precursors, Materials Science and Engineering: C 37 (2014) 286-291.

[26] X.-Y. Zhao, Y.-J. Zhu, F. Chen, B.-Q. Lu, C. Qi, J. Zhao, J. Wu, Hydrothermal synthesis of hydroxyapatite nanorods and nanowires using riboflavin-5′-phosphate monosodium salt as a new phosphorus source and their application in protein adsorption, CrystEngComm 15(39) (2013) 7926-7935.

[27] V.K. Mishra, B.N. Bhattacharjee, O. Parkash, D. Kumar, S.B. Rai, Mg-doped hydroxyapatite nanoplates for biomedical applications: A surfactant assisted microwave synthesis and spectroscopic investigations, Journal of Alloys and Compounds 614 (2014) 283-288.

[28] Y. Zhou, H. Yao, J. Wang, D. Wang, Q. Liu, Z. Li, Greener synthesis of electrospun collagen/hydroxyapatite composite fibers with an excellent microstructure for bone tissue engineering, Int J Nanomedicine 10 (2015) 3203-15.

[29] G. Bharath, A. Jagadeesh Kumar, K. Karthick, D. Mangalaraj, C. Viswanathan, N. Ponpandian, Shape evolution and size controlled synthesis of mesoporous hydroxyapatite nanostructures and their morphology dependent Pb(ii) removal from waste water, RSC Advances 4(70) (2014) 37446-37457.

[30] Q.-Q. Zhang, Y.-J. Zhu, J. Wu, Y.-T. Shao, L.-Y. Dong, A new kind of filter paper comprising ultralong hydroxyapatite nanowires and double metal oxide nanosheets for high-performance dye separation, Journal of Colloid and Interface Science 575 (2020) 78-87.

[31] S. Cao, X. Wu, Y. Zhu, R. Gupta, A. Tan, Z. Wang, Y.-S. Jun, S. Singamaneni, Polydopamine/hydroxyapatite nanowire-based bilayered membrane for photothermal-driven membrane distillation, Journal of Materials Chemistry A 8(10) (2020) 5147-5156.

[32] N. Razavi, B. Akhlaghinia, Hydroxyapatite nanoparticles (HAP NPs): a green and efficient heterogeneous catalyst for three-component one-pot synthesis of 2,3-

dihydroquinazolin-4(1H)-one derivatives in aqueous media, New Journal of Chemistry 40(1) (2016) 447-457.

[33] F. Chen, Y.-J. Zhu, Large-Scale Automated Production of Highly Ordered Ultralong Hydroxyapatite Nanowires and Construction of Various Fire-Resistant Flexible Ordered Architectures, ACS Nano 10(12) (2016) 11483-11495.

[34] X. Chen, X. Jin, J. Tan, W. Li, M. Chen, L. Yao, H. Yang, Large-scale synthesis of water-soluble luminescent hydroxyapatite nanorods for security printing, Journal of Colloid and Interface Science 468 (2016) 300-306.

[35] T. Chatterjee, P. Chatterjee, A.K. Chakraborty, S.K. Pradhan, A.K. Meikap, Template-free growth of copper-doped hydroxyapatite nanowhiskers and their use as uric acid electrochemical sensor, Materials Today Communications 33 (2022) 104870.

[36] Nanomaterials: General Synthetic Approaches, Essentials in Nanoscience and Nanotechnology2016, pp. 29-76.

[37] F. Ren, Y. Ding, X. Ge, X. Lu, K. Wang, Y. Leng, Growth of one-dimensional single-crystalline hydroxyapatite nanorods, Journal of Crystal Growth 349(1) (2012) 75-82.

[38] A. Zhu, Y. Lu, Y. Si, S. Dai, Frabicating hydroxyapatite nanorods using a biomacromolecule template, Applied Surface Science 257(8) (2011) 3174-3179.

[39] Y.H.S. A. Joseph Nathanael, and Tae Hwan Oh, PVP Assisted Synthesis of Hydroxyapatite Nanorods with Tunable Aspect Ratio and Bioactivity, Journal of Nanomaterials (2015) 9.

[40] Z. Wu, S. Yang, W. Wu, Shape control of inorganic nanoparticles from solution, Nanoscale 8(3) (2016) 1237-1259.

[41] E. Andronescu, A.M. Grumezescu, M.-I. Guşă, A.M. Holban, F.-C. Ilie, A. Irimia, I.-F. Nicoară, M. Ţone, Chapter 6 - Nano-hydroxyapatite: Novel approaches in biomedical

applications, in: A.M. Grumezescu (Ed.), Nanobiomaterials in Hard Tissue Engineering, William Andrew Publishing2016, pp. 189-213.

[42] K. Byrappa, M. Yoshimura, 10 - Hydrothermal Technology for Nanotechnology—A Technology for Processing of Advanced Materials, in: K. Byrappa, M. Yoshimura (Eds.), Handbook of Hydrothermal Technology (Second Edition), William Andrew Publishing, Oxford, 2013, pp. 615-762.

[43] S. Feng, R. Xu, New Materials in Hydrothermal Synthesis, Accounts of Chemical Research 34(3) (2001) 239-247.

[44] L. Yubao, J. De Wijn, C.P.A.T. Klein, S. Van De Meer, K. De Groot, Preparation and characterization of nanograde osteoapatite-like rod crystals, Journal of Materials Science: Materials in Medicine 5(5) (1994) 252-255.

[45] L. Yan, Y. Li, Z.-X. Deng, J. Zhuang, X. Sun, Surfactant-assisted hydrothermal synthesis of hydroxyapatite nanorods, International Journal of Inorganic Materials 3(7) (2001) 633-637.

[46] R. Gonzalez-McQuire, J.-Y. Chane-Ching, E. Vignaud, A. Lebugle, S. Mann, Synthesis and characterization of amino acid-functionalized hydroxyapatite nanorods, Journal of Materials Chemistry 14(14) (2004) 2277-2281.

[47] X. Guo, P. Xiao, J. Liu, Z. Shen, Fabrication of Nanostructured Hydroxyapatite via Hydrothermal Synthesis and Spark Plasma Sintering, Journal of the American Ceramic Society 88(4) (2005) 1026-1029.

[48] F. Zhang, Z.-H. Zhou, S.-P. Yang, L.-H. Mao, H.-M. Chen, X.-B. Yu, Hydrothermal synthesis of hydroxyapatite nanorods in the presence of anionic starburst dendrimer, Materials Letters 59(11) (2005) 1422-1425.

[49] A. Wang, H. Yin, D. Liu, H. Wu, M. Ren, T. Jiang, X. Cheng, Y. Xu, Size-controlled synthesis of hydroxyapatite nanorods in the presence of organic modifiers, Materials Letters 61(10) (2007) 2084-2088.

[50] A. Wang, D. Liu, H. Yin, H. Wu, Y. Wada, M. Ren, T. Jiang, X. Cheng, Y. Xu, Size-controlled synthesis of hydroxyapatite nanorods by chemical precipitation in the presence of organic modifiers, Materials Science and Engineering: C 27(4) (2007) 865-869.

[51] M. Okada, T. Furuzono, Calcination of Rod-like Hydroxyapatite Nanocrystals with an Anti-sintering Agent Surrounding the Crystals, Journal of Nanoparticle Research 9(5) (2007) 807-815.

[52] K. Lin, J. Chang, R. Cheng, M. Ruan, Hydrothermal microemulsion synthesis of stoichiometric single crystal hydroxyapatite nanorods with mono-dispersion and narrow-size distribution, Materials Letters 61(8) (2007) 1683-1687.

[53] Y. Xu, J. Jiang, Y. Lu, R.-J. Sun, J. Song, L. Ren, S.-H. Yu, Facile Surfactant-Free Synthesis of Water-Dispersible Willow-Leaf-Like Carbonate Apatite Nanorods in Ethanol/Water Mixed Solution and Their Cytotoxicity, Crystal Growth & Design 8(10) (2008) 3822-3828.

[54] Y. Li, D. Li, Z. Xu, Synthesis of hydroxyapatite nanorods assisted by Pluronics, Journal of Materials Science 44(5) (2009) 1258-1263.

[55] C. Zhang, J. Yang, Z. Quan, P. Yang, C. Li, Z. Hou, J. Lin, Hydroxyapatite Nano- and Microcrystals with Multiform Morphologies: Controllable Synthesis and Luminescence Properties, Crystal Growth & Design 9(6) (2009) 2725-2733.

[56] C. Zhang, C. Li, S. Huang, Z. Hou, Z. Cheng, P. Yang, C. Peng, J. Lin, Self-activated luminescent and mesoporous strontium hydroxyapatite nanorods for drug delivery, Biomaterials 31(12) (2010) 3374-3383.

[57] G. Wu, L.-Z. Zhou, K.-w. Wang, F. Chen, Y. Sun, Y.-r. Duan, Y. Zhu, H. Gu, Hydroxylapatite nanorods: an efficient and promising carrier for gene transfection, Journal of colloid and interface science 345 2 (2010) 427-32.

[58] R. Xin, F. Ren, Y. Leng, Synthesis and characterization of nano-crystalline calcium phosphates with EDTA-assisted hydrothermal method, Materials & Design 31(4) (2010) 1691-1694.

[59] S. Manafi, M.R. Rahimipour, Synthesis of Nanocrystalline Hydroxyapatite Nanorods via Hydrothermal Conditions, Chemical Engineering & Technology 34(6) (2011) 972-976.

[60] A.J. Nathanael, D. Mangalaraj, S.I. Hong, Y. Masuda, Synthesis and in-depth analysis of highly ordered yttrium doped hydroxyapatite nanorods prepared by hydrothermal method and its mechanical analysis, Materials Characterization 62(12) (2011) 1109-1115.

[61] N.K. Nguyen, M. Leoni, D. Maniglio, C. Migliaresi, Hydroxyapatite nanorods: soft-template synthesis, characterization and preliminary in vitro tests, J Biomater Appl 28(1) (2013) 49-61.

[62] A. Joseph Nathanael, D. Mangalaraj, S.I. Hong, Y. Masuda, Y.H. Rhee, H.W. Kim, Influence of fluorine substitution on the morphology and structure of hydroxyapatite nanocrystals prepared by hydrothermal method, Materials Chemistry and Physics 137(3) (2013) 967-976.

[63] D. Gopi, N. Bhuvaneshwari, J. Indira, K. Kanimozhi, L. Kavitha, A novel green template assisted synthesis of hydroxyapatite nanorods and their spectral characterization, Spectrochimica Acta Part A: Molecular and Biomolecular Spectroscopy 107 (2013) 196-202.

[64] N.K. Nga, L.T. Giang, T.Q. Huy, P.H. Viet, C. Migliaresi, Surfactant-assisted size control of hydroxyapatite nanorods for bone tissue engineering, Colloids Surf B Biointerfaces 116 (2014) 666-73.

[65] Y. Yang, Q. Wu, M. Wang, J. Long, Z. Mao, X. Chen, Hydrothermal Synthesis of Hydroxyapatite with Different Morphologies: Influence of Supersaturation of the Reaction System, Crystal Growth & Design 14(9) (2014) 4864-4871.

[66] X.-Y. Zhao, Y.-J. Zhu, B.-Q. Lu, F. Chen, C. Qi, J. Zhao, J. Wu, Hydrothermal synthesis of hydroxyapatite nanorods using pyridoxal-5′-phosphate as a phosphorus source, Materials Research Bulletin 55 (2014) 67-70.

[67] X. Jin, X. Chen, Y. Cheng, L. Wang, B. Hu, J. Tan, Effects of hydrothermal temperature and time on hydrothermal synthesis of colloidal hydroxyapatite nanorods in the presence of sodium citrate, Journal of Colloid and Interface Science 450 (2015) 151-158.

[68] X. Jin, J. Zhuang, Z. Zhang, H. Guo, J. Tan, Hydrothermal synthesis of hydroxyapatite nanorods in the presence of sodium citrate and its aqueous colloidal stability evaluation in neutral pH, Journal of Colloid and Interface Science 443 (2015) 125-130.

[69] X. Zheng, M. Liu, J. Hui, D. Fan, H. Ma, X. Zhang, Y. Wang, Y. Wei, Ln3+-doped hydroxyapatite nanocrystals: controllable synthesis and cell imaging, Physical Chemistry Chemical Physics 17(31) (2015) 20301-20307.

[70] M.M. Taheri, M.R. Abdul Kadir, T. Shokuhfar, A. Hamlekhan, M. Assadian, M.R. Shirdar, A. Mirjalili, Surfactant-assisted hydrothermal synthesis of Fluoridated Hydroxyapatite nanorods, Ceramics International 41(8) (2015) 9867-9872.

[71] M. Filippousi, P.I. Siafaka, E.P. Amanatiadou, S.G. Nanaki, M. Nerantzaki, D.N. Bikiaris, I.S. Vizirianakis, G. Van Tendeloo, Modified chitosan coated mesoporous strontium hydroxyapatite nanorods as drug carriers, Journal of Materials Chemistry B 3(29) (2015) 5991-6000.

[72] D.M. Andrade Neto, E.V. Carvalho, E.A. Rodrigues, V.P. Feitosa, S. Sauro, G. Mele, L. Carbone, S.E. Mazzetto, L.K. Rodrigues, P.B. Fechine, Novel hydroxyapatite nanorods improve anti-caries efficacy of enamel infiltrants, Dent Mater 32(6) (2016) 784-93.

[73] M.F. Cipreste, I. Gonzalez, T. Maria da Mata Martins, A.M. Goes, W. Augusto de Almeida Macedo, E.M. Barros de Sousa, Attaching folic acid on hydroxyapatite nanorod

surfaces: an investigation of the HA–FA interaction, RSC Advances 6(80) (2016) 76390-76400.

[74] M.F. Cipreste, A.M. Peres, A.A.C. Cotta, F.H. Aragón, A.d.M. Antunes, A.S. Leal, W.A.A. Macedo, E.M.B. de Sousa, Synthesis and characterization of 159Gd-doped hydroxyapatite nanorods for bioapplications as theranostic systems, Materials Chemistry and Physics 181 (2016) 301-311.

[75] T.T. Hoai, N.K. Nga, L.T. Giang, T.Q. Huy, P.N.M. Tuan, B.T.T. Binh, Hydrothermal Synthesis of Hydroxyapatite Nanorods for Rapid Formation of Bone-Like Mineralization, Journal of Electronic Materials 46(8) (2017) 5064-5072.

[76] M. Buitrago-Vásquez, C.P. Ossa-Orozco, Hydrothermal synthesis of hydroxyapatite nanorods using a fruit extract template, DYNA 85 (2018) 283-288.

[77] W.P.S.L. Wijesinghe, M.M.M.G.P.G. Mantilaka, R.M.G. Rajapakse, H.M.T.G.A. Pitawala, T.N. Premachandra, H.M.T.U. Herath, R.P.V.J. Rajapakse, K.G.U. Wijayantha, Urea-assisted synthesis of hydroxyapatite nanorods from naturally occurring impure apatite rocks for biomedical applications, RSC Advances 7(40) (2017) 24806-24812.

[78] X. Zheng, J. Hui, H. Li, C. Zhu, X. Hua, H. Ma, D. Fan, Fabrication of novel biodegradable porous bone scaffolds based on amphiphilic hydroxyapatite nanorods, Materials Science and Engineering: C 75 (2017) 699-705.

[79] Y.-D. Yu, Y.-J. Zhu, C. Qi, Y.-Y. Jiang, H. Li, J. Wu, Hydroxyapatite nanorod-assembled porous hollow polyhedra as drug/protein carriers, Journal of Colloid and Interface Science 496 (2017) 416-424.

[80] G.M. Hernández Ortiz, R. Parra, M.A. Fanovich, Comparative hydrothermal synthesis of hydroxyapatite by using cetyltrimethylammonium bromide and hexamethylenetetramine as additives, Ceramics International 44(4) (2018) 3658-3663.

[81] H. Bensalah, M.F. Bekheet, S. Alami Younssi, M. Ouammou, A. Gurlo, Hydrothermal synthesis of nanocrystalline hydroxyapatite from phosphogypsum waste, Journal of Environmental Chemical Engineering 6(1) (2018) 1347-1352.

[82] M.F. Alif, W. Aprillia, S. Arief, A hydrothermal synthesis of natural hydroxyapatite obtained from Corbicula moltkiana freshwater clams shell biowaste, Materials Letters 230 (2018) 40-43.

[83] J. Liu, K. Li, H. Wang, M. Zhu, H. Xu, H. Yan, Self-assembly of hydroxyapatite nanostructures by microwave irradiation, Nanotechnology 16(1) (2004) 82-87.

[84] A. Kumar, Y. Kuang, Z. Liang, X. Sun, Microwave chemistry, recent advancements, and eco-friendly microwave-assisted synthesis of nanoarchitectures and their applications: a review, Materials Today Nano 11 (2020) 100076.

[85] W. Amer, K. Abdelouahdi, H.R. Ramananarivo, M. Zahouily, A. Fihri, Y. Coppel, R.S. Varma, A. Solhy, Synthesis of mesoporous nano-hydroxyapatite by using zwitterions surfactant, Materials Letters 107 (2013) 189-193.

[86] G.S. Kumar, L. Sathish, R. Govindan, E.K. Girija, Utilization of snail shells to synthesise hydroxyapatite nanorods for orthopedic applications, RSC Advances 5(49) (2015) 39544-39548.

[87] V.K. Mishra, S.K. Srivastava, B.P. Asthana, D. Kumar, Structural and Spectroscopic Studies of Hydroxyapatite Nanorods Formed via Microwave-Assisted Synthesis Route, Journal of the American Ceramic Society 95(9) (2012) 2709-2715.

[88] S. Agrawal, M. Kelkar, A. De, A.R. Kulkarni, M.N. Gandhi, Surfactant free novel one-minute microwave synthesis, characterization and cell toxicity study of mesoporous strontium hydroxyapatite nanorods, RSC Advances 6(97) (2016) 94921-94926.

[89] M. Shkir, M. Kilany, I.S. Yahia, Facile microwave-assisted synthesis of tungsten-doped hydroxyapatite nanorods: A systematic structural, morphological, dielectric, radiation and microbial activity studies, Ceramics International 43(17) (2017) 14923-14931.

[90] I.S. Yahia, M. Shkir, S. AlFaify, V. Ganesh, H.Y. Zahran, M. Kilany, Facile microwave-assisted synthesis of Te-doped hydroxyapatite nanorods and nanosheets and their characterizations for bone cement applications, Materials Science and Engineering: C 72 (2017) 472-480.

[91] M.M. Abutalib, I.S. Yahia, Novel and facile microwave-assisted synthesis of Mo-doped hydroxyapatite nanorods: Characterization, gamma absorption coefficient, and bioactivity, Materials Science and Engineering: C 78 (2017) 1093-1100.

[92] V. Kalaiselvi, R. Mathammal, S. Vijayakumar, B. Vaseeharan, Microwave assisted green synthesis of Hydroxyapatite nanorods using Moringa oleifera flower extract and its antimicrobial applications, International Journal of Veterinary Science and Medicine 6(2) (2018) 286-295.

[93] R. Al-Wafi, A.A. Al-Ghamdi, R. Jafer, A.A. Al-Judaibi, M.A. Al-Ghamdi, I.S. Yahia, O. Albulym, A.M. El-Naggar, Rapid synthesis of cesium-doped hydroxyapatite nanorods: characterisation and microbial activity, Advances in Applied Ceramics 118(6) (2019) 340-350.

[94] G. Karunakaran, E.-B. Cho, G.S. Kumar, E. Kolesnikov, G. Janarthanan, M.M. Pillai, S. Rajendran, S. Boobalan, M.V. Gorshenkov, D. Kuznetsov, Ascorbic Acid-Assisted Microwave Synthesis of Mesoporous Ag-Doped Hydroxyapatite Nanorods from Biowaste Seashells for Implant Applications, ACS Applied Bio Materials 2(5) (2019) 2280-2293.

[95] P. Agalya, T. Saravanan, G.S. Kumar, S. Cholan, G. Karunakaran, N. Van Minh, Surfactant-assisted microwave synthesis of luminescent/magnetic bifunctional hydroxyapatite nanorods for dual-model imaging, Optik 225 (2021) 165564.

[96] G. Karunakaran, E.B. Cho, K. Thirumurugan, G.S. Kumar, E. Kolesnikov, S. Boobalan, G. Janarthanan, M.M. Pillai, S. Rajendran, Mesoporous Mn-doped hydroxyapatite nanorods obtained via pyridinium chloride enabled microwave-assisted synthesis by utilizing Donax variabilis seashells for implant applications, Mater Sci Eng C Mater Biol Appl 126 (2021) 112170.

[97] D. Muthu, G. Suresh Kumar, M. Gowri, M. Prasath, V. Viswabaskaran, V.S. Kattimani, E.K. Girija, Rapid synthesis of eggshell derived hydroxyapatite with nanoscale characteristics for biomedical applications, Ceramics International 48(1) (2022) 1326-1339.

[98] J. Zhan, Y.-H. Tseng, J.C.C. Chan, C.-Y. Mou, Biomimetic Formation of Hydroxyapatite Nanorods by a Single-Crystal-to-Single-Crystal Transformation, Advanced Functional Materials 15(12) (2005) 2005-2010.

[99] H. Chen, K. Sun, Z. Tang, R.V. Law, J.F. Mansfield, A. Czajka-Jakubowska, B.H. Clarkson, Synthesis of Fluorapatite Nanorods and Nanowires by Direct Precipitation from Solution, Crystal Growth & Design 6(6) (2006) 1504-1508.

[100] J. Tan, M. Chen, J. Xia, Water-dispersible hydroxyapatite nanorods synthesized by a facile method, Applied Surface Science 255(21) (2009) 8774-8779.

[101] G. Verma, K.C. Barick, N. Manoj, A.K. Sahu, P.A. Hassan, Rod-like micelle templated synthesis of porous hydroxyapatite, Ceramics International 39(8) (2013) 8995-9002.

[102] F. Mohandes, M. Salavati-Niasari, Particle size and shape modification of hydroxyapatite nanostructures synthesized via a complexing agent-assisted route, Materials Science and Engineering: C 40 (2014) 288-298.

[103] W.I. Mortada, I.M.M. Kenawy, A.M. Abdelghany, A.M. Ismail, A.F. Donia, K.A. Nabieh, Determination of Cu2+, Zn2+ and Pb2+ in biological and food samples by FAAS after preconcentration with hydroxyapatite nanorods originated from eggshell, Materials Science and Engineering: C 52 (2015) 288-296.

[104] A. Clifford, M.S. Ata, I. Zhitomirsky, Synthesis, liquid – Liquid extraction and deposition of hydroxyapatite nanorod composites, Materials Letters 201 (2017) 140-143.

[105] S. Mondal, V.T. Nguyen, S. Park, J. Choi, L.H. Tran, M. Yi, J.H. Shin, C.-Y. Lee, J. Oh, Bioactive, luminescent erbium-doped hydroxyapatite nanocrystals for biomedical applications, Ceramics International 46(10, Part B) (2020) 16020-16031.

[106] M. Jevtić, M. Mitrić, S. Škapin, B. Jančar, N. Ignjatović, D. Uskoković, Crystal Structure of Hydroxyapatite Nanorods Synthesized by Sonochemical Homogeneous Precipitation, Crystal Growth & Design 8(7) (2008) 2217-2222.

[107] S.K. Padmanabhan, A. Balakrishnan, M.-C. Chu, Y.J. Lee, T.N. Kim, S.-J. Cho, Sol–gel synthesis and characterization of hydroxyapatite nanorods, Particuology 7(6) (2009) 466-470.

[108] S. Jadalannagari, S. More, M. Kowshik, S.R. Ramanan, Low temperature synthesis of hydroxyapatite nano-rods by a modified sol–gel technique, Materials Science and Engineering: C 31(7) (2011) 1534-1538.

[109] R.K. Singh, T.-H. Kim, K.D. Patel, J.-J. Kim, H.-W. Kim, Development of biocompatible apatite nanorod-based drug-delivery system with in situ fluorescence imaging capacity, Journal of Materials Chemistry B 2(14) (2014) 2039-2050.

[110] Z. Ning, Z. Chang, W. Li, C. Sun, J. Zhang, Y. Liu, Solvothermal Synthesis and Optical Performance of One-dimensional Strontium Hydroxyapatite Nanorod, Chinese Journal of Chemical Engineering 20(1) (2012) 89-94.

[111] F. Chen, Y.-J. Zhu, X.-Y. Zhao, B.-Q. Lu, J. Wu, Solvothermal synthesis of oriented hydroxyapatite nanorod/nanosheet arrays using creatine phosphate as phosphorus source, CrystEngComm 15(22) (2013) 4527-4531.

[112] H. Yang, T. Liang, X. Qi, H. Jiang, Y. Deng, P. Wang, H. Gao, Solvothermal synthesis of hydroxyapatite nanorods with assistance of green polymer, Materials Science and Engineering: C 79 (2017) 9-14.

[113] A. Khalil, A. Almajid, M. Soliman, Effect of Hydroxide Ion Concentration on the Morphology of the Hydroxyapatite Nanorods Synthesized Using Electrophoretic Deposition, Materials Sciences and Applications 02 (2011) 105-110.

[114] X. Guo, J.E. Gough, P. Xiao, J. Liu, Z. Shen, Fabrication of nanostructured hydroxyapatite and analysis of human osteoblastic cellular response, Journal of Biomedical Materials Research Part A 82A(4) (2007) 1022-1032.

[115] Y. Ji, A. Wang, G. Wu, H. Yin, S. Liu, B. Chen, F. Liu, X. Li, Synthesis of different sized and porous hydroxyapatite nanorods without organic modifiers and their 5-fluorouracil release performance, Materials Science and Engineering: C 57 (2015) 14-23.

[116] G.S. Kumar, G. Karunakaran, E.K. Girija, E. Kolesnikov, N.V. Minh, M.V. Gorshenkov, D. Kuznetsov, Size and morphology-controlled synthesis of mesoporous hydroxyapatite nanocrystals by microwave-assisted hydrothermal method, Ceramics International 44(10) (2018) 11257-11264.

[117] J. Chen, J. Liu, H. Deng, S. Yao, Y. Wang, Regulatory synthesis and characterization of hydroxyapatite nanocrystals by a microwave-assisted hydrothermal method, Ceramics International 46(2) (2020) 2185-2193.

[118] A.F. Ali, Z.A. Alrowaili, E.M. El-Giar, M.M. Ahmed, A.M. El-Kady, Novel green synthesis of hydroxyapatite uniform nanorods via microwave-hydrothermal route using licorice root extract as template, Ceramics International 47(3) (2021) 3928-3937.

[119] D. Mehta, P. Mondal, V.K. Saharan, S. George, Synthesis of hydroxyapatite nanorods for application in water defluoridation and optimization of process variables: Advantage of ultrasonication with precipitation method over conventional method, Ultrasonics Sonochemistry 37 (2017) 56-70.

[120] J. Chen, Z. Wen, S. Zhong, Z. Wang, J. Wu, Q. Zhang, Synthesis of hydroxyapatite nanorods from abalone shells via hydrothermal solid-state conversion, Materials & Design 87 (2015) 445-449.

[121] H. Nosrati, R.S. Mamoory, D.Q.S. Le, C.E. Bünger, R.Z. Emameh, F. Dabir, Gas injection approach for synthesis of hydroxyapatite nanorods via hydrothermal method, Materials Characterization 159 (2020) 110071.

[122] H. Nosrati, R. Sarraf-Mamoory, D.Q.S. Le, M.C. Perez, C.E. Bünger, Evaluation of Argon-Gas-Injected Solvothermal Synthesis of Hydroxyapatite Crystals Followed by High-Frequency Induction Heat Sintering, Crystal Growth & Design 20(5) (2020) 3182-3189.

[123] Y. Wang, X. Ren, X. Ma, W. Su, Y. Zhang, X. Sun, X. Li, Alginate-Intervened Hydrothermal Synthesis of Hydroxyapatite Nanocrystals with Nanopores, Crystal Growth & Design 15(4) (2015) 1949-1956.

[124] J. Zhang, D. Jiang, J. Zhang, Q. Lin, Z. Huang, Synthesis of organized hydroxyapatite (HA) using triton X-100, Ceramics International 36(8) (2010) 2441-2447.

[125] S.K. Saha, A. Banerjee, S. Banerjee, S. Bose, Synthesis of nanocrystalline hydroxyapatite using surfactant template systems: Role of templates in controlling morphology, Materials Science and Engineering: C 29(7) (2009) 2294-2301.

[126] S. Bose, S.K. Saha, Synthesis and Characterization of Hydroxyapatite Nanopowders by Emulsion Technique, Chemistry of Materials 15(23) (2003) 4464-4469.

[127] K. Shiba, S. Motozuka, T. Yamaguchi, N. Ogawa, Y. Otsuka, K. Ohnuma, T. Kataoka, M. Tagaya, Effect of Cationic Surfactant Micelles on Hydroxyapatite Nanocrystal Formation: An Investigation into the Inorganic–Organic Interfacial Interactions, Crystal Growth & Design 16(3) (2016) 1463-1471.

[128] X. Wang, J. Zhuang, Q. Peng, Y.D. Li, Liquid–Solid–Solution Synthesis of Biomedical Hydroxyapatite Nanorods, Advanced Materials 18(15) (2006) 2031-2034.

[129] R. Subramanian, P. Murugan, G. Chinnadurai, K. Ponmurugan, N.A. Al-Dhabi, Experimental studies on caffeine mediated synthesis of hydroxyapatite nanorods and their characterization, Materials Research Express 7(1) (2020) 015022.

[130] K. Alorku, M. Manoj, A. Yuan, A plant-mediated synthesis of nanostructured hydroxyapatite for biomedical applications: a review, RSC Advances 10(67) (2020) 40923-40939.

[131] Z. Evis, T.J. Webster, Nanosize hydroxyapatite: doping with various ions, Advances in Applied Ceramics 110(5) (2011) 311-321.

[132] G. Chen, X. Zheng, C. Wang, J. Hui, X. Sheng, X. Xu, J. Bao, W. Xiu, L. Yuwen, D. Fan, A postsynthetic ion exchange method for tunable doping of hydroxyapatite nanocrystals, RSC Advances 7(89) (2017) 56537-56542.

[133] Y. Zhou, W. Li, X. Jiang, Y. Sun, H. Yang, Q. Liu, Y. Cao, Y. Zhang, H. Cheng, Synthesis of strontium (Sr) doped hydroxyapatite (HAp) nanorods for enhanced adsorption of Cr (VI) ions from wastewater, Ceramics International 47(12) (2021) 16730-16736.

[134] G. Karunakaran, E.-B. Cho, G.S. Kumar, E. Kolesnikov, A. Dmitry, S. Ali, Microwave-assisted synthesis of superparamagnetic mesoporous Co-doped hydroxyapatite nanorods for various biomedical applications, Ceramics International 47(6) (2021) 8642-8652.

[135] F.Y. Rajhi, I.S. Yahia, H.Y. Zahran, M. Kilany, Synthesis, structural, optical, dielectric properties, gamma radiation attenuation, and antimicrobial activity of V-doped hydroxyapatite nanorods, Materials Today Communications 26 (2021) 101981.

[136] Q. Fan, F. Fan, W. Xu, H. Zhang, N. Liu, The structural and surface properties of Al-doped hydroxyapatite (Ca5(PO4)3OH) nanorods and their applications for pH-induced drug delivery, Journal of Alloys and Compounds 879 (2021) 160414.

[137] X. Wang, S. Ihara, X. Li, A. Ito, Y. Sogo, Y. Watanabe, N.M. Tsuji, A. Yamazaki, Si-doping increases the adjuvant activity of hydroxyapatite nanorods, Colloids and Surfaces B: Biointerfaces 174 (2019) 300-307.

[138] C. Xue, Y. Chen, Y. Huang, P. Zhu, Hydrothermal Synthesis and Biocompatibility Study of Highly Crystalline Carbonated Hydroxyapatite Nanorods, Nanoscale Research Letters 10(1) (2015) 316.

[139] Y. Zhou, C. Ge, P. Zhou, J. Jin, Y. Zhu, B. Xu, X. Zhang, K.A. Al-Ghanim, S. Mahboob, Fluorine doped calcium deficient hydroxyapatite nanorod bundles as theranostic nanoplatforms, Materials Letters 264 (2020) 127297.

[140] R.-L. Yang, Y.-J. Zhu, F.-F. Chen, L.-Y. Dong, Z.-C. Xiong, Luminescent, Fire-Resistant, and Water-Proof Ultralong Hydroxyapatite Nanowire-Based Paper for Multimode Anticounterfeiting Applications, ACS Applied Materials & Interfaces 9(30) (2017) 25455-25464.

[141] T.-W. Sun, Y.-J. Zhu, F. Chen, F.-F. Chen, Y.-Y. Jiang, Y.-G. Zhang, J. Wu, Ultralong hydroxyapatite nanowires/collagen scaffolds with hierarchical porous structure, enhanced mechanical properties and excellent cellular attachment, Ceramics International 43(17) (2017) 15747-15754.

[142] T.-W. Sun, W.-L. Yu, Y.-J. Zhu, R.-L. Yang, Y.-Q. Shen, D.-Y. Chen, Y.-H. He, F. Chen, Hydroxyapatite Nanowire@Magnesium Silicate Core–Shell Hierarchical Nanocomposite: Synthesis and Application in Bone Regeneration, ACS Applied Materials & Interfaces 9(19) (2017) 16435-16447.

[143] T.W. Sun, Y.J. Zhu, F. Chen, Y.G. Zhang, Ultralong Hydroxyapatite Nanowire/Collagen Biopaper with High Flexibility, Improved Mechanical Properties and Excellent Cellular Attachment, Chem Asian J 12(6) (2017) 655-664.

[144] F.F. Chen, Y.J. Zhu, Hydroxyapatite Nanowire-Based All-Weather Flexible Electrically Conductive Paper with Superhydrophobic and Flame-Retardant Properties, 9(45) (2017) 39534-39548.

[145] R.-L. Yang, Y.-J. Zhu, F.-F. Chen, D.-D. Qin, Z.-C. Xiong, Recyclable, Fire-Resistant, Superhydrophobic, and Magnetic Paper Based on Ultralong Hydroxyapatite Nanowires for Continuous Oil/Water Separation and Oil Collection, ACS Sustainable Chemistry & Engineering 6(8) (2018) 10140-10150.

[146] R.-L. Yang, Y.-J. Zhu, F.-F. Chen, D.-D. Qin, Z.-C. Xiong, Bioinspired Macroscopic Ribbon Fibers with a Nacre-Mimetic Architecture Based on Highly Ordered Alignment of Ultralong Hydroxyapatite Nanowires, ACS Nano 12(12) (2018) 12284-12295.

[147] T.-W. Sun, Y.-J. Zhu, Solvothermal Growth of Ultralong Hydroxyapatite Nanowire Coating on Glass Substrate, Chemistry Letters 48(12) (2019) 1462-1464.

[148] Q.-Q. Zhang, Y.-J. Zhu, J. Wu, Y.-T. Shao, A.-Y. Cai, L.-Y. Dong, Ultralong Hydroxyapatite Nanowire-Based Filter Paper for High-Performance Water Purification, ACS Applied Materials & Interfaces 11(4) (2019) 4288-4301.

[149] H. Yuan, X. Zheng, W. Liu, H. Zhang, J. Shao, J. Yao, C. Mao, J. Hui, D. Fan, A novel bovine serum albumin and sodium alginate hydrogel scaffold doped with hydroxyapatite nanowires for cartilage defects repair, Colloids and Surfaces B: Biointerfaces 192 (2020) 111041.

[150] J. Zhu, F. Zhao, T. Peng, H. Liu, L. Xie, C. Jiang, Highly elastic and robust hydroxyapatite nanowires/polyimide composite aerogel with anisotropic structure for thermal insulation, Composites Part B: Engineering 223 (2021) 109081.

[151] J. Zou, S. Xiaogang, R. Li, Q. He, Hydroxyapatite nanowires prepare high-performance tin-phosphate anode, Colloids and Surfaces A: Physicochemical and Engineering Aspects 602 (2020) 124757.

[152] Z. Yang, Y. Huang, S.-T. Chen, Y.-Q. Zhao, H.-L. Li, Z.-A. Hu, Template synthesis of highly ordered hydroxyapatite nanowire arrays, Journal of Materials Science 40(5) (2005) 1121-1125.

[153] Y.-G. Zhang, Y.-J. Zhu, F. Chen, J. Wu, Ultralong hydroxyapatite nanowires synthesized by solvothermal treatment using a series of phosphate sodium salts, Materials Letters 144 (2015) 135-137.

[154] Y.-Y. Jiang, Y.-J. Zhu, F. Chen, J. Wu, Solvothermal synthesis of submillimeter ultralong hydroxyapatite nanowires using a calcium oleate precursor in a series of monohydroxy alcohols, Ceramics International 41(4) (2015) 6098-6102.

[155] Y.-G. Zhang, Y.-J. Zhu, F. Chen, T.-W. Sun, Y.-Y. Jiang, Highly porous ceramics based on ultralong hydroxyapatite nanowires, RSC Advances 6(104) (2016) 102003-102009.

[156] J. He, K. Zhang, S. Wu, X. Cai, K. Chen, Y. Li, B. Sun, Y. Jia, F. Meng, Z. Jin, L. Kong, J. Liu, Performance of novel hydroxyapatite nanowires in treatment of fluoride contaminated water, Journal of Hazardous Materials 303 (2016) 119-130.

[157] Y.-Y. Jiang, Y.-J. Zhu, H. Li, Y.-G. Zhang, Y.-Q. Shen, T.-W. Sun, F. Chen, Preparation and enhanced mechanical properties of hybrid hydrogels comprising ultralong hydroxyapatite nanowires and sodium alginate, Journal of Colloid and Interface Science 497 (2017) 266-275.

[158] Z.-C. Xiong, Z.-Y. Yang, Y.-J. Zhu, F.-F. Chen, Y.-G. Zhang, R.-L. Yang, Ultralong Hydroxyapatite Nanowires-Based Paper Co-Loaded with Silver Nanoparticles and Antibiotic for Long-Term Antibacterial Benefit, ACS Applied Materials & Interfaces 9(27) (2017) 22212-22222.

[159] Z.-C. Xiong, Z.-Y. Yang, Y.-J. Zhu, F.-F. Chen, R.-L. Yang, D.-D. Qin, Ultralong hydroxyapatite nanowire-based layered catalytic paper for highly efficient continuous flow reactions, Journal of Materials Chemistry A 6(14) (2018) 5762-5773.

[160] L. Zhang, Y. Luo, Y. Zhao, B. Guan, L. Zhang, B. Yu, W. Zhang, Silver nanoparticle-incorporated ultralong hydroxyapatite nanowires with internal reference as SERS substrate for trace environmental pollutant detection, New Journal of Chemistry 42(22) (2018) 17950-17957.

[161] D.-D. Qin, Y.-J. Zhu, F.-F. Chen, R.-L. Yang, Z.-C. Xiong, Self-floating aerogel composed of carbon nanotubes and ultralong hydroxyapatite nanowires for highly efficient solar energy-assisted water purification, Carbon 150 (2019) 233-243.

[162] H.-P. Yu, Y.-J. Zhu, B.-Q. Lu, Highly efficient and environmentally friendly microwave-assisted hydrothermal rapid synthesis of ultralong hydroxyapatite nanowires, Ceramics International 44(11) (2018) 12352-12356.

[163] Y.-Q. Chen, Y.-J. Zhu, Z.-Y. Wang, H.-P. Yu, Z.-C. Xiong, A scalable, low-cost and green strategy for the synthesis of ultralong hydroxyapatite nanowires using peanut oil, CrystEngComm 24(17) (2022) 3208-3216.

[164] K. Lin, X. Liu, J. Chang, Y. Zhu, Facile synthesis of hydroxyapatite nanoparticles, nanowires and hollow nano-structured microspheres using similar structured hard-precursors, Nanoscale 3(8) (2011) 3052-3055.

[165] D.O. Costa, S.J. Dixon, A.S. Rizkalla, One- and Three-Dimensional Growth of Hydroxyapatite Nanowires during Sol–Gel–Hydrothermal Synthesis, ACS Applied Materials & Interfaces 4(3) (2012) 1490-1499.

[166] T.-G. Kim, B. Park, Synthesis and Growth Mechanisms of One-Dimensional Strontium Hydroxyapatite Nanostructures, Inorganic Chemistry 44(26) (2005) 9895-9901.

[167] S. Bramhe, T.N. Kim, A. Balakrishnan, M.C. Chu, Conversion from biowaste Venerupis clam shells to hydroxyapatite nanowires, Materials Letters 135 (2014) 195-198.

[168] C. Qi, Y.-J. Zhu, T.-W. Sun, J. Wu, F. Chen, Microwave-Assisted Hydrothermal Rapid Synthesis of Amorphous Calcium Phosphate Mesoporous Microspheres Using Adenosine 5′-

Diphosphate and Application in pH-Responsive Drug Delivery, Chemistry – An Asian Journal 10(11) (2015) 2503-2511.

[169] C. Shu, W. Yanwei, L. Hong, P. Zhengzheng, Y. Kangde, Synthesis of carbonated hydroxyapatite nanofibers by mechanochemical methods, Ceramics International 31(1) (2005) 135-138.

[170] M.-L. Qi, K. He, Z.-N. Huang, R. Shahbazian-Yassar, G.-Y. Xiao, Y.-P. Lu, T. Shokuhfar, Hydroxyapatite Fibers: A Review of Synthesis Methods, JOM 69(8) (2017) 1354-1360.

[171] M. Cao, Y. Wang, C. Guo, Y. Qi, C. Hu, Preparation of Ultrahigh-Aspect-Ratio Hydroxyapatite Nanofibers in Reverse Micelles under Hydrothermal Conditions, Langmuir 20(11) (2004) 4784-4786.

[172] S. Gao, K. Sun, A. Li, H. Wang, Synthesis and characterization of hydroxyapatite nanofiber by chemical precipitation method using surfactants, Materials Research Bulletin 48(3) (2013) 1003-1006.

[173] L. Liu, J. Huang, Y. Feng, J. Liu, X. Yu, Synthesis and characterization of ultralong nanofibrillar and hydroxyapatite powder, Advanced Powder Technology 26(2) (2015) 428-433.

[174] R.M. Tripathi, N. Kumar, A. Singh Bhadwal, R.K. Gupta, B.R. Shrivastav, A. Shrivastav, Facile and rapid biomimetic approach for synthesis of HAp nanofibers and evaluation of their photocatalytic activity, Materials Letters 140 (2015) 64-67.

[175] N. Mendez, R. Velázquez-Castillo, E. Rivera-Muñoz, L. Bucio, G. Mondragón-Galicia, A. Manzano-Ramírez, M. Ocampo, L. Apátiga-Castro, Crystal Growth and structural analysis of hydroxyapatite nanofibers synthesized by the hydrothermal microwave-assisted method, Ceramics International 43 (2017) 451-457.

[176] Y.-c. Wang, W.-l. Xu, Y.-p. Lu, W.-h. Xu, H. Yin, G.-y. Xiao, Investigation of nature of starting materials on the construction of hydroxyapatite 1D/3D morphologies, Materials Science and Engineering: C 108 (2020) 110408.

[177] K. Suchanek, A. Bartkowiak, M. Perzanowski, M. Marszalek, From monetite plate to hydroxyapatite nanofibers by monoethanolamine assisted hydrothermal approach OPEN, Scientific Reports 8 (2018) 15408.

[178] J. Xue, T. Wu, Y. Dai, Y. Xia, Electrospinning and Electrospun Nanofibers: Methods, Materials, and Applications, Chemical Reviews 119(8) (2019) 5298-5415.

[179] D. Li, J.T. McCann, Y. Xia, M. Marquez, Electrospinning: A Simple and Versatile Technique for Producing Ceramic Nanofibers and Nanotubes, Journal of the American Ceramic Society 89(6) (2006) 1861-1869.

[180] D. Malwal, G. Packirisamy, Fabrication and Applications of Ceramic nanofibers in Water Remediation: A review, Critical Reviews in Environmental Science and Technology 46 (2015) 00-00.

[181] J.-H. Lee, Y.-J. Kim, Hydroxyapatite nanofibers fabricated through electrospinning and sol–gel process, Ceramics International 40(2) (2014) 3361-3369.

[182] C. Luo, S. Stoyanov, E. Stride, E. Pelan, M. Edirisinghe, Electrospinning versus fibre production methods: from specifics to technological convergence, Chemical Society reviews 41 13 (2012) 4708-35.

[183] J. Holopainen, M. Ritala, Rapid production of bioactive hydroxyapatite fibers via electroblowing, Journal of the European Ceramic Society 36(13) (2016) 3219-3224.

[184] X. Qiao, Y. Huang, H. Cheng, H.J. Seo, Facile preparation of hydroxyapatite nanofibers from mineralization of CaAlB3O7 powders in K2HPO4 solutions, Materials Letters 161 (2015) 459-463.

[185] Y. Mu, K. Zhu, J. Luan, S. Zhang, C. Zhang, R. Na, Y. Yang, X. Zhang, G. Wang, Fabrication of hybrid ultrafiltration membranes with improved water separation properties by incorporating environmentally friendly taurine modified hydroxyapatite nanotubes, Journal of Membrane Science 577 (2019) 274-284.

[186] H. Wang, L. Ming, L. Jia, L. Li, G. Wang, Y. Zhang, G.H. Li, Surfactant-Assisted in situ Chemical Etching for the General Synthesis of ZnO Nanotubes Array, Nanoscale research letters 5 (2010) 1102-6.

[187] H. Hillebrenner, F. Buyukserin, J.D. Stewart, C.R. Martin, Template synthesized nanotubes for biomedical delivery applications, Nanomedicine 1(1) (2006) 39-50.

[188] H.J. Fan, U. Gösele, M. Zacharias, Formation of nanotubes and hollow nanoparticles based on Kirkendall and diffusion processes: a review, Small (Weinheim an der Bergstrasse, Germany) 3(10) (2007) 1660-71.

[189] Y. Yuan, C. Liu, Y. Zhang, X. Shan, Sol–gel auto-combustion synthesis of hydroxyapatite nanotubes array in porous alumina template, Materials Chemistry and Physics 112(1) (2008) 275-280.

[190] B.B. Chandanshive, P. Rai, A.L. Rossi, O. Ersen, D. Khushalani, Synthesis of hydroxyapatite nanotubes for biomedical applications, Materials Science and Engineering: C 33(5) (2013) 2981-2986.

[191] R.K. Singh, A.M. El-Fiqi, K.D. Patel, H.-W. Kim, A novel preparation of magnetic hydroxyapatite nanotubes, Materials Letters 75 (2012) 130-133.

[192] Q. Sun, J.-T. Lou, F. Kang, J.-F. Chen, J.-X. Wang, Facile preparation of hydroxyapatite nanotubes assisted by needle-like calcium carbonate, Powder Technology 261 (2014) 49-54.

[193] X. Guo, L. Yu, L. Chen, H. Zhang, L. Peng, X. Guo, W. Ding, Organoamine-assisted biomimetic synthesis of faceted hexagonal hydroxyapatite nanotubes with prominent

stimulation activity for osteoblast proliferation, Journal of Materials Chemistry B 2(13) (2014) 1760-1763.

[194] H. Wang, C. Wang, B. Xiao, L. Zhao, J. Zhang, Y. Zhu, X. Guo, The hydroxyapatite nanotube as a promoter to optimize the HDS reaction of NiMo/TiO2 catalyst, Catalysis Today 259 (2016) 340-346.

[195] J. Hui, G. Xiang, X. Xu, J. Zhuang, X. Wang, Monodisperse F-Substituted Hydroxyapatite Single-Crystal Nanotubes with Amphiphilic Surface Properties, Inorganic Chemistry 48(13) (2009) 5614-5616.

[196] S. Beaufils, T. Rouillon, P. Millet, J. Le Bideau, P. Weiss, J.P. Chopart, A.L. Daltin, Synthesis of calcium-deficient hydroxyapatite nanowires and nanotubes performed by template-assisted electrodeposition, Mater Sci Eng C Mater Biol Appl 98 (2019) 333-346.

[197] L. Yubao, K. De Groot, J. De Wijn, C.P.A.T. Klein, S.V.D. Meer, Morphology and composition of nanograde calcium phosphate needle-like crystals formed by simple hydrothermal treatment, Journal of Materials Science: Materials in Medicine 5(6) (1994) 326-331.

[198] X. Ma, Y. Li, C. Wang, Y. Sun, Y. Ma, X. Dong, J. Qian, Y. Yuan, C. Liu, Controlled synthesis and transformation of nano-hydroxyapatite with tailored morphologies for biomedical applications, Journal of Materials Chemistry B 5(46) (2017) 9148-9156.

[199] H. Ito, Y. Oaki, H. Imai, Selective Synthesis of Various Nanoscale Morphologies of Hydroxyapatite via an Intermediate phase, Crystal Growth & Design 8(3) (2008) 1055-1059.

[200] T. Kobayashi, S. Ono, S. Hirakura, Y. Oaki, H. Imai, Morphological variation of hydroxyapatite grown in aqueous solution based on simulated body fluid, CrystEngComm 14(3) (2012) 1143-1149.

[201] N. Zheng, L. Yin, M. Su, Z. Liu, D.C.W. Tsang, D. Chen, Synthesis of shape and structure-dependent hydroxyapatite nanostructures as a superior adsorbent for removal of U(VI), Chemical Engineering Journal 384 (2020) 123262.

[202] W. Zhou, Z. Hu, T. Wang, G. Yang, W. Xi, Y. Gan, W. Lu, J. Hu, Enhanced corrosion resistance and bioactivity of Mg alloy modified by Zn-doped nanowhisker hydroxyapatite coatings, Colloids and Surfaces B: Biointerfaces 186 (2020) 110710.

[203] M.-l. Qi, Z. Huang, A. Phakatkar, W. Yao, Y. Yuan, T. Foroozan, G.-y. Xiao, R. Shahbazian-Yassar, Y.-p. Lu, T. Shokuhfar, Facile hydrothermal synthesis of antibacterial multi-layered hydroxyapatite nanostructures with superior flexibility, CrystEngComm 20(9) (2018) 1304-1312.

[204] Y. Wan, C. Wu, G. Zuo, G. Xiong, J. Jin, R. Guo, Z. Wang, H. Luo, Controlled template synthesis of lamellar hydroxyapatite nanoplates as a potential carrier for gene delivery, Materials Chemistry and Physics 156 (2015) 238-246.

[205] G. Zuo, Y. Wan, Y. Zhang, Preparation and characterization of a novel laminated magnetic hydroxyapatite for application on gene delivery, Materials Letters 68 (2012) 225-227.

[206] J. Jin, G. Zuo, G. Xiong, H. Luo, Q. Li, C. Ma, D. Li, F. Gu, Y. Ma, Y. Wan, The inhibition of lamellar hydroxyapatite and lamellar magnetic hydroxyapatite on the migration and adhesion of breast cancer cells, Journal of Materials Science: Materials in Medicine 25(4) (2014) 1025-1031.

[207] Y. Wan, C. Wu, G. Xiong, G. Zuo, J. Jin, K. Ren, Y. Zhu, Z. Wang, H. Luo, Mechanical properties and cytotoxicity of nanoplate-like hydroxyapatite/polylactide nanocomposites prepared by intercalation technique, J Mech Behav Biomed Mater 47 (2015) 29-37.

[208] H. Luo, W. Li, D. Ji, G. Zuo, G. Xiong, Y. Zhu, L. Li, M. Han, C. Wu, Y. Wan, One-step exfoliation and surface modification of lamellar hydroxyapatite by intercalation of glucosamine, Materials Chemistry and Physics 173 (2016) 262-267.

[209] H. Luo, G. Zuo, G. Xiong, C. Li, C. Wu, Y. Wan, Porous nanoplate-like hydroxyapatite–sodium alginate nanocomposite scaffolds for potential bone tissue engineering, Materials Technology 32(2) (2017) 78-84.

[210] H. Luo, J. Xie, L. Xiong, Z. Yang, G. Zuo, H. Wang, Y. Zhu, Y. Wan, Engineering photoluminescent and magnetic lamellar hydroxyapatite by facile one-step Se/Gd dual-doping, Journal of Materials Chemistry B 6(21) (2018) 3515-3521.

[211] C. Liu, H. Zhai, Z. Zhang, Y. Li, X. Xu, R. Tang, Cells Recognize and Prefer Bone-like Hydroxyapatite: Biochemical Understanding of Ultrathin Mineral Platelets in Bone, ACS Applied Materials & Interfaces 8(44) (2016) 29997-30004.

[212] F. Nudelman, A.J. Lausch, N.A.J.M. Sommerdijk, E.D. Sone, In vitro models of collagen biomineralization, Journal of Structural Biology 183(2) (2013) 258-269.

[213] B. Li, L. Kan, X. Zhang, J. Li, R. Li, Q. Gui, D. Qiu, F. He, N. Ma, Y. Wang, H. Wei, Biomimetic Bone-like Hydroxyapatite by Mineralization on Supramolecular Porous Fiber Networks, Langmuir 33(34) (2017) 8493-8502.

[214] V. Sharma, A. Srinivasan, F. Nikolajeff, S. Kumar, Biomineralization process in hard tissues: The interaction complexity within protein and inorganic counterparts, Acta Biomaterialia 120 (2021) 20-37.

[215] B. Palazzo, D. Walsh, M. Iafisco, E. Foresti, L. Bertinetti, G. Martra, C.L. Bianchi, G. Cappelletti, N. Roveri, Amino acid synergetic effect on structure, morphology and surface properties of biomimetic apatite nanocrystals, Acta Biomaterialia 5(4) (2009) 1241-1252.

[216] A. Tsetsekou, D. Brasinika, V. Vaou, E. Chatzitheodoridis, On the synthesis of tailored biomimetic hydroxyapatite nanoplates through a bioinspired approach in the presence of collagen or chitosan and l-arginine, Materials Science and Engineering: C 43 (2014) 555-565.

[217] J.-J. Guan, B. Tian, S. Tang, Q.-F. Ke, C.-Q. Zhang, Z.-A. Zhu, Y.-P. Guo, Hydroxyapatite coatings with oriented nanoplate arrays: synthesis, formation mechanism and cytocompatibility, Journal of Materials Chemistry B 3(8) (2015) 1655-1666.

[218] W. Chen, B. Tian, Y. Lei, Q.-F. Ke, Z.-A. Zhu, Y.-P. Guo, Hydroxyapatite coatings with oriented nanoplate and nanorod arrays: Fabrication, morphology, cytocompatibility and osteogenic differentiation, Materials Science and Engineering: C 67 (2016) 395-408.

[219] M. Sundrarajan, S. Jegatheeswaran, S. Selvam, N. Sanjeevi, M. Balaji, The ionic liquid assisted green synthesis of hydroxyapatite nanoplates by Moringa oleifera flower extract: A biomimetic approach, Materials & Design 88 (2015) 1183-1190.

[220] L. Li, W. Song, J. Lian, J. Zhang, Environmentally Friendly Synthesis of Hydroxyapatite Nanoplates and their Adsorption Behavior of Proteins, Advanced Materials Research 113-116 (2010) 1036-1039.

[221] J.L. Cabrera, R. Velázquez-Castillo, E.M. Rivera-Muñoz, Synthesis of hydroxyapatite nanostructures using microwave heating, J Nanosci Nanotechnol 11(6) (2011) 5555-61.

[222] E.M. Rivera-Muñoz, R. Velázquez-Castillo, R. Huirache-Acuña, J.L. Cabrera-Torres, J. Arenas-Alatorre, Synthesis and Characterization of Hydroxyapatite-Based Nanostructures: Nanoparticles, Nanoplates, Nanofibers and Nanoribbons, Materials Science Forum 706-709 (2012) 589-594.

[223] E. Lester, M. Gimeno-Fabra, D. Irvine, K. Walton, D. Grant, F. Hild, P. Dunne, Continuous Synthesis of Dispersant-Coated Hydroxyapatite Plates, CrystEngComm 17 (2015).

[224] Y. Mori, M. Aizawa, Control of Ca / P Molar Ratio of Plate-shaped Hydroxyapatite Powders With an a (b)-axis Orientation and Their Thermal Stability, 2017.

[225] K. Lin, Y. Zhou, Y. Zhou, H. Qu, F. Chen, Y. Zhu, J. Chang, Biomimetic hydroxyapatite porous microspheres with co-substituted essential trace elements: Surfactant-free hydrothermal synthesis, enhanced degradation and drug release, Journal of Materials Chemistry 21(41) (2011) 16558-16565.

[226] J. Xiao, Y. Zhu, Q. Ruan, Y. Liu, Y. Zeng, F. Xu, L. Zhang, Biomacromolecule and Surfactant Complex Matrix for Oriented Stack of 2-Dimensional Carbonated Hydroxyapatite Nanosheets as Alignment in Calcified Tissues, Crystal Growth & Design 10(4) (2010) 1492-1499.

[227] C. Qi, Y.-J. Zhu, B.-Q. Lu, X.-Y. Zhao, J. Zhao, F. Chen, Hydroxyapatite nanosheet-assembled porous hollow microspheres: DNA-templated hydrothermal synthesis, drug delivery and protein adsorption, Journal of Materials Chemistry 22(42) (2012) 22642-22650.

[228] X. Chen, B. Yang, C. Qi, T.-W. Sun, F. Chen, J. Wu, X.-P. Feng, Y.-J. Zhu, DNA-templated microwave-hydrothermal synthesis of nanostructured hydroxyapatite for storing and sustained release of an antibacterial protein, Dalton Transactions 45(4) (2016) 1648-1656.

[229] X.-Y. Zhao, Y.-J. Zhu, J. Zhao, B.-Q. Lu, F. Chen, C. Qi, J. Wu, Hydroxyapatite nanosheet-assembled microspheres: Hemoglobin-templated synthesis and adsorption for heavy metal ions, Journal of Colloid and Interface Science 416 (2014) 11-18.

[230] S. Zhong, Z. Wen, J. Chen, Q. Li, X. Shi, S. Ding, Q. Zhang, Effects for rapid conversion from abalone shell to hydroxyapaptite nanosheets by ionic surfactants, Materials Science and Engineering: C 77 (2017) 708-712.

[231] Y. Su, J. Wang, S. Li, J. Zhu, W. Liu, Z. Zhang, Self-templated microwave-assisted hydrothermal synthesis of two-dimensional holey hydroxyapatite nanosheets for efficient heavy metal removal, Environmental Science and Pollution Research 26(29) (2019) 30076-30086.

[232] M. Murugesan, R. Subbiah, P. Meena, D. Mangalaraj, P. Nagamony, C. Viswanathan, K. Park, Green Synthesis and Characterization of Bioceramic Hydroxyapatite (HAp) Nanosheets and Its Cellular Study, Advanced Science, Engineering and Medicine 8 (2016) 216-221.

[233] S. Bose, S. Tarafder, Calcium phosphate ceramic systems in growth factor and drug delivery for bone tissue engineering: a review, Acta Biomater 8(4) (2012) 1401-21.

[234] M. Dang, L. Saunders, X. Niu, Y. Fan, P.X. Ma, Biomimetic delivery of signals for bone tissue engineering, Bone Research 6(1) (2018) 25.

[235] H.C. Pape, A. Evans, P. Kobbe, Autologous bone graft: properties and techniques, J Orthop Trauma 24 Suppl 1 (2010) S36-40.

[236] H. Qu, H. Fu, Z. Han, Y. Sun, Biomaterials for bone tissue engineering scaffolds: a review, RSC Advances 9(45) (2019) 26252-26262.

[237] M. Orciani, M. Fini, R. Di Primio, M. Mattioli-Belmonte, Biofabrication and Bone Tissue Regeneration: Cell Source, Approaches, and Challenges, Frontiers in Bioengineering and Biotechnology 5(17) (2017).

[238] H. Zhou, J. Lee, Nanoscale hydroxyapatite particles for bone tissue engineering, Acta Biomater 7(7) (2011) 2769-81.

[239] K. Li, F. Dai, T. Yan, Y. Xue, L. Zhang, Y. Han, Magnetic Silicium Hydroxyapatite Nanorods for Enhancing Osteoblast Response in Vitro and Biointegration in Vivo, ACS Biomaterials Science & Engineering 5(5) (2019) 2208-2221.

[240] N.K. Nga, N.T. Thuy Chau, P.H. Viet, Facile synthesis of hydroxyapatite nanoparticles mimicking biological apatite from eggshells for bone-tissue engineering, Colloids Surf B Biointerfaces 172 (2018) 769-778.

[241] T.-W. Sun, Y.-J. Zhu, F. Chen, Hydroxyapatite nanowire/collagen elastic porous nanocomposite and its enhanced performance in bone defect repair, RSC Advances 8(46) (2018) 26218-26229.

[242] G.-J. Huang, H.-P. Yu, X.-L. Wang, B.-B. Ning, J. Gao, Y.-Q. Shi, Y.-J. Zhu, J.-L. Duan, Highly porous and elastic aerogel based on ultralong hydroxyapatite nanowires for high-performance bone regeneration and neovascularization, Journal of Materials Chemistry B 9(5) (2021) 1277-1287.

[243] T. Zheng, L. Guo, Z. Du, H. Leng, Q. Cai, X. Yang, Bioceramic fibrous scaffolds built with calcium silicate/hydroxyapatite nanofibers showing advantages for bone regeneration, Ceramics International 47 (2021).

[244] H.S. Ko, S. Lee, J.Y. Jho, Synthesis and Modification of Hydroxyapatite Nanofiber for Poly(Lactic Acid) Composites with Enhanced Mechanical Strength and Bioactivity, Nanomaterials (Basel) 11(1) (2021).

[245] R.-L. Ying, R.-X. Sun, Q.-q. Li, C.-n. Fu, K.-Z. Chen, Synthesis of ultralong hydroxyapatite micro/nanoribbons and their application as reinforcement in collagen scaffolds for bone regeneration, Ceramics International 45(5) (2019) 5914-5921.

[246] J. Ji, B. Bar-On, H.D. Wagner, Mechanics of electrospun collagen and hydroxyapatite/collagen nanofibers, Journal of the Mechanical Behavior of Biomedical Materials 13 (2012) 185-193.

[247] Y.-Q. Tang, Q.-Y. Wang, Q.-F. Ke, C.-Q. Zhang, J.-J. Guan, Y.-P. Guo, Mineralization of ytterbium-doped hydroxyapatite nanorod arrays in magnetic chitosan scaffolds improves osteogenic and angiogenic abilities for bone defect healing, Chemical Engineering Journal 387 (2020) 124166.

[248] R. Hou, G. Zhang, G. Du, D. Zhan, Y. Cong, Y. Cheng, J. Fu, Magnetic nanohydroxyapatite/PVA composite hydrogels for promoted osteoblast adhesion and proliferation, Colloids and Surfaces B: Biointerfaces 103 (2013) 318-325.

[249] S. Moeini, M.R. Mohammadi, A. Simchi, In-situ solvothermal processing of polycaprolactone/hydroxyapatite nanocomposites with enhanced mechanical and biological performance for bone tissue engineering, Bioactive Materials 2(3) (2017) 146-155.

[250] P. Feng, R. Zhao, L. Yang, S. Chen, D. Wang, H. Pan, C. Shuai, Hydrothermal synthesis of hydroxyapatite nanorods and their use in PCL bone scaffold, Ceramics International 48(22) (2022) 33682-33692.

[251] C. Liao, K. Li, K. Wong, W.Y. Tong, K. Yeung, S. Tjong, Novel polypropylene biocomposites reinforced with carbon nanotubes and hydroxyapatite nanorods for bone replacements, Materials science & engineering. C, Materials for biological applications 33 (2013) 1380-8.

[252] N.K. Nga, T.T. Hoai, P.H. Viet, Biomimetic scaffolds based on hydroxyapatite nanorod/poly(d,l) lactic acid with their corresponding apatite-forming capability and biocompatibility for bone-tissue engineering, Colloids and Surfaces B: Biointerfaces 128 (2015) 506-514.

[253] H. Zhang, Q.-W. Fu, T.-W. Sun, F. Chen, C. Qi, J. Wu, Z.-Y. Cai, Q.-R. Qian, Y.-J. Zhu, Amorphous calcium phosphate, hydroxyapatite and poly(d,l-lactic acid) composite nanofibers: Electrospinning preparation, mineralization and in vivo bone defect repair, Colloids and Surfaces B: Biointerfaces 136 (2015) 27-36.

[254] W. Pon-On, P. Suntornsaratoon, N. Charoenphandhu, J. Thongbunchoo, N. Krishnamra, I.M. Tang, Synthesis and investigations of mineral ions-loaded apatite from fish scale and PLA/chitosan composite for bone scaffolds, Materials Letters 221 (2018) 143-146.

[255] D. Khare, B. Basu, A.K. Dubey, Electrical stimulation and piezoelectric biomaterials for bone tissue engineering applications, Biomaterials 258 (2020) 120280.

[256] P. Singh, X. Yu, A. Kumar, A.K. Dubey, Recent advances in silicate-based crystalline bioceramics for orthopedic applications: a review, Journal of Materials Science 57(28) (2022) 13109-13151.

[257] Z. Fan, J. Wang, Z. Wang, H. Ran, Y. Li, L. Niu, P. Gong, B. Liu, S. Yang, One-pot synthesis of graphene/hydroxyapatite nanorod composite for tissue engineering, Carbon 66 (2014) 407-416.

[258] Y. Wei, L. Liu, H. Gao, X. Shi, Y. Wang, In Situ Formation of Hexagon-like Column Array Hydroxyapatite on 3D-Plotted Hydroxyapatite Scaffolds by Hydrothermal Method and Its Effect on Osteogenic Differentiation, ACS Applied Bio Materials 3(3) (2020) 1753-1760.

[259] S. Lamkhao, M. Phaya, C. Jansakun, N. Chandet, K. Thongkorn, G. Rujijanagul, P. Bangrak, C. Randorn, Synthesis of Hydroxyapatite with Antibacterial Properties Using a Microwave-Assisted Combustion Method, Scientific Reports 9(1) (2019) 4015.

[260] P. Shree, C.K. Singh, K.K. Sodhi, J.N. Surya, D.K. Singh, Biofilms: Understanding the structure and contribution towards bacterial resistance in antibiotics, Medicine in Microecology 16 (2023) 100084.

[261] Y. Lu, W.J. Cai, The Role of Staphylococcal Biofilm on the Surface of Implants in Orthopedic Infection, 10(10) (2022).

[262] L. Crémet, S. Corvec, P. Bémer, L. Bret, C. Lebrun, B. Lesimple, A.-F. Miegeville, A. Reynaud, D. Lepelletier, N. Caroff, Orthopaedic-implant infections by Escherichia coli: Molecular and phenotypic analysis of the causative strains, Journal of Infection 64(2) (2012) 169-175.

[263] Y. Min, S. Wu, W. Li, Y. Ma, Y. Wang, P. Zhang, Y. Zheng, One-pot synthesis of multipod Au-Cu nanocrystals with tunable branching for efficient photothermal treatment against multidrug-resistant bacteria, Journal of Alloys and Compounds 976 (2024) 172935.

[264] K. Li, J. Chen, Y. Xue, T. Ding, S. Zhu, M. Mao, L. Zhang, Y. Han, Polymer brush grafted antimicrobial peptide on hydroxyapatite nanorods for highly effective antibacterial performance, Chemical Engineering Journal 423 (2021) 130133.

[265] L. Wang, C. Hu, L. Shao, The antimicrobial activity of nanoparticles: present situation and prospects for the future, International journal of nanomedicine 12 (2017) 1227-1249.

[266] K. Baskar, T. Anusuya, G. Devanand Venkatasubbu, Mechanistic investigation on microbial toxicity of nano hydroxyapatite on implant associated pathogens, Materials science & engineering. C, Materials for biological applications 73 (2017) 8-14.

[267] G.S. Kumar, S. Rajendran, S. Karthi, R. Govindan, E.K. Girija, G. Karunakaran, D. Kuznetsov, Green synthesis and antibacterial activity of hydroxyapatite nanorods for orthopedic applications, MRS Communications 7(2) (2017) 183-188.

[268] H. Abed, N. H, E. Salim, Influence of nano-hydroxyapatite particles on the mechanical and antibacterial properties of polycarbonate films, Materials Research Express 10 (2023).

[269] G. Karunakaran, E.-B. Cho, G.S. Kumar, E. Kolesnikov, S.K. Govindaraj, K. Mariyappan, S. Boobalan, CTAB enabled microwave-hydrothermal assisted mesoporous Zn-doped hydroxyapatite nanorods synthesis using bio-waste Nodipecten nodosus scallop for biomedical implant applications, Environmental Research 216 (2023) 114683.

[270] O. Geuli, N. Metoki, T. Zada, M. Reches, N. Eliaz, D. Mandler, Synthesis, coating, and drug-release of hydroxyapatite nanoparticles loaded with antibiotics, Journal of Materials Chemistry B 5(38) (2017) 7819-7830.

[271] J.J. Aguilera-Correa, M. Gisbert-Garzarán, A. Mediero, M.J. Fernández-Aceñero, D. de-Pablo-Velasco, D. Lozano, J. Esteban, M. Vallet-Regí, Antibiotic delivery from bone-targeted

mesoporous silica nanoparticles for the treatment of osteomyelitis caused by methicillin-resistant Staphylococcus aureus, Acta biomaterialia 154 (2022) 608-625.

[272] S.A. Kelly, A.M. Rodgers, S.C. O'Brien, R.F. Donnelly, B.F. Gilmore, Gut Check Time: Antibiotic Delivery Strategies to Reduce Antimicrobial Resistance, Trends in Biotechnology 38(4) (2020) 447-462.

[273] M. Kavruk, O. Celikbicak, V.C. Ozalp, B.A. Borsa, F.J. Hernandez, G. Bayramoglu, B. Salih, M.Y. Arica, Antibiotic loaded nanocapsules functionalized with aptamer gates for targeted destruction of pathogens, Chemical Communications 51(40) (2015) 8492-8495.

[274] A. Nazli, D.L. He, D. Liao, M.Z.I. Khan, C. Huang, Y. He, Strategies and progresses for enhancing targeted antibiotic delivery, Advanced drug delivery reviews 189 (2022) 114502.

[275] B.L. Smith, S. Fernando, M.D. King, Escherichia coli resistance mechanism AcrAB-TolC efflux pump interactions with commonly used antibiotics: a molecular dynamics study, Scientific Reports 14(1) (2024) 2742.

[276] W.C. Reygaert, An overview of the antimicrobial resistance mechanisms of bacteria, AIMS microbiology 4(3) (2018) 482-501.

[277] U. Kesarwani, A.K. Dubey, Antibacterial efficacy of bone mimicking-hydroxyapatite nanoplates with varying morphology, Inorganic Chemistry Communications 174 (2025) 113918.

[278] D. Hawthorne, A. Pannala, S. Sandeman, A. Lloyd, Sustained and targeted delivery of hydrophilic drug compounds: A review of existing and novel technologies from bench to bedside, Journal of Drug Delivery Science and Technology 78 (2022) 103936.

[279] N. Safitri, N. Rauf, D. Tahir, Enhancing drug loading and release with hydroxyapatite nanoparticles for efficient drug delivery: A review synthesis methods, surface ion effects, and clinical prospects, Journal of Drug Delivery Science and Technology 90 (2023) 105092.

[280] M. Rivas, L.J. del Valle, A.M. Rodríguez-Rivero, P. Turon, J. Puiggalí, C. Alemán, Loading of Antibiotic into Biocoated Hydroxyapatite Nanoparticles: Smart Antitumor Platforms with Regulated Release, ACS Biomaterials Science & Engineering 4(9) (2018) 3234-3245.

[281] A.P.S. Prasanna, G.D. Venkatasubbu, Sustained release of amoxicillin from hydroxyapatite nanocomposite for bone infections, Progress in biomaterials 7(4) (2018) 289-296.

[282] M.S. Asghar, U. Ghazanfar, M. Idrees, M.S. Irshad, Z. Haq, M.Q. Javed, S.Z. Hassan, M. Rizwan, In vitro controlled drug delivery of cationic substituted hydroxyapatite nanoparticles; enhanced anti-chelating and antibacterial response, Kuwait Journal of Science 50(2) (2023) 97-104.

[283] C. Soriano-Souza, H. Valiense, E. Mavropoulos, V. Martinez-Zelaya, A.M. Costa, A.T. Alves, M. Longuinho, R. Resende, C. Mourão, J. Granjeiro, M.H. Rocha-Leao, A. Rossi, M. Calasans-Maia, Doxycycline containing hydroxyapatite ceramic microspheres as a bone-targeting drug delivery system, Journal of biomedical materials research. Part B, Applied biomaterials 108(4) (2020) 1351-1362.